Aspects of the energy transition and their effects on power systems

Thèse N° 9307

Présentée le 4 avril 2019

à la Faculté des sciences de base
Chaire de théorie de la matière condensée
Programme doctoral en physique

pour l'obtention du grade de Docteur ès Sciences

par

Laurent Vincent PAGNIER

Acceptée sur proposition du jury

Prof. N. Grandjean, président du jury
Prof. F. Mila, Prof. Ph. Jacquod, directeurs de thèse
Prof. M. Chertkov, rapporteur
Prof. S. Kettemann, rapporteur
Prof. F. Dörfler, rapporteur

2019

EPFL
ÉCOLE POLYTECHNIQUE
FÉDÉRALE DE LAUSANNE

À mes parents, ma petite soeur et mes proches…

Abstract

Most European countries are committed to an energy transition which consists in the substitution of conventional CO_2 emitting energy sources by new renewable energy sources (RES), in particular wind and solar power. As opposed to conventional energy sources, new RES are distributed, non-dispatchable, fluctuating and inertialess and have negligible marginal costs. In this thesis, we investigate the impact of the energy transition on the electricity sector in Europe.

In the first part of this thesis, we investigate the future electricity production and prices in Europe. We develop a dispatch algorithm on an aggregated model of the pan-European power grid with which we study the future European productions. We show that, as the penetration of new RES increases, the transmission grids are more strongly used and that more flexibility is required from conventional generators. The existing infrastructures seem to able to absorb, through increased international power exchanges and usage of the existing pumped-storage hydroelectricity, the variations of new RES productions even for high penetrations. Then we investigate the effects of new RES on electricity prices. We explain why, due to their negligible marginal cost and their lack of dispatchability, they tend to drag electricity prices down and can be considered as a reduction of the load in the electricity pricing. In particular, photovoltaics decreases the volatility of electricity prices. We show that, in most European countries, the day-ahead electricity price is strongly correlated with the residual load, which is obtained by subtracting the non-dispatchable productions, in particular those of the new RES, from the load. From this observation, we build an effective price model based solely on the residual load with which the revenues of different electricity producers are evaluated.

The second part of this thesis deals with disturbances in large transmission grids. The substitution of conventional generators by inertialess RES reduces the amount of inertia connected to power systems which might affect their reliability. To examine the propagation of disturbances in large transmission grids, we develop a dynamical model of the continental European transmission grid. We observe that the magnitude of the disturbance following a power loss depends on the fault location. We show that when inertia and primary control are uniformly distributed, the faults exciting the slowest eigenmodes of the network Laplacian are followed by the strongest disturbances. Reducing inertia on those eigenmodes, which are mostly located in the periphery of the grid, affects more its resilience than when the reduction occurs in its center. Finally, we use perturbation theory to derive algorithms for optimal placement of inertia and primary control when some mild inhomogeneities are present in their distributions. We show that,when the vulnerability of the whole grid is taken into account, a uniform dis-

tribution of inertia is optimal and the primary control is best placed in the periphery of the grid.

Résumé

La plupart des pays européens sont engagés dans une transition énergétique qui consiste à remplacer les énergies fossiles émettant du CO_2 par de nouvelles énergies renouvelables (NER), en particulier par de l'énergie solaire et éolienne. A contrario des énergies conventionnelles, les NER sont des productions intermittentes, distribuées et non-réglable. Ce sont des générateurs sans inertie et leurs coûts marginaux de production sont négligeables. Dans cette thèse, nous investiguons l'impact de la transition énergétique sur le secteur électrique en Europe.

Dans la première partie de cette thèse, nous étudions les futures productions et prix d'électricité en Europe. Nous développons un algorithme de répartition des productions sur un modèle agrégé du réseau de transport pan-européen. Nous montrons que, lorsque la pénétration de NER augmente, les réseaux de transport sont plus sollicités et que plus de flexibilité est demandé aux générateurs conventionnels. Les infrastructures existantes semblent capable d'absorber, à travers des échanges internationaux accrus et un fort usage du pompage turbinage, les variations de production dues aux NER même lorsque leur pénétration est importante. Ensuite, nous étudions les effets des NER sur les prix de l'électricité. Nous expliquons pourquoi, à cause de leur coûts marginaux négligeables et leur manque de flexibilité, ils tirent les prix de l'électricité vers le bas. Nous notons que les NER peuvent être considérés comme une réduction de la charge dans le processus du calcul du prix de l'électricité. Nous montrons que les prix de l'électricité sur les marchés "day-ahead" sont fortement corrélés avec la charge résiduelle qui est obtenue en soustrayant de la charge les productions non-flexibles, en particulier celles des NER. De cette observation, nous élaborons un modèle effectif du prix de l'électricité à partir de la charge résiduelle et nous l'utilisons pour évaluer les revenues de différents producteurs d'électricité.

La seconde partie de cette thèse est consacrée aux perturbations dans les réseaux de transport d'électricité. La substitution des générateurs conventionnels par des NER réduit la quantité d'inertie connectée aux réseaux électriques, ce qui pourrait réduire leur fiabilité. Afin d'examiner la propagation de perturbations dans les réseaux de transport, nous développons un modèle dynamique du réseau d'Europe continental. Nous observons que la magnitude des perturbations suivant des pertes de puissance localisées dépend de l'endroit de celles-ci. Nous montrons que lorsque l'inertie et le réglage primaire sont uniformément repartis dans le système, les pertes excitant les modes propres les plus lents du Laplacien du réseau sont suivies par les perturbations les plus fortes. En réduisant l'inertie sur ces modes, qui se situent principalement en périphérie du réseau, cela affecte plus sa fiabilité que lorsque la réduction est faite au centre de celui-ci. Finalement, nous appliquons la théorie des perturbations pour

dériver des algorithmes de placement optimal pour l'inertie et le réglage primaire dans le cas où les distributions de celles-ci sont légèrement inhomogènes. Nous montrons que lorsque l'on considère la vulnérabilité du réseau pris dans son ensemble, une distribution homogène de l'inertie ainsi que plus de réglage primaire placé en périphérie du réseau sont optimaux.

Mots clés : *intégration des énergies renouvelables, répartition de la production, prix de l'électricité, charge résiduelle, fiabilité des réseaux de transport d'électricité, propagation des perturbations, vecteur de Fiedler, taux de changement de fréquence (RoCoF), placement optimal de l'inertie et du réglage primaire.*

Contents

Contents

II The roles of inertia, primary control and grid geometry on disturbances in transmission grids

General introduction

Over the 20th century, the average temperature on Earth has increased by $0.66°C$ [1]. Today, there is a consensus among scientists that mankind influences the climate worldwide [2]. Limiting our impact on climate may be achieved by the reduction of our greenhouse gas emissions, in particular CO_2. This materializes in the energy transition which is the ongoing process during which we depart from fossil energy in favor of new renewable energy sources (RES) in particular solar and wind power.

The energy transition is a complex interdisciplinary subject. It encompasses branches of social sciences as well as technical and natural sciences. Policymakers vote incentives for renewable energy sources or taxes on CO_2 emitting sources giving the necessary framework to the unfolding of the energy transition. The Economics must design new schemes for a fair competition between new energy sources and conventional ones. Multiple disciplines of Engineering have to be involved to optimize our energy uses with sustainable transport, urban planning, building physics, domotics or appliance efficiency. Last but not least, Physics, which studies complex systems, can help to understand the general laws governing the energy transition. The present work focuses on the electricity aspect of the energy transition to which we try to apply Einstein's moto [3] "Everything should be made as simple as possible, but no simpler." by using techniques as coarse-grained modeling and perturbation theory.

Since the end of the 19th century, power systems have grown following the increasing electricity demand. New generators, mainly relying on fossil fuels, were progressively installed. Nowadays, 65% of the electricity consumed in the World is produced from fossil fuel. An alternative to fossil fuel based electricity generation is nuclear power which has the advantage of not emitting CO_2. However, after the Chernobyl disaster and the more recent Fukushima accident, ecological and safety concerns related to nuclear power emerged in public opinion. This led Germany to start the withdrawal of nuclear power from its energy mix. In any case, uranium reserves are limited, nuclear power is not sustainable and cannot be a major contributor to the World energy mix for more than a century. The only sustainable substitute for fossil fuel based electricity generation is solar and wind power. Supported by public incentives, their penetration has rapidly increased in Europe during the last decade. Germany has doubled its wind power generation capacity and has increased tenfold its installed photovoltaics (PV) panels over this period of time. On the other hand, fossil-fired generators have mainly been kept running. Over the same period, the electricity demand in Europe has stagnated, reflecting

the economic heath since the 2008 financial crisis [4]. This has led to a generation overcapacity in Europe.

The initial guideline of this work was to investigate how the energy transition will affect the Swiss electricity sector. In 2011, the Swiss parliament decided not to renew the aging Swiss nuclear reactors which are about to reach their lifespan. In December 2019, the Mühleberg power plant will be the first Swiss nuclear power plant to be decommissioned. The others will follow within two decades. Nuclear plants have produced 38% of the Swiss electricity over the past twenty years [4]. Therefore, a significant portion of the Swiss electricity supply will be missing in the near future if nothing is undertaken. The development of hydroelectricity is capped, most of the resources are already exploited. Switzerland is committed to reducing its greenhouse gas emissions, hence the commissioning of new thermal power plants seems unrealistic. The remaining possibility is a drastic increase of new RES in the Swiss energy mix over the next decades. These new energy sources in Switzerland as well as in Europe affect the existing infrastructures. They will modify the power flows in the pan-European transmission grid which will require reinforcement. The Swiss hydroelectricity suffers from the low electricity prices which are imputed to the increasing penetration of new RES and the resulting generation overcapacity in Europe.

New RES differ from conventional generators in different aspects: (i) they are distributed, (ii) they are non-dispatchable and fluctuating, (iii) they have negligible marginal costs and (iv) they are inertialess. (i) and (ii) affect the power flows in transmission grids. (ii) and (iii) have strong effects on power markets and electricity prices. Their lack of dispatchability means a poor adequacy between their productions and electricity demand which forces the other productions to be more flexible. (iv) affects the reliability of the grid. When less rotational inertia is present in a power system, it reacts more promptly and more strongly to contingencies which means less time to restore the situation before a potential cascading failure. For a harmonious unfolding of the energy transition, it is paramount to mitigate the non-desirable effects of new RES which can be tackled at the distribution grid or transmission grid level. The first approach, which relies on smart grids and demand response to maximize the local use of new RES electricity, mitigates locally the unwanted power fluctuations due to the new RES. In this distributed approach, electricity is produced and consumed almost only locally and power exchanges are reduced, making the high voltage transmission grid much less needed than it is now. However this local approach is quite costly due to the amount of local storage (electric batteries) required to absorb fluctuations of new RES. The second approach takes advantage of the spatial and temporal disparities of the wind and solar productions, surplus electricity is stored in large facilities as pumped-storage power plants or exported through international power exchanges. In this work, we focus on this latter approach at transmission grid level.

In the first part of this work, we investigate the future electricity production and prices in Europe. To carry out our investigation on the substitution of conventional generators by new RES, we build an aggregated model of the pan-European grid which allows to dispatch the

national production fleets through an economic dispatch. Once our model is calibrated, we investigate the future dispatches of conventional generators when the penetration of new RES in European mixes is significantly higher than its present level. We show that high penetrations of new RES can be reached with only minor enhancement of the pan-European transmission grid. However, this requires significantly higher flexibility of conventional generators.

The electricity price depends on the law of supply and demand. Load is, to a large extent, inflexible and production varies to support it and consequently electricity price used to follow the load profile. The energy transition in Europe is accompanied by the liberalization of electricity markets. Nowadays, a significant share of the electricity consumed in Europe is traded in day-head spot markets, in which the auctions are made on the day prior to the delivery. Over the last decades, with the increasing penetration of renewable energy sources, a significant share of electricity production became non-dispatchable. Due to their negligible marginal prices, the new RES tend to draw down electricity prices, leading to a loss of profitability of flexible sources. We propose to study future economic opportunities with residual load which is the national load from which the non-flexible productions are subtracted. The underlying idea is that electricity price should be proportional to the missing power that flexible sources must generate to sustain the load. With this economic indicator, we investigate the future revenues of flexible sources which will be needed for a serene unfolding of the energy transition in Europe.

The second part of this work deals with the absence of rotational inertia of new RES. In power systems, there is always an imbalance between generation and load which drives up (down) the system frequency if there is a surplus (lack) of generation. Synchronous generators connected to the grid help to mitigate power imbalances, their kinetic energy increases (decreases) which provides (absorbs) the missing (surplus) power. This grants time to deploy primary control and to rectify the system frequency. The lack of rotational inertia is never a concern in power systems extensively supplied by conventional generators. On the other hand, the ongoing substitution of thermal power plants by PV panels and wind turbines reduces the amount of inertia connected to the continental European grid which might affect its reliability.

Having a high spatial resolution of the transmission grid is paramount to address the problem of rotational inertia. Consequently, we develop a detailed model of the European transmission grid from publicly available databases. We use this dynamical model to investigate the propagation and the magnitude of disturbances following localized abrupt power losses. We discover that their magnitudes are strongly dependent on the fault location. We relate the location of the largest disturbances to an element of graph theory, the Fiedler vector. We show that when inertia is reduced on the buses with large squared Fielder components the system gets more easily disturbed then when the same amount of inertia is reduced on buses with small squared Fielder components.

Finally, as inertia can be emulated by power electronics, we investigate the optimal placement of rotational inertia and primary control with a perturbation theory approach. We start our

Contents

investigation by the case where inertia and primary control are uniformly distributed in the system. On this assumption, the system dynamics has a closed-form expression. We quantify the magnitude of disturbance by a performance measure. We show that, in this case, the most vulnerable sites are those exciting the slowest eigenmodes of the Laplacian of the grid. By using perturbation theory, we investigate the cases where some mild heterogeneities are present in local damping ratio and inertia. We obtain the sensitivities of our measure in local variations of inertia and primary control and we obtain algorithms to optimally distribute these resources. We find that primary control must be placed mainly on the slowest eigenmodes of the Laplacian of the grid and that inertia is required in the vicinity of the fault location. We conclude our investigation by applying our findings to our continental European grid.

1 General notions on power system analysis

In this introductory chapter, we present some basic topics. They are treated in more details in textbooks on power system analysis, see for instance Refs. [5, 6].

1.1 Notions of Physics

The conservation of the electric charge implies that the current i_j injected in the power system through the bus #j equals the sum of the currents exiting this bus through the transmission lines, this reads

$$i_j = \sum_{k \sim j} i_{kj}, \tag{1.1}$$

where $k \sim j$ means that the sum is carried over the buses directly connected to bus #j. Ohm's law states that the electric current i flowing along a conductor is related to the voltage difference v between its ends

$$v = Ri, \tag{1.2}$$

where R is its resistance. The electric charge Q stored in a capacitor is related to the voltage difference v between its poles by $Q = Cv$ where C is its capacitance. When the voltage and the current are time-dependent, in addition to Ohm's law, they are related by the following relationships

$$i = C \frac{\mathrm{d}v}{\mathrm{d}t}, \tag{1.3}$$

$$v = L \frac{\mathrm{d}i}{\mathrm{d}t}, \tag{1.4}$$

where L is the inductance of a inductor. Eq. (1.3) describes the charging current $i = \mathrm{d}Q/\mathrm{d}t$ in a capacitor when the voltage between its poles varies and Eq. (1.4) describes the induced voltage when the current varies in an inductor.

1.2 Alternating current

In this section, we introduce the complex quantities (phasors) used for the analysis of the steady state of power systems.

Since the 1890s and the end of the "war of the currents", which resulted in the victory of Nikola Tesla's alternating current (AC) against Thomas Edison's direct current, most power systems are operated in AC. The main advantage of alternating current over direct current is the ease with which it can be transformed to a higher voltage to mitigate transmission losses.

When the generators in the system have three identical, but regularly delayed windings, it results in three distinct phases which have relative phase differences of $\pm 2/3\pi$ (120°). The advantage of three-phase electric power over single-phase, is that it does not require a neutral cable for the current to return to the generator. As the amount of conductor to transmit a given power is reduced, it is economically advantageous, to operate power systems in three-phase. On the assumption that the three phases are balanced, power systems can be described by per-phase (single phase) equivalent circuits [5, 6]. In this works, we always assume that the three phases are balanced.

In alternating current, voltage $v(t)$ and current $i(t)$ are given by

$$v(t) = V\cos(\omega_0 t + \theta_V), \qquad i(t) = I\cos(\omega_0 t + \theta_I), \tag{1.5}$$

where θ_V and θ_I are the phase shifts of voltage and current phases compared to some reference and $\omega_0 = 2\pi f_0$ with the system frequency $f_0 = 50$ Hz in Europe and 60 Hz in America. With the choice $\theta_V = 0$, from Eq. (1.5), the instantaneous power $p(t) = v(t)i(t)$ reads

$$p(t) = \frac{VI}{2}\Big[\cos(\theta)\big(1 + \cos(2\omega_0 t)\big) + \sin(\theta)\sin(2\omega_0 t)\Big], \tag{1.6}$$

where $\theta = \theta_I - \theta_V$ is the phase shift between voltage and current. The average transmitted power $\langle p(t)\rangle$ is obtained by integrating the instantaneous power $p(t)$ over a period $T = 2\pi/\omega_0$, we get

$$\langle p(t)\rangle = \frac{1}{T}\int_0^T p(t)\mathrm{d}t = \frac{VI\cos(\theta)}{2}. \tag{1.7}$$

By defining the *active power* $P \equiv VI\cos(\theta)/2$ and the *reactive power* $Q \equiv VI\sin(\theta)/2$, the instantaneous power reads

$$p(t) = P\big[1 + \cos(2\omega_0 t)\big] + Q\sin(2\omega_0 t). \tag{1.8}$$

From Eq. (1.8), we observe that the instantaneous power consist in two terms: the first one has an average power of P and the second one has a zero average power. We find that when $v(t)$ and $i(t)$ are in phase, $\theta = 0$, the average transmitted power is maximal and corresponds

to $VI/2$ and when there is a phase shift $\theta = \pi/2$, the average transmitted power vanishes. For steady state analysis, it is convenient to describe the voltage and current as complex numbers (phasors). Indeed, as the system frequency ω_0 is assumed be constant, the $v(t)$ and $i(t)$ are fully characterized by their magnitudes and phases and we can describe them by following complex numbers

$$\underline{V} = \frac{V}{\sqrt{2}}e^{i\theta_V}, \qquad \underline{I} = \frac{I}{\sqrt{2}}e^{i\theta_I}, \tag{1.9}$$

where we use underlines to denote complex quantities. A relation similar to Ohm's law relates $\underline{I}$ to $\underline{V}$

$$\underline{I} = Z\underline{V}, \tag{1.10}$$

where $Z = R + iX$ is the impedance of the circuit element. The imaginary part X, called reactance, depends on the inductive or capacitive nature of the element. From Eqs. (1.3) and (1.4), we find that $X = \omega_0 L$ and $X = 1/(\omega_0 C)$ for an inductor and a capacitor. The complex power $\underline{S}$ is defined as

$$\underline{S} = \underline{V}\,\underline{I}^*, \tag{1.11}$$

where $*$ denotes the complex conjugate. From Eq. (1.9), we find that $\underline{S} = P + iQ$. In the following we investigate the relationship between the voltage magnitudes and phases and active and reactive power injections in a transmission grid.

1.3 Power flow equations

In this section, we derive the power flow equations which give the relationships between the power injections in the system and the bus voltages. On the assumption that the lines are lossless, that the voltage magnitudes are close to their rated values and that the voltage phases differences are small, we derive an approximate of the power flow equations, called DC power flow approximation. We show that, in this case, the power flows in the system can be directly obtained form the nodal power injection thanks to the DC power transfer distribution factors.

Fig. 1.1 (a) shows the lumped circuit of infinitesimal slice of a transmission line of length $\mathrm{d}x$. The resistance r^{km} depends on the materials of which the transmission lines are composed. The inductance l^{km} and the capacitance c^{km} depend on the geometry of the transmission line, in particular on the distances between the three cables composing the line and between the cables and the ground.

From the relationships between the voltages and currents at the extremities of the slice, we get
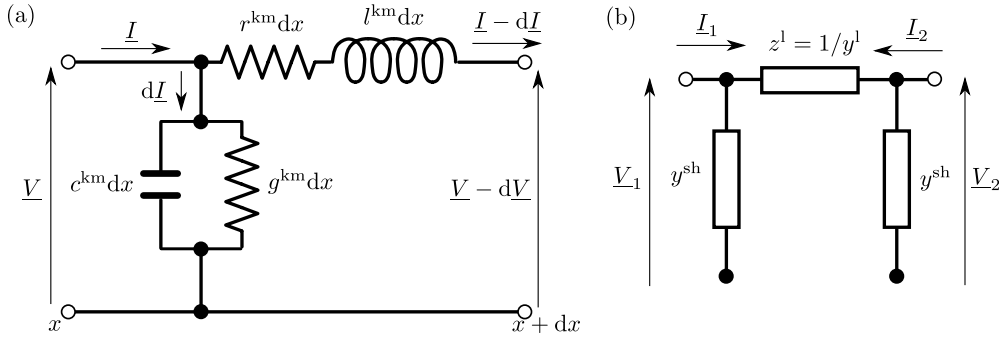
Figure 1.1 – *(a) Infinitesimal lumped circuit of a transmission line. (b) Π-equivalent circuit of a transmission line. Source: own illustration loosely based on Refs. [5, 6].*

the following equations

$$\frac{d}{dx}\underline{V} = z\underline{I},\tag{1.12}$$

$$\frac{d}{dx}\underline{I} = y\underline{V},\tag{1.13}$$

where $z = r^{\text{km}} + i\omega_0 l^{\text{km}}$ and $y = g^{\text{km}} + i\omega_0 c^{\text{km}}$. In Eq. (1.12), we used that $\underline{I} \approx \underline{I} - d\underline{I}$. From Eqs. (1.12) and (1.13), voltage $\underline{V}(x)$ and current $\underline{I}(x)$ at any point x of the line are given by

$$\underline{V}(x) = \underline{V}_0 \cosh(\sqrt{zy}x) + \sqrt{z/y}\underline{I}_0 \sinh(\sqrt{zy}x),\tag{1.14}$$

$$\underline{I}(x) = \underline{I}_0 \cosh(\sqrt{zy}x) + \sqrt{z/y}\underline{V}_0 \sinh(\sqrt{zy}x),\tag{1.15}$$

where $\underline{V}_0$ is the bus voltage at the first extremity of the line and $\underline{I}_0$ is the current exiting this extremity. We are interested in the relation between voltages and currents at the extremities of the line. We define $\underline{V}_1 \equiv \underline{V}_0$, $\underline{I}_1 \equiv \underline{I}_0$, $\underline{V}_2 \equiv \underline{V}(L)$, and $\underline{I}_2 \equiv -\underline{I}(L)$ and $\zeta \equiv \sqrt{zy}L$. Eqs. (1.14) and (1.15) can be reformulated as

$$\begin{bmatrix} \underline{I}_1 \\ \underline{I}_2 \end{bmatrix} = \begin{bmatrix} y^{\text{l}} + y^{\text{sh}} & -y^{\text{l}} \\ -y^{\text{l}} & y^{\text{l}} + y^{\text{sh}} \end{bmatrix} \begin{bmatrix} \underline{V}_1 \\ \underline{V}_2 \end{bmatrix},\tag{1.16}$$

where $y^{\text{l}} \equiv -\zeta/(zL\sinh\zeta)$ is the series admittance of the line and $y^{\text{sh}} \equiv -\zeta \tanh(\zeta/2)/(zL)$ is its shunt admittance. For short lines, we can obtain approximate expressions of y^{l} and y^{sh} by truncating the series expansions $\zeta/\sinh(\zeta) = 1 + \zeta^2/2 + \mathcal{O}(\zeta^4)$ and $\zeta \tanh\zeta/2 = \zeta^2/2 + \mathcal{O}(\zeta^4)$, we get

$$y^{\text{l}} \approx -1/(zL), \qquad y^{\text{sh}} \approx -yL,\tag{1.17}$$

where the notion of shortness depends on the characteristics of the line. For very short lines, we can even neglect the shunt admittance y^{sh} which is small in comparison with y^{l}. We observe that Eq. (1.16) is equivalent to the electric circuit displayed in Fig. 1.1 (b). Hence, we showed that a transmission line can be described by an equivalent electric circuit and that

the series impedance $z^{\mathrm{l}} = 1/y^{\mathrm{l}}$ and the shunt admittance y^{sh} are roughly proportional to the length of the line. Furthermore, with Eq. (1.16), we expressed the currents exiting the buses as a function of the bus voltages.

The same construction is applicable for each line in the transmission grid, and the currents $\boldsymbol{I} = [\underline{I}_1, \cdots, \underline{I}_N]^\top$ injected in the system are related to the bus voltages $\boldsymbol{V} = [\underline{V}_1, \cdots, \underline{V}_N]^\top$ by

$$\boldsymbol{I} = \boldsymbol{Y}\boldsymbol{V}, \tag{1.18}$$

where $\boldsymbol{Y}$ is the admittance matrix, the elements of which read

$$y_{ij} = \begin{cases} \sum_{k \sim i} \left(y_{ik}^{\mathrm{l}} + y_{ik}^{\mathrm{sh}} \right), & \text{if } i = j, \\ -y_{ij}^{l}, & \text{if } i \sim j. \end{cases} \tag{1.19}$$

The admittance matrix is a complex matrix, we can write it as $\boldsymbol{Y} = \boldsymbol{G} + i\boldsymbol{B}$ where $\boldsymbol{G}$ is the conductance matrix and $\boldsymbol{B}$ is the susceptance matrix. From Eq. (1.18), we have the the complex power injected in the system at bus #i is given by

$$\underline{S}_i = \underline{V}_i \underline{I}_i^* = \underline{V}_i \sum_j y_{ij}^* \underline{V}_j^*. \tag{1.20}$$

By expressing the complex power injection $\underline{S}_i$ in terms of active and reactive power injections P_i and Q_i and the voltages $\{\underline{V}_j\}$ in terms of their magnitudes $\{V_j\}$ and phases $\{\theta_j\}$ in Eq. (1.20), we obtain the *power flow equations* in their standard expression, which read

$$P_i = \sum_j V_i V_j \left[g_{ij} \cos(\theta_i - \theta_j) + b_{ij} \sin(\theta_i - \theta_j) \right], \tag{1.21}$$

$$Q_i = \sum_j V_i V_j \left[g_{ij} \sin(\theta_i - \theta_j) - b_{ij} \cos(\theta_i - \theta_j) \right]. \tag{1.22}$$

They are nonlinear equations and must be solved numerically by iterative methods as Newton-Raphson [5, 6]. Eqs. (1.21) and (1.22) are valid for any balanced power system at any voltage level. Fig. 1.2 shows that, in high voltage transmission grids, the susceptance b_{ij} is generally significantly higher than the conductance g_{ij}. For theses systems, one typically neglects g_{ij} in comparison with b_{ij} which corresponds to the lossless approximation. Eqs. (1.21) and (1.22) become

$$P_i = \sum_j V_i V_j b_{ij} \sin(\theta_i - \theta_j), \tag{1.23}$$

$$Q_i = -\sum_j V_i V_j b_{ij} \cos(\theta_i - \theta_j). \tag{1.24}$$

In transmission grid, the phase difference between the two ends of a transmission line usually remains under $\pi/12$ (15°) and hardly ever exceeds $\pi/6$ (30°). Hence, in normal operating
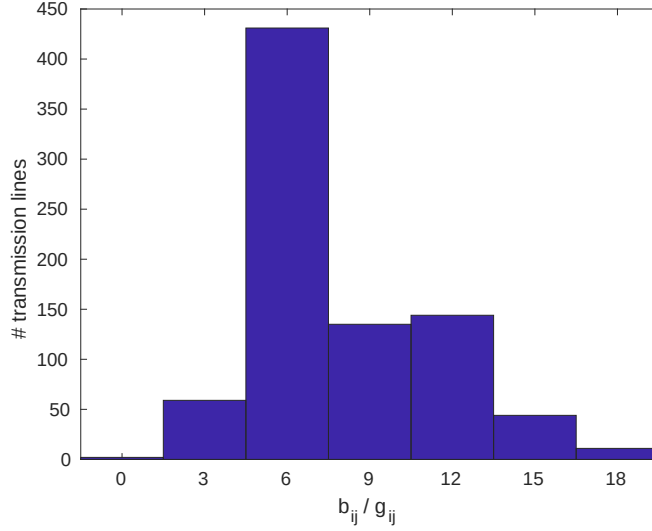
Figure 1.2 – *Ratio b_{ij}/g_{ij} for the French transmission system. When one averages over all transmission lines, one obtains $\langle b_{ij}\rangle = 8.2\,\langle g_{ij}\rangle$. Data source: [7].*

conditions, we have $\left|\theta_i - \theta_j\right| \ll 1$ and therefore we can linearized Eqs. (1.23) and (1.24), we get

$$P_i = \sum_{j\sim i} V_i V_j b_{ij}^{\mathrm{l}}\left(\theta_i - \theta_j\right) \equiv \sum_{j\sim i} P_{ij}, \tag{1.25}$$

$$Q_i = V_i \sum_{j\sim i} b_{ij}^{\mathrm{l}}\left(V_j - V_i\right) - V_i^2 \sum_{k\sim i} b_{ik}^{\mathrm{sh}} \equiv \sum_{j\sim i} Q_{ij} - V_i^2 b_i^{\mathrm{sh}}. \tag{1.26}$$

Transmission lines have a current limit known as thermal limit over which the line is overloaded an will trip off. The magnitude $\left|I_{ij}\right|$ of the current flowing through the line connecting buses #i and #i is given by

$$\left|I_{ij}\right| = \sqrt{P_{ij}^2 + Q_{ij}^2}\,/\,|V_i|. \tag{1.27}$$

Power systems are operated so that the voltage magnitudes $\left\{V_i\right\}$ remain in the narrow range 95-105% of their rated voltage $\left\{V_i^{\mathrm{r}}\right\}$. By comparing the active and reactive power flows along the line connecting buses #i and #j, we get $|Q_{ij}| \approx V_i^{\mathrm{r}} V_j^{\mathrm{r}} b_{ij}^{\mathrm{l}} \left|1 - V_i/V_j\right| \ll V_i^{\mathrm{r}} V_j^{\mathrm{r}} b_{ij}^{\mathrm{l}} \left|\theta_i - \theta_j\right| \approx |P_{ij}|$, hence the active power transmitted on a line is generally significantly higher its reactive counterpart and we get

$$\left|I_{ij}\right| \approx \left|P_{ij}\right|/V_i^{\mathrm{r}}. \tag{1.28}$$

Therefore, when investigating the power flows in normal operation conditions, we can generally discard the reactive power equations and only take into account the active power flows. Finally, on the assumption that $V_i = V_i^r$, $\forall i$, we get the power flow equations in DC approxi-

mation [8], which read

$$P_i = \sum_{j \sim i} \tilde{b}_{ij}^1 (\theta_i - \theta_j), \tag{1.29}$$

where $\tilde{b}_{ij}^1 \equiv V_i^r V_j^r b_{ij}^1$. To determine the power flowing on transmission lines of the system, firstly one must resolve the system of equations described in Eq. (1.29) for the $\{\theta_i\}$ and secondly we compute $P_{ij} = \tilde{b}_{ij}^1 (\theta_i - \theta_j)$.

1.3.1 Power transfer distribution factors (PTDFs)

These PTDFs relate the change on the power flows to the change in nodal power injections. The change on active and reactive power flows that we label $\Delta \boldsymbol{F}_P \equiv \{\Delta P_{ij}\}$ and $\Delta \boldsymbol{F}_Q \equiv \{\Delta Q_{ij}\}$ and active and reactive power injections $\Delta \boldsymbol{P} \equiv \{\Delta P_i\}$ and $\Delta \boldsymbol{Q} \equiv \{\Delta Q_i\}$ are related to the change on voltage magnitudes and phases $\Delta \boldsymbol{V} \equiv \{\Delta V_i\}$ and $\Delta \boldsymbol{\theta} \equiv \{\Delta \theta_i\}$,

$$\left[\begin{array}{c} \Delta \boldsymbol{P} \\ \Delta \boldsymbol{Q} \end{array} \right] = \left[\begin{array}{cc} \partial \boldsymbol{P}/\partial \boldsymbol{\theta} & \partial \boldsymbol{P}/\partial \boldsymbol{V} \\ \partial \boldsymbol{Q}/\partial \boldsymbol{\theta} & \partial \boldsymbol{Q}/\partial \boldsymbol{V} \end{array} \right] \left[\begin{array}{c} \Delta \boldsymbol{\theta} \\ \Delta \boldsymbol{V} \end{array} \right] \equiv \boldsymbol{J}_P \left[\begin{array}{c} \Delta \boldsymbol{\theta} \\ \Delta \boldsymbol{V} \end{array} \right], \tag{1.30}$$

$$\left[\begin{array}{c} \Delta \boldsymbol{F}_P \\ \Delta \boldsymbol{F}_Q \end{array} \right] = \left[\begin{array}{cc} \partial \boldsymbol{F}_P/\partial \boldsymbol{\theta} & \partial \boldsymbol{F}_P/\partial \boldsymbol{V} \\ \partial \boldsymbol{F}_Q/\partial \boldsymbol{\theta} & \partial \boldsymbol{F}_Q/\partial \boldsymbol{V} \end{array} \right] \left[\begin{array}{c} \Delta \boldsymbol{\theta} \\ \Delta \boldsymbol{V} \end{array} \right] \equiv \boldsymbol{J}_F \left[\begin{array}{c} \Delta \boldsymbol{\theta} \\ \Delta \boldsymbol{V} \end{array} \right], \tag{1.31}$$

where $\boldsymbol{J}_F$ and $\boldsymbol{J}_P$ are Jacobian matrices. From Eqs. (1.30) and (1.31), we get

$$\left[\begin{array}{c} \Delta \boldsymbol{F}_P \\ \Delta \boldsymbol{F}_Q \end{array} \right] = \boldsymbol{J}_F \boldsymbol{J}_P^{-1} = \left[\begin{array}{c} \Delta \boldsymbol{P} \\ \Delta \boldsymbol{Q} \end{array} \right], \tag{1.32}$$

$\boldsymbol{\Psi}_{\mathrm{AC}} \equiv \boldsymbol{J}_F \boldsymbol{J}_P^{-1}$ is the AC PTDF matrix. The Jacobian matrices $\boldsymbol{J}_F$ and $\boldsymbol{J}_P$ are evaluated at a known initial configuration and generally the AC power transfer distribution factors are only valid in the vicinity of this initial configuration. Nevertheless in the DC power flow, the PTDFs can be determined once and for all. In the following we derive their expression in this approximation.

We assign each line an arbitrary orientation, namely one of is extremities becomes its start and the other its end. The incidence matrix $\boldsymbol{A}$ corresponding to the oriented graph of a power system is given by

$$a_{ik} = \left\{ \begin{array}{ll} -1, & \text{if line } \#k \text{ starts at bus } \#i, \\ 1, & \text{if line } \#k \text{ ends at bus } \#i, \\ 0, & \text{otherwise.} \end{array} \right. \tag{1.33}$$

We observe that $\boldsymbol{A}^\top \mathbb{1}_{N \times 1} = \mathbb{0}_{N \times 1}$, where are $\mathbb{1}_{N \times 1}$ and $\mathbb{0}_{N \times 1}$ are the N-vectors with all entries equal to 1 and 0 respectively. We drop the P index and label $F_k \equiv P_{ij}$ the active power flowing on the line $\#k$ connecting buses $\#i$ to $\#j$ and $b_k \equiv \tilde{b}_{ij}^1$ its susceptance. From Eqs. (1.23) and (1.25), the power injection $\boldsymbol{P} = \left[P_1, \cdots, P_N \right]^\top$ and the power flows $\boldsymbol{F} = \left[F_1, \cdots, F_{N_l} \right]^\top$ are related

to the voltage phases $\boldsymbol{\theta} = \left[\theta_1, \cdots, \theta_N\right]^\top$ by

$$\boldsymbol{P} = \boldsymbol{B}\boldsymbol{\theta}\,, \tag{1.34}$$

$$\boldsymbol{F} = \mathrm{diag}\big(\{b_k\}\big)\boldsymbol{A}^\top\boldsymbol{\theta}\,. \tag{1.35}$$

From Eqs. (1.25) and (1.33), we have $\boldsymbol{B} = \boldsymbol{A}\,\mathrm{diag}\big(\{b_k\}\big)\boldsymbol{A}^\top$ and therefore $\boldsymbol{B}\,\mathbb{1}_{N \times 1} = \mathbb{0}_{N \times 1}$. We note that $\mathbb{1}_{N \times 1}$ is an eigenvector of $\boldsymbol{B}$ associated with the eigenvalue zero, that $\boldsymbol{B}$ is a singular matrix and that $\mathbb{1}_{N \times 1}$ spans the kernel of $\boldsymbol{B}$.[1] Pseudoinverses, we label them with †, are the generalization of inverses for singular matrices. They are not uniquely defined, nevertheless, every pseudoinverse $\boldsymbol{B}^\dagger$ becomes injective if one restricts its codomain to the image of $\boldsymbol{B}$ and therefore $\boldsymbol{A}^\top\boldsymbol{B}^\dagger\boldsymbol{P}$ is independent of the choice of the pseudoinverse as along as $\sum_i P_i = 0$, which is always satisfied in DC approximation. Physically, the non-uniqueness of the pseudoinverse is related to the gauge freedom, the freedom to choose the reference phase with respect to which one defines all bus phases in the system. Hence, in DC approximation, the power flows $\boldsymbol{F}$ are related to the nodal power injections $\boldsymbol{P}$ by

$$\boldsymbol{F} = \mathrm{diag}\big(\{b_k\}\big)\boldsymbol{A}^\top\boldsymbol{B}^\dagger\boldsymbol{P} \equiv \boldsymbol{\Psi}\boldsymbol{P}\,, \tag{1.36}$$

where $\boldsymbol{\Psi}$ is the DC PTDF matrix.

In Section 2.1.1, our dispatch algorithm uses Eq. (1.36) to obtain the power flows in the pan-European grid from power injections. It optimizes the production of dispatchable energy sources whiles guaranteeing that the power flows remain below their thermal limits.

---

[1] We assume that the graph of the transmission grid is connected, which implies that $\boldsymbol{B}$ has a single eigenvector associated with the eigenvalue zero.

The future of the electricity sector in Europe: a physico-economic investigation

Part I

2 The future of the electricity sector in Switzerland and in Europe

Most European countries are now engaged in the energy transition. New RES are considerably modifying our electricity generation and they compete the conventional productions. Their increasing penetration will results in a growing inbalance between the electricity generated by non-dispatchable sources and the electricity demand which forces the conventional sources to produce with more flexibility. To investigate these issues, we develop a dispatch algorithm on an aggregated model of the pan-European power grid which generates yearly production profiles for different dispatchable technologies. In Section 2.1, we detail how we obtain our aggregated model of the pan-European transmission grid. We explain how we model the different production technologies and how our economic dispatch works. We calibrate our model by trying and reproducing the historical production profiles of the year 2015. We obtain a surprisingly good agreement between our power dispatches and historical productions. Having calibrated our model, we investigate, in Section 2.2, the future production profiles in future situations with high penetrations of new RES in most European countries. In particular, we focus our investigation on conventional (dam) hydroelectricity, the only flexible renewable energy source, and pumped storage, the most mature technology for electricity storage. In Section 2.3, we adapt our model to investigate the congestion in the Swiss transmission grid. To address this problem, we incorporate the actual Swiss grid in our aggregated grid. The model and most of the results presented in this chapter were published in Refs. [9, 10].

2.1 An aggregated pan-European optimal power dispatch model

Aggregated models are used for systemic investigations where fully accurate power flows are not crucial and geographically resolved production and load data are hard to obtain. How these models are obtained depends on their purposes and the available information on the power systems being reduced. Aggregation procedures that preserve as much as possible the system structure and the power flows are presented in Refs. [11, 12, 13]. These reduction methods require detailed spatial information on the production and consumption locations and the structure of the grid. However, usually only aggregated national production and load profiles are publicly available [14], we therefore develop an aggregated model whose structure

is mainly given by the spatial resolution of the accessible data.

Fig. 2.1 shows our aggregated European grid, each node representing an independent dispatch zone. This model was designed to study the effects of the energy transition on Swiss electricity sector. As Switzerland is located between electricity exporting countries, France and Germany, to the north and an importing country, Italy to the south, most of the power flows are transiting North-South through Switzerland. There are several possible parallel paths that the electric power can take to transit from North to South and we want our model to take them into account. Portugal is solely connected to Spain, they are therefore aggregated in the same zone. Benelux countries are importing countries, we aggregate them in a single zone. We separate the Tyrol from Austria, because this splitting gives us a better agreement between historical and simulated power flows transiting through the Austria-Switzerland border.
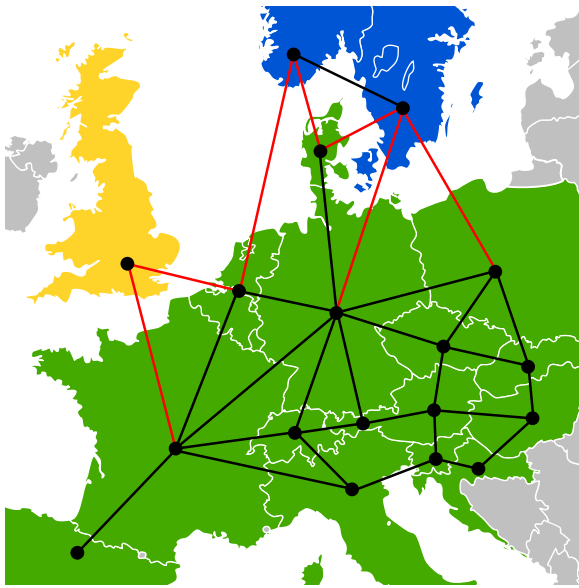

Figure 2.1 – *Aggregated model of the Central and Northern European grid. Each node represents a dispatch zone. The lines represent interconnections: AC connections are in black and DC connections in red. Synchronous areas are displayed in different colors.*

AT-AT	2.5	ES-FR	2.9
AT-DE	3.6	FR-IT	3.6
AT-CH	4.3	FR-NL	4.0
AT-CZ	2.9	HR-HU	3.2
AT-HU	2.9	HR-SI	2.5
AT-SI	3.6	HU-SK	2.2
CH-DE	6.5	IT-SI	1.4
CH-FR	7.5	NO-SE	3.6
CH-IT	5.8	PL-SK	2.2
CZ-DE	4.3	DE-SE	0.6
CZ-PL	2.9	DK-NO	1.6
CZ-SK	3.6	DK-SE	1.3
DE-DK	2.9	FR-UK	2.0
DE-FR	6.1	NL-NO	0.7
DE-NL	6.4	NL-UK	1.0
DE-PL	4.3	PL-SE	0.6

Table 2.1 – *Thermal limit power of each connection in GW which are given by the sum of the physical lines they represent. Source: own assessment.*

2.1.1 Interregional power flows

Fig. 2.1 shows the three AC synchronous areas that are considered in our model and the DC connections forming the pan-European transmission grid. In the following, we describe how we model AC and DC connections. In order to describe the power flows on AC connections, we must obtain effective admittances for them. Aggregation of power systems has a relatively long history [15, 16, 17, 18]. Traditionally, reduction methods were used by TSOs to aggregate portions of the grid which were out of their control but have influence on the power flowing in their grids [15, 16]. Recently, reduction methods were used to obtain simple equivalent systems

for systemic investigations [17, 18]. Existing reduction methods cannot be applied to our problem because they require detailed knowledge on the characteristics of the transmission grid we want to reduce, in particular its geometry, the electrical parameters of transmission lines and the locations of producers and consumers. In fact, we find that an equivalent system obtained by these methods for a winter configuration poorly assess the power flows in summer and vice versa. We circumvent this difficulty by finding the aggregated admittances corresponding to our aggregated model that give the best agreement between the historical yearly international power flow profiles and those computed with our aggregated model.

In Section 1.3 we showed that, within the DC lossless approximation, the power flows in an AC transmission system are related to the power injections by the DC PTDF matrix

$$\boldsymbol{\Psi}(\{b_k\}) = \mathrm{diag}(\{b_k\}) \boldsymbol{A}^\top \left(\boldsymbol{A} \mathrm{diag}(\{b_k\}) \boldsymbol{A}^\top \right)^\dagger. \tag{2.1}$$

In our model, as in most actual power market auctions, time is discretized hourly, $\Delta t = 1\mathrm{h}$, we define $t_n = n\Delta t$. For a given set of line admittances $\boldsymbol{b} = \{b_1, \cdots, b_{N_l}\}$, we can compute mismatch between the historical power flows $\boldsymbol{F}_n^\mathrm{h} \equiv \boldsymbol{F}^\mathrm{h}(t_n)$ and those obtained with the PTDF matrix $\boldsymbol{\Psi}(\{b_k\})$ and historical power injections $\boldsymbol{P}_n^\mathrm{h} \equiv \boldsymbol{P}^\mathrm{h}(t_n)$ in the transmission grid and we define the admittances $\boldsymbol{b}$ for the AC connections in our model as those which minimize this mismatch over the year,

$$\boldsymbol{b} = \underset{b_k \in]0,1]}{\mathrm{argmin}} \sum_n \left\| \boldsymbol{\Psi}(\{b_k\}) \boldsymbol{P}_n^\mathrm{h} - \boldsymbol{F}_n^\mathrm{h} \right\|^2. \tag{2.2}$$

This minimization is carried out numerically with 2015 historical national productions and loads and international power flows taken from ENTSO-E database [14]. Thermal limits $\{F_{\max k}\}$ of connections are given by the sum of the thermal limits of the physical lines they represent, their values are listed in Table 2.1. The PTDF matrix elements corresponding to the Scandinavian and UK grids are trivial because of their aggregated geometries.

The power flow on a DC connection depends on the setpoints of the power electronics at each end which are controlled by transmission grid operators. Therefore they can take arbitrary values in their rated power range $\left[-F_{\max k}, F_{\max k} \right]$. In our model, we represent a DC connection as a modification of the power balance in the zones at its extremities, it acts as a power "sink" at an end and a power "source" at the other end. The modification of the power balance P_i^dc in the zone #i due to DC connections reads

$$P_i^\mathrm{dc}(t) = \sum_k a_{ik}^\mathrm{dc} F_k^\mathrm{dc}(t), \tag{2.3}$$

where $\boldsymbol{A}^\mathrm{dc}$ is the incidence matrix corresponding to the DC connections and F_k^dc is the flow on DC connection #k [for the definition of an incidence matrix, see Eq. (1.33)]. Electricity transmission on a DC connection is also assumed to be lossless. In a power system consisting in distinct synchronous areas, the PTDF matrix $\boldsymbol{\Psi}$ of the whole system is block diagonal and is

given by

$$\mathbf{\Psi} = \bigoplus_\alpha \mathbf{\Psi}_\alpha, \tag{2.4}$$

where $\oplus$ denotes the direct sum operation and Ψ_α is the PTDF matrix of the synchronous area #α. Power injections $P_i^{\text{inj}}(t)$ in the pan-European transmission depend on the dispatchable $P_i^{\text{disp}}(t)$ and the non-dispatchable P_i^{ndisp} productions, on the zonal load L_i and on the possible curtailment $C_i(t)$ of new RES all of which are described in the following paragraphs, $P_i^{\text{inj}}(t)$ reads

$$P_i^{\text{inj}}(t) = P_i^{\text{disp}}(t) + P_i^{\text{ndisp}}(t) - L_i(t) - C_i(t) + P_i^{\text{dc}}(t). \tag{2.5}$$

As we assume a lossless electricity transmission, we obtain that the total production is equal to the total consumption at any time, this leads to

$$\sum_i P_i^{\text{inj}}(t) = 0, \ \forall t. \tag{2.6}$$

2.1.2 Production and consumption

National productions and loads are aggregated within each dispatch zone and attributed to the corresponding node. Power productions are subdivided into two sets. They are,

- **Non-dispatchable productions**, mostly consisting of run-of-the-river (RoR)[1], solar photovoltaics (PV) and wind turbine productions. The remaining non-dispatchable productions, mainly combined heat and power (CHP), are grouped into "miscellaneous production".
- **Dispatchable productions**: are divided in 6 technologies: (i) dam hydroelectricity, (ii) pumped-storage hydroelectricity, (iii) gas and oil, (iv) nuclear, (v) hard coal and (vi) lignite productions.

We differentiate dispatchablity which is the ability of a technology to produce electricity on demand and flexibility which is the ability of a dispatchable technology to vary its production rapidly.

For each zone and at each time, we define the residual loads $R_i(t)$ as the difference between the load and the non-dispatchable productions,

$$R_i(t) = L_i(t) - P_i^{\text{ndisp}}(t), \tag{2.7}$$

where $L_i(t)$ and $P_i^{\text{ndisp}}(t)$ respectively give the load and the sum of the non-dispatchable productions at time t in the zone #i. The task of our economic dispatch is to distribute the

---

[1]RoR is to some extent dispatchable. However, for the sake of simplicity, we decide to treat RoR as non-dispatchable in this work.

electricity generation over all dispatchable productions so that their production is equal to the total residual load at all times. This is equivalent to satisfy the balance condition that consumption is equal to production at all times.

The association of European transmission grid operators (ENTSO-E) provides data on historical production and load profiles and installed capacities in the different countries [14] and forecasts for annual RES productions [19, 20] that we use to set up our model.

Thermal productions

Fuel scarcity is not taken into account in our model, it is assumed that thermal generators[2] can always produce. The only limitations on thermal productions are that their production $P_i^s(t)$ cannot exceed their installed capacity $P_{\max i}^s$ of the technology #s in the zone #i, which reads

$$0 \leq P_i^s(t) \leq P_{\max i}^s, \tag{2.8}$$

and that the hourly variations of $P_i^s(t)$ are capped by their maximal ramping rate r^s which depends on the technology

$$\left| P_i^s(t + \Delta t) - P_i^s(t) \right| \leq r^s P_{\max i}^s. \tag{2.9}$$

The values of r^s we use in this work are given in Table 2.2.

Conventional dam hydroelectricity

Dam hydroelectricity is also subject to the constraints described in Eqs. (2.8) and (2.9). Furthermore, dam storage capacity is limited and dam productions must be optimized so that its storage never run dry or exceed their maximal capacity $S_{\max i}^{\text{dam}}$, hence the filling $S_i^{\text{dam}}(t)$ of the storage is subject to

$$0 \leq S_i^{\text{dam}}(t) \leq S_{\max i}^{\text{dam}}, \ \forall i. \tag{2.10}$$

Dam power plants generate electricity thanks to their water intake $I_i(t_n)$ which they collect in their storage. The filling $S_i^{\text{dam}}(t)$ of their storage evolves hourly as

$$S_i^{\text{dam}}(t_n + \Delta t) = S_i^{\text{dam}}(t_n) + \left[I_i(t_n) - P_i^{\text{dam}}(t_n) \right] \Delta t. \tag{2.11}$$

For our simulations, we use typical water intakes for dams in the Alps [21]. We assume that they will not change significantly for the next decade. Conventional dam power plants produce an amount of electricity equivalent to the multi-annual average of the water intake in their storage. To take this feature into account, we impose the periodic boundary condition that

---

[2]Thermal generators consist in dispatchable technologies (iii) to (vi).

$$S_i^{\mathrm{dam}}\big(t=0\big) = S_i^{\mathrm{dam}}\big(t=8760\mathrm{h}\big).$$

Pumped-storage (PS) hydroelectricity

PS hydroelectricity is the most-mature electricity storage technology. Electricity is consumed to pump water into a reservoir, water that is later flowed through a turbine to generate electricity. PS hydroelectricity is subject to constraints similar to those on conventional dam hydroelectricity. The reservoir filling depends on the pump/turbine power profiles $P_{\mathrm{p}i}^{\mathrm{ps}}(t)$ and $P_{\mathrm{t}i}^{\mathrm{ps}}(t)$ and evolves as

$$S_i^{\mathrm{ps}}(t+\Delta t) = S_i^{\mathrm{ps}}(t) + \left[\eta P_{\mathrm{p}i}^{\mathrm{ps}}(t) - \eta^{-1} P_{\mathrm{t}i}^{\mathrm{ps}}(t) \right] \Delta t , \tag{2.12}$$

with a typical pump/turbine efficiency of $\eta = 0.9$ (each way, see [22, 23]). The water intake in PS storage is usually negligible and we omit it in our model. In this work, electricity storage relies only on the pumped-storage which is the only mature technology of large-scale storage [23], used since more than 50 years. The operation of several storage technologies can be described by similar constraints [24].

Curtailment of new RES productions

With a large penetration of new RES, their productions might congest international connections leading to situations where the limit flows constraints are unsatisfiable. We therefore give the opportunity to our economic dispatch to curtail the new RES production. The curtailment $C_i(t)$ must satisfy

$$0 \le C_i(t) \le P_i^{\mathrm{pv}}(t) + P_i^{\mathrm{wind}}(t) . \tag{2.13}$$

From Eqs. (2.6) and (2.7), we have

$$\sum_i \left(P_i^{\mathrm{disp}}(t) - C_i(t) \right) = \sum_i R(t) , \ \forall t . \tag{2.14}$$

Hence, the dispatchable sources must be engaged to sustain the total residual load at any time. The task of our dispatch algorithm is to obtain their production profiles that minimize the global annual generation cost. It also minimizes addition costs which depend on the pumped-storage use, new RES curtailment and power flows.

2.1.3   Economic dispatch

A large number of different optimized power flows algorithms exist [25, 26, 27, 28, 29]. Our dispatch algorithm is a minimization process that takes into account different costs which are listed below.

Generation costs

Our dispatch algorithm minimizes the generation costs. A marginal cost a^s and a repulsion cost b^s is assigned to each technology #s. The repulsion cost does not directly correspond to any real economic costs, it progressively increases the total production cost as the production increases and reaches its maximal possible value. However, we found that they are necessary to reproduce historical time series faithfully. The values of $\{a^s\}$ and $\{b^s\}$ we use in our simulation are listed in Table 2.2.

The generation cost in the zone #i at each time step $\Delta t = 1$h is given by a sum over the marginal and repulsion costs for all technologies as

$$W_i(t) = \sum_s \left[a^s P_i^s(t) + b^s P_i^s(t)^2 / P_{\max i}^s \right] \Delta t, \tag{2.15}$$

technology	$a^s \left[\text{GWh}^{-1}\right]$	$b^s \left[\text{GWh}^{-1} P_{\max}^{-1}\right]$	$r^s \left[\text{h}^{-1}\right]$
dam	90	18	1.0
gas	90	60	1.0
nuclear	25	20	0.2
hard coal	35	35	0.2
lignite	20	20	0.1

Table 2.2 – *Effective parameters describing the different dispatchable technologies. The marginal costs $\{a^s\}$ are loosely based on those found in Ref. [27]. The effective ramp rates $\{r^s\}$ and repulsion costs $\{b^s\}$ have been calibrated so that production profiles reproduce historical data qualitatively.*

Curtailment costs

A prohibitive marginal cost $a^{\text{curtail}} = 1000[\text{GWh}^{-1}]$ is assigned to the curtailment, so that new RES are curtailed only if they make the optimization infeasible.

Pumped-storage revenues

Pumped-storage (PS) power plants have no marginal cost. Electricity prices give them the signal whether they must pump or generate and its variations allows them to generate profits. In Chapter 3, we show that we can define an effective electricity price $p_{\text{eff}\,i}(t)$ based on the residual load $R_i(t)$, which is defined in Eq. (2.7). Here, the effective price $p_{\text{eff}\,i}(t) \propto R_i(t)$ is normalized to be consistent with the parameters in Table 2.2. In the zone #i, the revenues $G_{\text{PS}\,i}$ generated by PS hydroelectricity depend on its pump/turbine power profiles $P_{\text{p}\,i}^{\text{ps}}(t)$ and $P_{\text{t}\,i}^{\text{ps}}(t)$ and are given by

$$G_i^{\text{ps}} = \sum_n p_{\text{eff}\,i}(t_n) \left[P_{\text{t}\,i}^{\text{ps}}(t_n) - P_{\text{p}\,i}^{\text{ps}}(t_n) \right] \Delta t, \tag{2.16}$$

We define the cost function W_{PS} for PS operations as

$$W_{\mathrm{PS}} = -\sum_i G_i^{\mathrm{ps}}. \tag{2.17}$$

Our economic dispatch maximizes the revenues of PS power plants.

Reliability cost (or line aging cost)

Transmission system operators (TSOs) are reluctant to allow power dispatches that induce power flows on transmission lines which are close to their thermal limits. The underlying reasons are that it increases the probability of cascading failures and that it causes premature aging of the transmission lines. When such situations occur, TSOs may ask a redispatch of the power generation to mitigate the power flows on their lines. The power flows $\boldsymbol{F} = \left[F_1, \cdots, F_{N_l} \right]$ depend on the power injections in the transmission grid which are the differences between zonal dispatchable productions and residual loads

$$\boldsymbol{F}(t) = \boldsymbol{\Psi}\,\boldsymbol{P}^{\mathrm{inj}}(t), \tag{2.18}$$

where Ψ is the PTDF matrix defined in Eq. (2.4) and $\boldsymbol{P}^{\mathrm{inj}}(t) \equiv \boldsymbol{P}^{\mathrm{disp}}(t) - \boldsymbol{C}(t) - \boldsymbol{R}(t) + \boldsymbol{P}^{\mathrm{dc}}(t)$ are the power injections in AC synchronous grids. Our economic dispatch engages the productions in increasing order of generation costs until a connection reaches its thermal limit.

$$W_{\mathrm{F}} = \sum_{k,n} \left(c_k^{\mathrm{F}} F_k(t_n) / F_{\mathrm{max},k} \right)^2, \tag{2.19}$$

where c_k^{F} is the costs related to operations of the line #k. In principle, it depends on different characteristics of the connection as its length, the number and the voltage of the physical lines. We assume the costs to be uniform $c_k^{\mathrm{F}} \equiv c_{\mathrm{F}}$. This cost prevents the flows to grow too close to their maximal value. By increasing the cost c_{F}, one can force each zone to produce electricity in quasi-autarky and significantly decrease the power exchanges in the pan-European grid.

Problem formulation

In summary, our economic dispatch finds the production profiles of the dispatchable sources that minimizes the total cost function

$$W = \sum_{i,n} W_i(t_n) + W_{\mathrm{PS}} + W_{\mathrm{F}} + W_{\mathrm{C}}, \tag{2.20}$$

under the following constraints:

Power limits $P_i^s(t) \leq P_{\mathrm{max}\,i}^s$, $\forall t$; the power generated never exceeds its maximal installed capacity.

Ramp rates $|\partial P_i^s(t)/\partial t| \leq r^s\, P_{\mathrm{max}\,i}^s$, $\forall t$; each technology has a maximal ramp rate r^s at which

the production increases or decreases. These ramp rates are similar, but not exactly equal, to the real, technical rates. We adapted them slightly when calibrating our model, to better reproduce historical production time series.

Internodal power flows $|F_k(t)| \leq F_{\max k}$; they should never exceed their thermal limit $F_{\max k}$.

Dam storage Dam hydroelectric plants are constrained by the finiteness of their reservoir and the annual water intake.

Our economic dispatch is equivalent to a quadratic programming problem [30] with the form

$$\min \boldsymbol{x}^\top \boldsymbol{Q} \boldsymbol{x} + \boldsymbol{c}^\top \boldsymbol{x}, \tag{2.21}$$
$$\text{s.t. } \boldsymbol{A}_{\text{eq}} \boldsymbol{x} = \boldsymbol{b}_{\text{eq}},$$
$$\boldsymbol{A} \boldsymbol{x} \leq \boldsymbol{b},$$

which is resolved with an optimization software, we use *Gurobi solver* [31].

2.1.4 Model calibration

The last step of the elaboration of our model is to calibrate it which is carried out by trying and reproducing the historical production profiles of the year 2015. In the calibration process, we slightly vary the initial values of effective parameters $\{a^s\}$, $\{b^s\}$ and $\{r^s\}$ to maximize the agreement between our power dispatches and historical productions. Their final values are reported in Table 2.2.

In Fig. 2.3 we show the results for a winter and a summer week in Germany, Italy, Poland and France, after the optimization of effective parameters. The agreement between dispatched and actual productions is excellent for an aggregated power dispatch model. We find comparable agreements in the other countries. Fig. 2.2 illustrates that our model qualitatively reproduce the productions of Swiss and Norwegian dam hydroelectricity. The production dispatches of the most flexible technologies are hard to predict as they can strongly vary from hour to hour. From Fig. 2.3 and 2.2, we conclude that our model is calibrated and fully validated and we use it to investigate future scenarios of the energy transition. We are unaware of another model that captures the national generation profiles with that level of accuracy at an European scale.
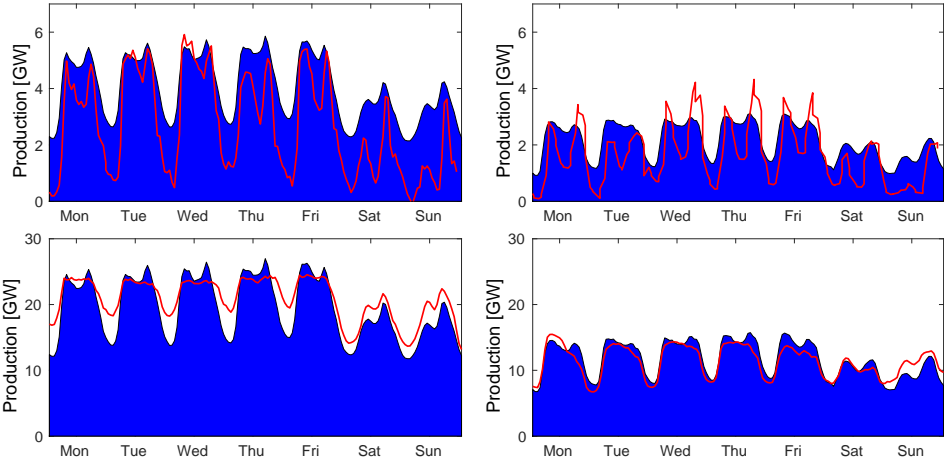
Figure 2.2 – *Dam production of Switzerland (top) and Norway (bottom) for a week in winter (left) and summer (right) in 2015. Dispatched productions are displayed in blue and actual 2015 production profiles are in red.*
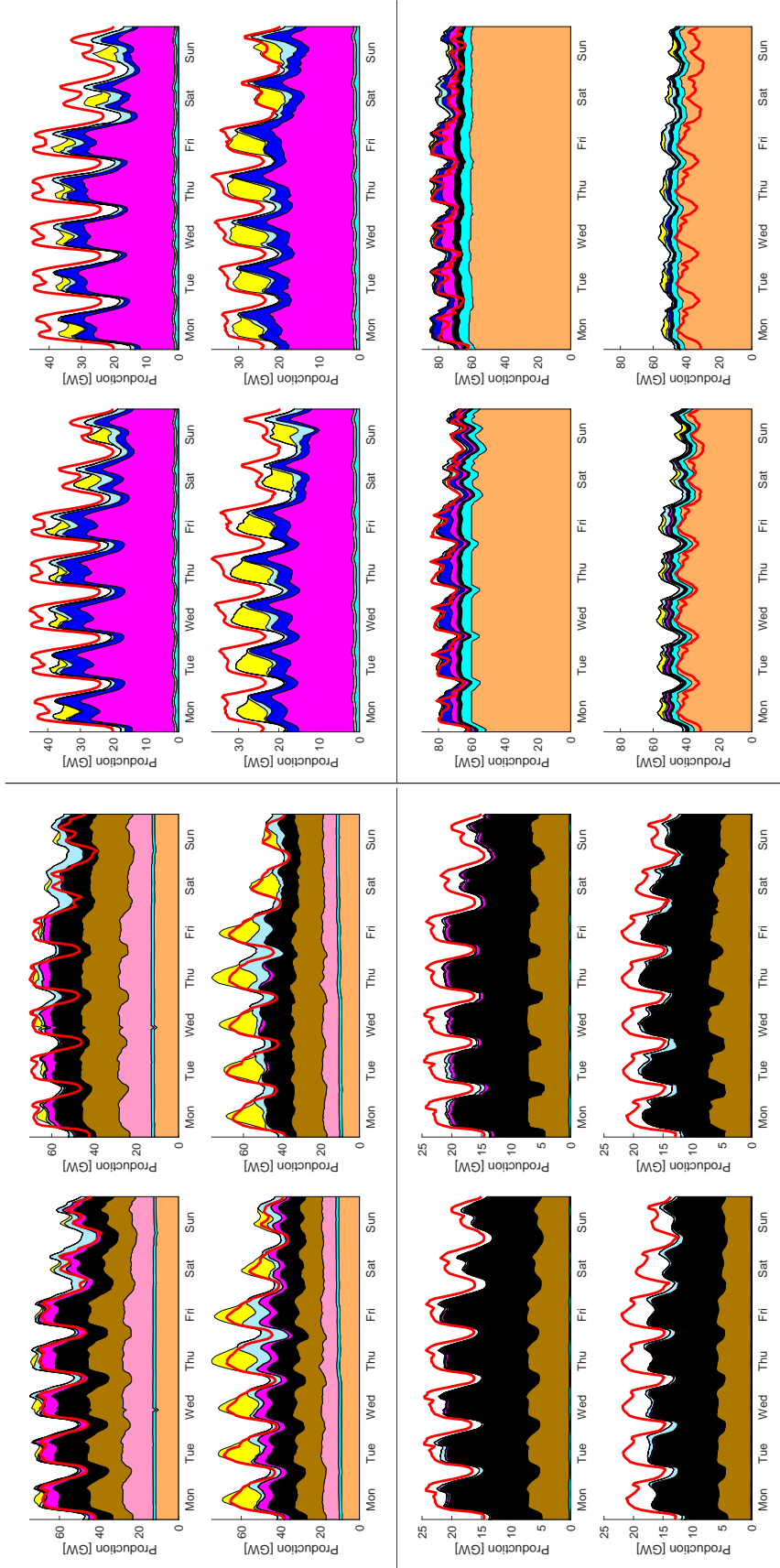
Figure 2.3 – *Dispatched (left column in each group of four panels) and actual 2015 (right column in each group of four panels) productions in Germany (top, left group), Italy (top, right), Poland (bottom, left) and France (bottom, right) for a winter week (top row in each group) and a summer week (bottom row). Technologies are color-coded as follows: nuclear (orange), RoR (cyan), miscellaneous (pink), lignite (brown), hard coal (black), gas (purple; including hard coal in Italy), dam (blue), wind (light blue) and PV (yellow). The red curve indicates the 2015 national loads.*

25

2.1.5 Similar models

The characteristics of the models describing the electricity sector depends on their purposes. Models used in long term planning of the extension of the European grid [32, 33] significantly differ from those used by electrical engineers for N-1 contingencies [34, 35]. In more general investigations on energy consumption, electricity grids can be coupled to other energy systems, for instance to natural gas networks [36].

An exhaustive review of the models of the European electricity sector is beyond the scope of this work. We list below a few models that are relatively similar to the one we developed. Rodriguez et al. used an aggregated model of the European grid to optimize its extension while minimizing the required backup of conventional sources [28]. Schaber et al. investigate the future revenues of different technologies with an aggregated model [26]. Schwippe et al. developed an aggregated dispatch model to study the future extension of the pan-European transmission grid [29]. Hörsch et al. developed a PyPSA, a load flow software, which includes an aggregated model of Europe [37]. Comaty et al. developed an aggregated model which has a higher spatial resolution (regional distpatch zones) in Switzerland [27].

Our model has some attractive features that most of the previously mentioned models do not incorporate. It is reproducing the historical production profiles with good fidelity. The power flows in AC grids are obtained with power transfer distribution factors (PTDFs) which reproduce the historical power flows profiles. Energy storage (pumped-storage in our model) is dispatched thanks to an effective electricity price.

2.2 Future power dispatches and international flows in Europe

In this section we investigate future production dispatches in a scenario with large penetration of new RES in most European countries corresponding to the year 2030. Some assumptions on the evolution of national loads and installed capacities of the different technologies must be made. We choose to use 2015 national loads without modifying them. We assume that the increase of electricity demand due to population growth and sustainable transport is more or less canceled by higher efficiency of appliances. The future new RES production profiles are obtained from the 2015 profiles which are scaled up to match the annual generation predicted in *ENTSO-E 2030 Vision 4 of European Green Revolution* [20]. For conventional sources, we take their installed capacities from the same ENTSO-E scenario. We deliberately choose a scenario with a high penetration of new RES in the European energy mix. The underlying idea is that if the pan-European power system can handle a new RES oriented scenario, it can handle any scenario with lower penetration of new RES.

Fig. 2.4 shows the productions of Germany, Italy, Switzerland and Norway for two consecutive weeks in the winter of the year 2030. One sees first that when new RES production is low (first five days), dam hydro productions are high to help supplying the electricity demand. When new RES productions are high, dam hydro production is significantly lowered. In particular,

one sees that, with large new RES productions, Switzerland continuously imports electricity during several consecutive days, which is never the case nowadays. Pump-storage hydro is additionally intensively used, as it produces a lot when RES produce little and consumes (pumps) when RES productions are high.
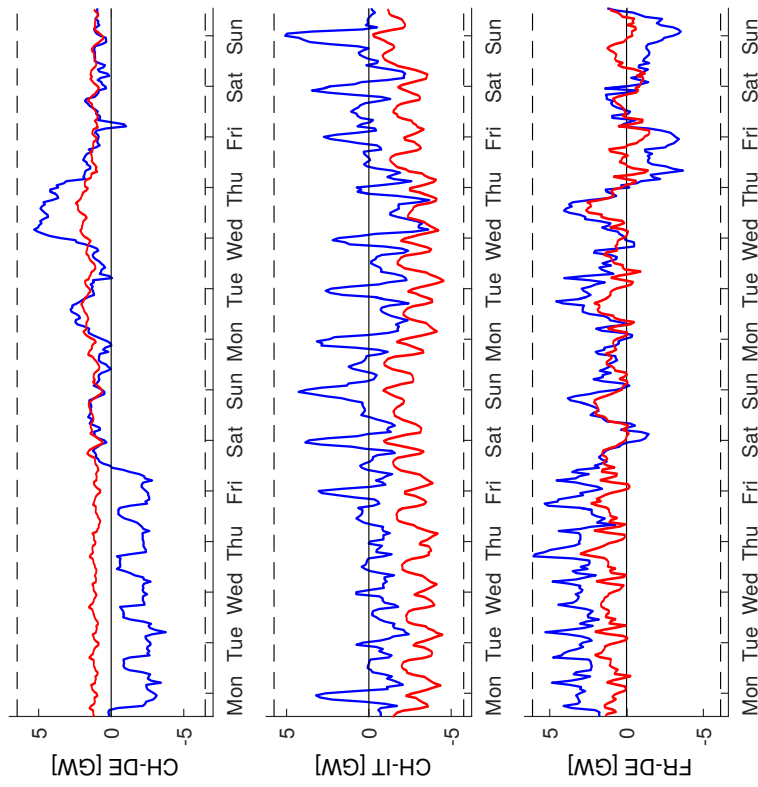
Figure 2.4 – *Top to bottom: electricity productions of Germany, Italy, Switzerland and Norway for two winter weeks in 2030. Color convention is as in Fig. 2.3, with additionally, pump-storage production (turquoise) and PS pumping additional load (green line).*

Figure 2.5 – *Top to bottom: power flows between Switzerland and Germany, Switzerland and Italy and France and Germany in 2015 (red) and 2030 (blue). The thermal limit power of each connection is indicated by a dashed line.*
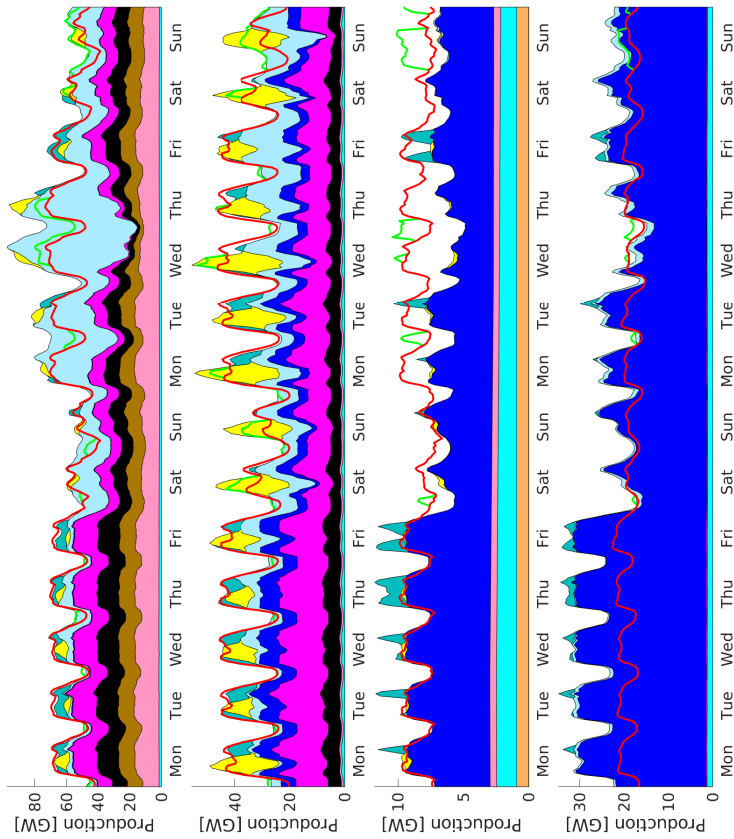
Fig. 2.5 shows the power flow of three important AC connections in the continental European grid for the same two weeks. For comparison we added the power flows obtained for 2015 for the same period. We observe that the power flows in 2015 tend to have a dominant direction, for instance, the connection between Switzerland and Italy is used for Italian import only. Whereas in 2030, the increased Italian PV capacity results in a reversed flow across this connection. It is clear that large new RES productions induce increased power exchanges between European countries, often reversing the direction of the power flows. This leads to situations where the power flows are regularly close to their thermal limits and sometimes in an unexpected direction.

Fig. 2.6 shows the production of the same countries for a summer week. It illustrates the role of PS plants in the 2030 pan-European power dispatches. During summer weeks, PS plants will work at close to maximal capacity on an almost daily basis. They generate in the morning and in the evening when load is high and the PV production is not at its peak. At noon PS pumps consume electricity to refill their storage. We conclude that PS plants will play a crucial role in the mitigation of daily new RES production fluctuations. The power exchanges among the European countries are intense, each displayed country exports 7GW or more at some point in time during the week. More flexibility is asked to the dispatchable technologies, the most flagrant example is the change in the Italian gas and dam hydro production dispatches between 2015 and 2030, compare Fig. 2.6 with Fig. 2.3. Finally no curtailment of new RES is present in Figs. 2.4 and 2.6. Indeed, only about 1% of new RES yearly production in Europe is curtailed. This means that the power exchanges and PS hydroelectricity operations are able to absorb the large peaks of the new RES productions.
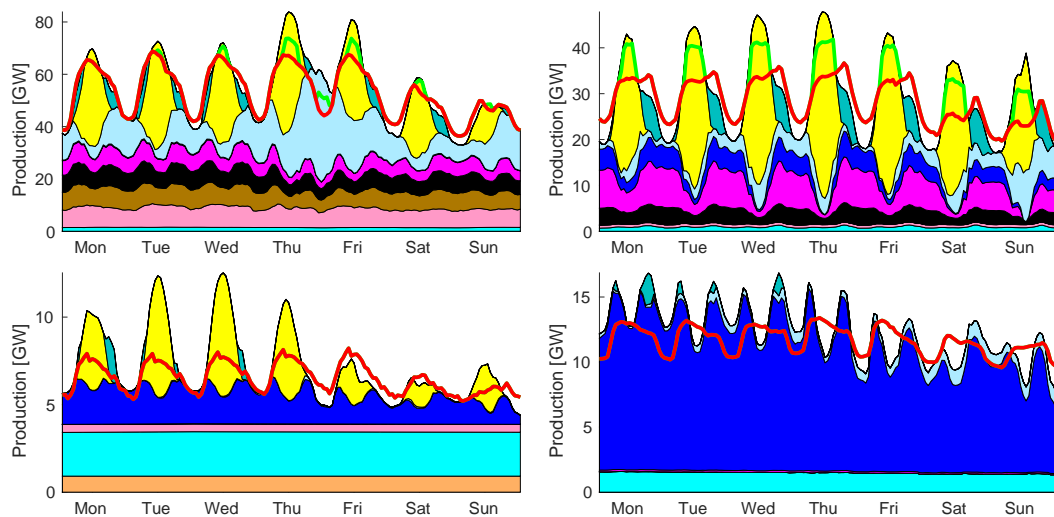

Figure 2.6 – *Top to bottom: electricity productions of Germany, Italy, Switzerland and Norway for a summer weeks in 2030. Color convention is as in Fig. 2.4, with additionally, pump-storage production (turquoise) and pump-storage consumption (pumping; green line).*

In conclusion, our investigations show that significant higher penetrations of new RES can be

achieved in the European mixes without major enhancements of the existing pan-European transmission grid. Nevertheless, some reinforcements mainly on North-South connections will be required to prevent their flows to exceed their thermal limits too often. The PS hydroelectricity will have a decisive role for the mitigation of the variations of the new RES productions on a daily basis. In the next section, we show that a few reinforcements can resolve the future congestion of the Swiss transmission system due to the increasing penetration of new RES in Switzerland and in Europe.

2.3 Future reliability of the Swiss transmission grid

Swissgrid, the owner and operator of the Swiss transmission network, has recently presented its strategic grid 2025, which is the network it requires to guarantee the reliability of the grid and to allow electricity to be exchanged indiscriminately. The strategic grid 2025 differs from the present configuration by about ten reinforcements, for a complete list see Ref. [38]. The main enhancements are stronger East-West and North-South connections. In this section, we study the future reliability of the Swiss transmission grid. In this section, we perform an independent analysis of the strategic grid 2025, we compare it with the present configuration of the grid.

We build two scenarios, corresponding to the year 2030, with high penetrations of new RES in the Swiss and European energy mixes. We assume that the capacity of dam hydroelectricity remains unchanged, that all nuclear power plants, except Leibstadt, are decommissioned and that the energy transition in Switzerland will mainly rely on solar power to replace nuclear production. To do so, our first scenario relies on solar power exclusively. In the second scenario, we reduce the PV production by 4 TWh which are produced by about 600 large wind turbines instead. In both scenarios the annual RES production is 17 TWh, corresponding to the average annual production of the decommissioned nuclear power plants. The characteristics of our two scenarios are summarized in Table 2.3. For the European productions, as previously, we base our scenarios on *ENTSO-E 2030 Vision 4 of European Green Revolution* [20].

	PV [TWh]	WT [TWh]
100% PV scenario	17	0
RES mix scenario	13	4

Table 2.3 – *Swiss PV and wind turbine (WT) annual productions in the 2 scenarios considered in this report.*

2.3.1 Disaggregation of Switzerland

We upgrade our pan-European model by disaggregating the Swiss production and load and by embedding the Swiss transmission grid, either in the present configuration or in the strategic grid 2025, inside the aggregated European grid, see Fig. 2.7. We describe below the necessary

modifications to our pan-European model.

Swiss transmission grid

For lines inside Switzerland, we use their true admittances provided by Swissgrid. Effective admittances are determined for lines between Swiss buses and the aggregated European buses. They are obtained by the same procedure we applied in Section 2.1.1. Fig. 2.8 illustrates how well this calibration process works. The PS power plants under construction, Nant-de-Drance and Linth-Limmern, are connected to the grid. For the present configuration of the grid, we artificially add a substation to connect Nant-de-Drance power plant to the grid.
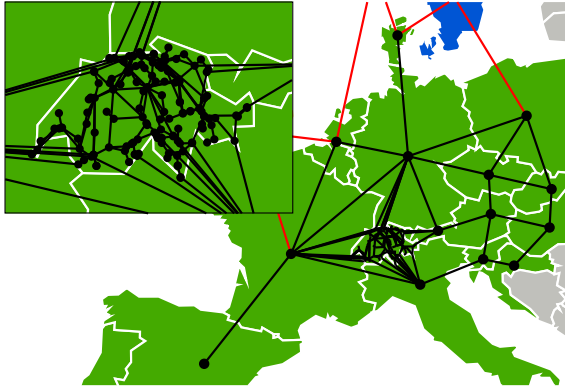

Figure 2.7 – *The Swiss high voltage transmission network is embedded into our aggregated model of the pan-European power grid.*
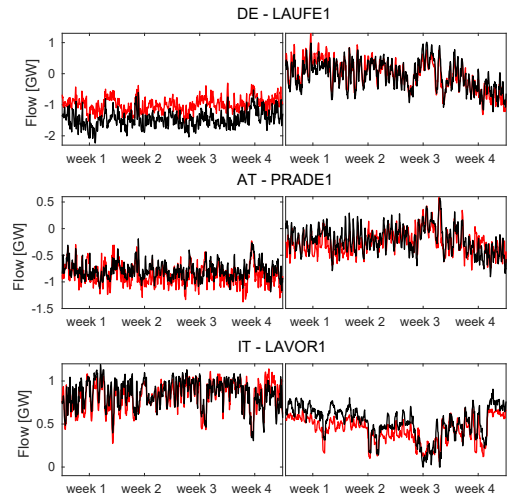

Figure 2.8 – *Calculated (red) vs. historical (black) power flows on three different interconnections to Switzerland for four winter (left panels) and four summer weeks (right panels) in 2015.*

Allocation of dispatchable productions

Our economic dispatch determines the total production per technology for the Swiss dispatch zone, whereas the power flow computations require power injections in the Swiss transmission network at each individual bus, which we obtain as follows. For a given technology #s, the distribution factor π_i^s depends on the installed capacity $P_{\max i}^s$ connected to the Swiss grid bus #i and it is defined as

$$\pi_i^s = P_{\max i}^s / P_{\max \text{CH}}^s, \tag{2.22}$$

where $P_{\max \text{CH}}^s$ is the total installed capacity of this technology in Switzerland. Then, the power injection $P_i^{\text{inj}}(t)$ at the bus #i is given by

$$P_i^{\text{inj}}(t) = \sum_s \pi_i^s P_{\text{CH}}^s(t) - R_i(t). \tag{2.23}$$

Here, $R_i(t)$ is the residual load at bus $\#i$, defined as the difference between the true 2015 load and the new RES productions we obtain as explained below.

Distribution of new RES over the Swiss territory

Our Swiss RES production profiles rely on the wind speed and solar irradiance profiles at several locations in Switzerland, taken from the Federal Office of Meteorology and Climatology database [39].

Most of the projects of new wind turbines in Switzerland are located in the Jura Mountains, therefore we consider new wind turbines only there. The production of a wind turbine is obtained from the wind speed with the following power curve

$$P^{\text{tur}}\big[v(t)\big] = \begin{cases} P_{\text{rated}}\,, \text{if } v_{\text{rated}} \leq v(t) < v_{\text{max}}\,, \\ P_{\text{rated}}\big/v_{\text{rated}}\big[v^3(t) - v_{\text{min}}^3\big]\,, \text{if } v_{\text{min}} \leq v(t) < v_{\text{rated}}\,, \\ 0\,, \text{otherwise.} \end{cases} \tag{2.24}$$

where P_{rated} and v_{rated} are the rated power of the turbine and the corresponding rated speed, v_{min} is the minimal wind speed at which the turbine produces, v_{max} is the cut-out speed above which the turbine is stopped. In the following we use $P_{\text{rated}} = 1[\text{p.u.}]$, $v_{\text{min}} = 3[\text{m/s}]$, $v_{\text{rated}} = 14[\text{m/s}]$ and $v_{\text{max}} = 25[\text{m/s}]$. To obtain the Swiss wind production, we compute the production of 600 wind turbines. We need to take into account the fact that each wind turbine is subjected to different winds. There are only a few weather station in the Jura Mountains that give us wind time series. To each wind turbine we therefore attribute a wind profile that is defined as the sum

$$v_i(t) = v_i^{\text{ws}}(t) + W(i, t), \tag{2.25}$$

of the true wind speed $v_i^{\text{ws}}(t)$ at some weather station and a white noise term $W(i, t) \in [-W_0, W_0]$, with W_0 chosen so that the noise term does not dominate. The total wind production is given by

$$P^{\text{wind}}(t) = \xi^{\text{wind}} \sum_{i=1}^{100} P^{\text{tur}}\big[v_i(t)\big], \tag{2.26}$$

where ξ^{wind} normalizes the total wind production profile in order to obtain the desired annual production. As no information on the topology of the distribution network is available, it is not possible to anticipate exactly where the production of a wind turbine is injected in the transmission network. Consequently, we distribute the wind production to buses in the vicinity of the Jura Mountains with an ad-hoc set of distribution factors.

Solar photovoltaics will be dominantly installed on rooftops in Switzerland. Therefore we distribute the PV production according to the population. One can argue that the urban regions with higher population density (i.e. where people live in larger residential buildings

rather than in individual dwellings), have lower roof surface per capita ratios. However, there are usually commercial or industrial parks in the vicinity of urban regions offering important roof surfaces. For the sake of simplicity, we assume that these two aspects balance each other. The PV production at each bus is the sum of the contributions of all municipalities connected to it via the low- and medium-voltage grids. We assume that each municipality is served by its nearest bus. The contribution of the municipality #k depends on its population and its solar irradiance $\mathrm{SI}_k(t)$ which is obtained as the weighted average of the solar irradiances at the nearest weather stations

$$\mathrm{SI}_k(t) = \sum_{d_{kj} < d_{\max}} \mathrm{SI}_j^{\mathrm{ws}}(t) \big/ (N d_{kj}), \tag{2.27}$$

where $\mathrm{SI}_j^{\mathrm{ws}}(t)$ is the solar irradiance at the weather station #j, d_{kj} is the distance between the municipality #k and the weather station #j, $d_{\max} = 40$km is an arbitrarily chosen threshold distance and $N = \sum_{d_{kj} < d_{\max}} d_{kj}^{-1}$. This procedure prevents local perturbations from affecting too strongly PV production and its injection at buses. The contribution $\mathrm{PV}_k(t)$ of the municipality #k depends on its population pop_k and is given by

$$\mathrm{PV}_k(t) = \mathrm{pop}_k \, \mathrm{SI}_k(t) \big/ \mathrm{pop}_{\mathrm{tot}}, \tag{2.28}$$

where $\mathrm{pop}_{\mathrm{tot}}$ is the Swiss population. Each municipality contributes to the PV production of its closest bus. The PV production at the bus #i is given by

$$P_i^{\mathrm{pv}}(t) = \xi^{\mathrm{pv}} \sum_{k \in \mathcal{K}_i} \mathrm{PV}_i(t), \tag{2.29}$$

where $\mathcal{K}_i$ is the set of indices of the municipality related to the bus #i and ξ^{pv} uniformly scales to the PV profiles meet the planned annual production.

2.3.2 Comparison between the present grid and the strategic grid 2025

The missions of Swissgrid are (i) to allow electricity to be exchanged indiscriminately and (ii) to guarantee the reliability of the grid. In the following, we evaluate if the present configuration of the grid and the strategic grid 2025 allows to fulfill them.

In 2015, Swissgrid presented its strategic grid 2025 [38] which is the result of a two-step optimization. First, the present grid is enhanced progressively until the resulting grid is no longer congested. Secondly, each upgraded element is removed sequentially and the influence of this action on the reliability of the grid is assessed [40]. To assess the strategic grid 2025 against the current one, Swissgrid used 2-step simulations. The first step is a market simulation, the productions are dispatched at national scale. Once the national productions are determined, they are distributed to the buses of a spatially resolved pan-European grid. The second step consists in standard N-1 power flow computations. Swissgrid used two commercial programs: *Powrsym* [41] for the market simulations and presumably *PSS/E* [42]

for the power flow computations. Our approach is different in so far as our model find the economic dispatches and the power flows in a single step. Our modelling of pumped-storage facilities and their operations, with hourly resolution based on an effective electricity price, seems more realistic than the one used by Swissgrid for the elaboration of the strategic grid 2025 [40].

Opportunities for PS hydroelectricity operations

We investigate if electricity producers might suffer from production limitations due to the congestion of the Swiss transmission grid. Here, we focus on PS hydroelectricity, because two large new PS power plants, Nant-de-Drance (900MW) and Linth-Limmern (1000MW), will be soon connected to the grid which will double the Swiss PS hydroelectricity capacity.

In order to investigate whether or not the Swiss PS hydroelectricity is hindered by the congestion of the network, we perform numerical simulations with and without thermal power limits on the Swiss transmission grid. More constraints means that some economically viable operations cannot be made because they would lead to the violation of some thermal limit constraints. By comparing simulations with and without constraints, we can determine if the producers, in particular hydroelectric producers, are limited in their operations by grid constraints and the associated necessary redispatch.

Fig. 2.9 (a) shows the Swiss PS production with the 2015 grid. When the Swiss flows are constrained the usage of the PS facilities is reduced by 18% and PS plants can only rarely produce at full power. The situation significantly improves with the 2025 grid, as can be seen in Fig. 2.9 (b), where flow constraints affect PS production only weakly. Clearly, the strategic grid 2025 is beneficial for PS operators, who will be able to operate their facilities almost without grid constraints.

Swiss network congestion

$N-1$ contingency calculations are a standard procedure used by TSOs to assess the reliability of their transmission system. Each line of the Swiss network is tripped sequentially, and a power flow calculation with the resulting network is performed. We define the worst case $N-1$ flow $F_k^{\text{N-1}}(t)$ for the line #k at time t as

$$F_k^{\text{N-1}}(t) = \max_{i=\{1,\cdots,N_{\text{line}}\}} \left(|F_{i,k}(t)| \right) \forall\, t\,, \tag{2.30}$$

where $F_{i,k}(t)$ is the power flow on the line #k after line #i tripped.

Fig. 2.10 (a) shows the annual maximal $N-1$ power flows in the 2015 grid. We observe that the grid is strongly congested on several lines. This is particularly the case in sections of the grid connected to large hydro power plants. Fig. 2.10 (b) shows that the strategic grid 2025 strongly reduces these congestions. Still, the connection at the far east of the network gets overloaded
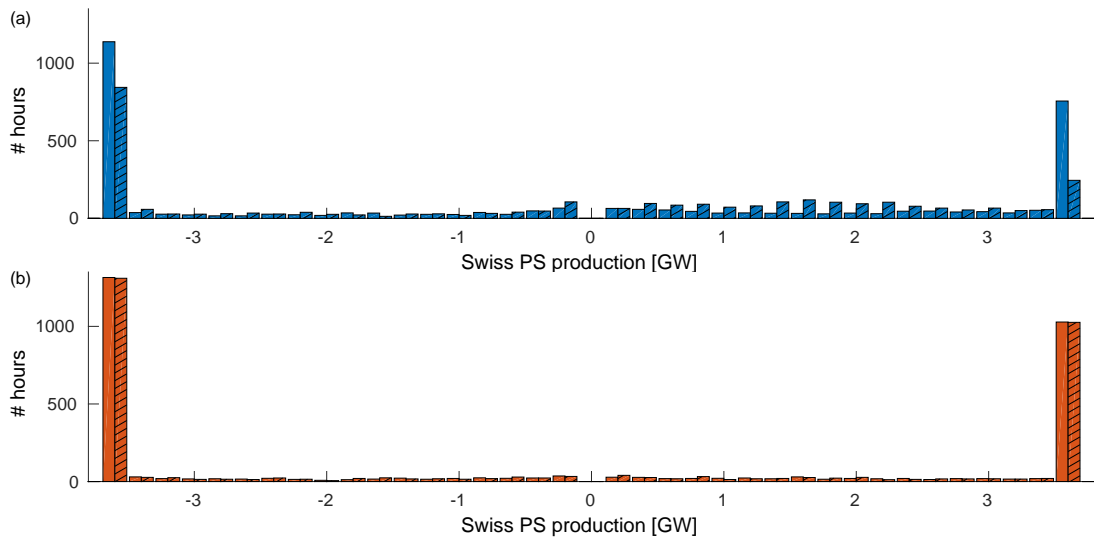
Figure 2.9 – *Histograms of the production of Swiss PS plants with (hatched) and without (plain) constraints on the power in the 2015 grid [panel (a)] and in the strategic grid 2025 [panel (b)]. Negative production means pump consumption and in both panels, the idle state spike has been removed. The annual pump consumption is higher than the annual production due to a finite efficiency of η = 0.9 each way.*

sometime by the North-South transit. The reinforcements proposed by Swissgrid seems to strongly reduce the congestion of the Swiss transmission network.
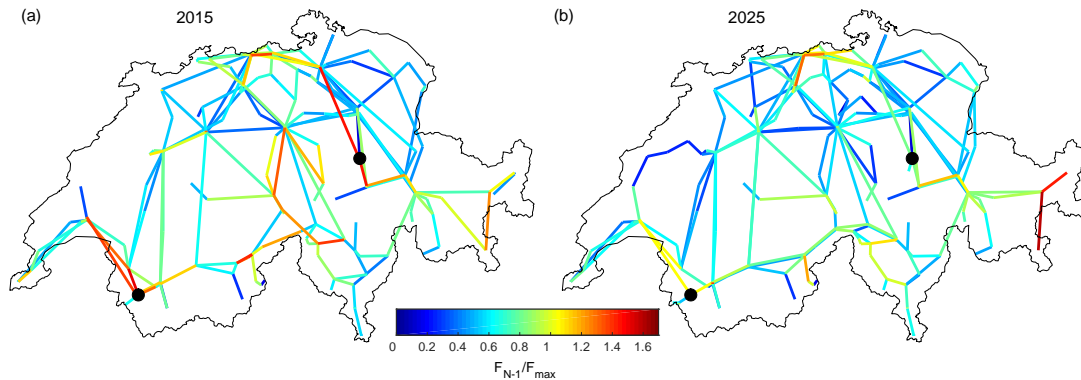

Figure 2.10 – *(a) Annual N-1 maximal flows in the 2015 grid. (b) Annual N-1 maximal flows in the strategic grid 2025. These flows correspond to the 100% PV scenario, similar results are obtained with the RES mix scenario. The two large new PS facilities are displayed with black dots.*

Our investigations show that the Swiss transmission network will be considerably less congested after the enhancement of the grid from its present configuration to the strategic grid 2025. In particular, Swiss hydroelectricity producers will not be affected by limitations due to grid congestion. The strategic grid 2025 allow Swissgrid to fulfill its missions, whereas the existing configuration fails to guarantee their fulfillment. For our final investigations, we exclusively use the strategic grid 2025.

2.3.3 Future power flows in the Swiss network

We conclude our investigation of the future reliability of the Swiss grid by observing how the variations of new RES productions in Europe increase the flows in the Swiss transmission network and how it might congest it.

Fig. 2.11 (a) shows simulated dispatched productions of Switzerland, France, Germany and Italy for ten consecutive days in winter. During the first three days, the RES production in Europe is high, in particular from wind power. Wind turbine generation in Germany is actually sufficient to cover alone the whole German load during the first day shown. During that time, hydroelectricity production in Switzerland is low and almost zero during offpeak periods. RES production in Europe decreases over the next three days. Dispatchable productions start to produce more to compensate this decrease. In the last 4 days shown, RES productions in Europe are low. Hydroelectricity in Switzerland produces near or at its maximal power most of the time. Fig. 2.11 (b)-(e) present snapshots of the maximal N-1 power flows corresponding to times indicated by dashed lines in panel (a). In the situation described in panels (b) and (c), the Swiss production is very low, with essentially only Leibstadt producing. The Swiss load is 8.5 GW higher than the national production, while at the same time, Italy is strongly importing too. Even under these exceptional conditions, we see that the strategic grid 2025 behaves well and very few, very localized congestions occur - mostly the eastmost connection.

Fig. 2.12 (a) shows the production of Switzerland, France, Germany and Italy for ten consecutive days, this time in summer. Italy and Switzerland which have high penetration of PV in their mixes, have large production around midday. Italy uses its PS pumps every day at noon and its PS turbines in the evening. Comparing Figs. 2.11 (e) and 2.12 (b), one observes that the Swiss peak production in summer exceeds by far that of winter, with production peaks at 15GW. Nevertheless the grid is less congested in summer, which we attribute to the geographically homogeneous spreading of the PV production in the grid.

As a final remark, the few reinforcements proposed by Swissgrid seem to be sufficient to guarantee the reliability of the Swiss transmission grid until at least 2030. More results are presented in Ref. [10].

Figure 2.11 – *(a) Production and consumption profiles in Switzerland, France, Germany and Italy for 10 days in winter. Color convention is as in Fig. 2.4. Panels (b)-(e) show the worst N − 1 power flows for the strategic grid 2025, for times indicated by vertical dashed lines in panel (a).*
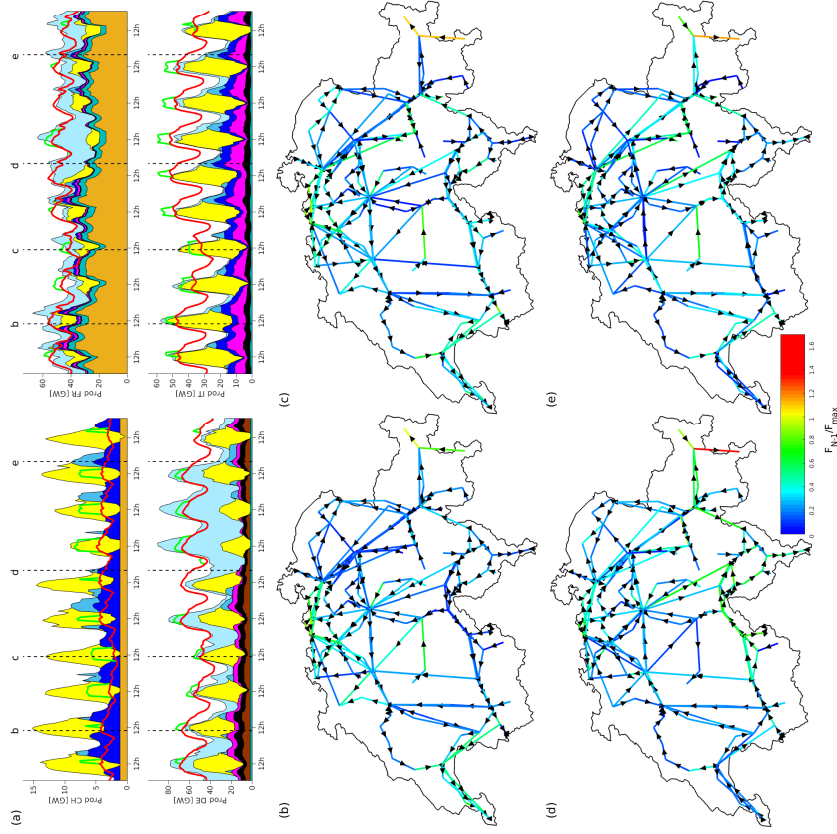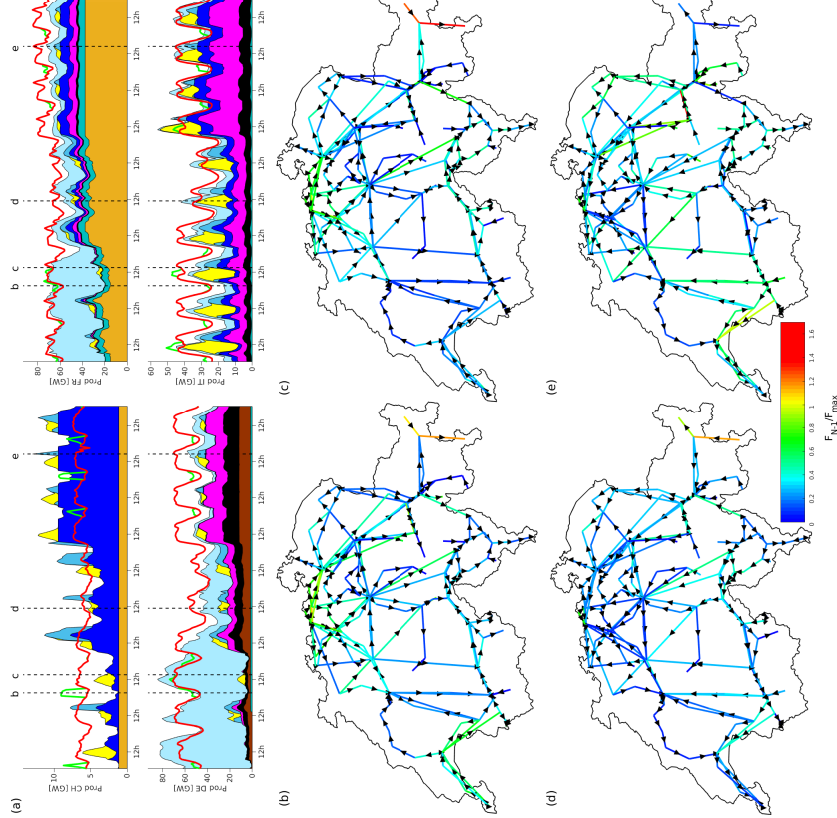
Figure 2.12 – *(a) Production and consumption profiles in Switzerland, France, Germany and Italy for 10 days in summer. Color convention is as in Fig. 2.4. Panels (b)-(e) show the worst N − 1 power flows for the strategic grid 2025, for times indicated by vertical dashed lines in panel (a).*

2.4 Conclusion

We have constructed a pan-European model for the future electricity market. Using a reduction method, we obtained an aggregated model of the pan-European transmission grid. We built an economic dispatch based on the minimization of the generation cost and additional costs related to the curtailment of new RES, pumped-storage operations and power flows. We calibrated it so that it reproduces 2015 production profiles. As a summary, the main features of our model pan-European power dispatch are:

- A remarkable reproduction of historical production profiles.
- Pumped-storage hydroelectricity is dispatched in the most realistic way by maximizing its revenues obtained with an effective price based on the residual load.
- Realistic power flows in the AC grids obtained with power transfer distribution factors (PTDFs), AC and DC connections are treated distinctly.
- An additional quadratic "repulsion" term for each technology to obtain more realistic production profiles.
- An effective TSOs redispatch through an addition cost on power flows.

We investigated how dispatchable sources will be engaged in 2030. We found unsurprisingly that, as the penetration of new RES increases the European mixes, large variations of non-dispatchable productions require more flexibility from conventional dispatchable sources. What is more surprising is that power exchanges and existing PS hydroelectricity are able to absorb the variations of new RES productions, even for a relatively high penetration of new RES in the European energy mix.

We embedded the Swiss network in our aggregated model of the pan-European transmission grid and created RES production profiles for every Swiss bus, based on its location and data from weather stations. We used our model to compare the 2015 grid and the strategic grid 2025 of Switzerland. We showed that the few enhancements proposed by Swissgrid strongly reduce the congestion of the Swiss transmission network. Hydroelectric producers should be able to produce without being restricted in a future with a high penetration of new RES in the Swiss energy mix.

Our investigations suggest that no technical constraint should hinder the energy transition in Europe during the next decade. This is expected to change in further stages of the energy transition, at the horizon of the year 2050, where even more flexibility, more energy storage and/or new RES curtailment will be required. Our results are consistent with those of Ref. [43]. They find that more flexible production is required as the penetration of new RES increases and that flexible sources become essential when the penetration of new RES reaches 50%.

This chapter has illustrated that our pan-European dispatch model *Eurotranselect* is a well-designed, multipurpose, adaptive tool for systematic investigations of future European electricity sectors.

3 Electricity prices: the paradox of the energy transition

In this chapter we investigate the effect of the increasing penetration of new RES on the electricity prices. We start by showing that the residual load, corresponding to the load to which the nonflexible productions are subtracted, is strongly correlated with the day-ahead electricity price. From this observation, we conclude that we can build an effective electricity price based on the residual load. Armed with this physico-economic indicator, we investigate the future revenues of different production technologies. In the early stage of the energy transition, we show that the new RES, in particular the PV productions, reduce the residual load variations and consequently decrease the volatility of electricity prices which affects particularly the revenues of pumped-storage hydroelectricity. The new RES tend to decrease the average price of electricity, especially if thermal baseload productions are not decommissioned. This affects particularly the revenues of the mostly flexible productions. As we demonstrated in Chapter 2, flexible energy sources and energy storage will be required in a later stage of the energy transition for its harmonious unfolding. In this chapter, we focus our investigations on Germany and Spain which have already a large penetration of new RES in their energy mixes. We show that the hydroelectricity becomes profitable again when the penetration of new RES has sufficiently increased. Most of the results presented in this chapter were published in Ref. [44].

3.1 Electricity markets

We briefly explain the energy markets in which electricity is traded, we show that electricity price depends on the load and the new RES productions.

In the 20th century, national European transmission grids were progressively interconnected to increase their reliability which granted the opportunity of international power exchanges. At that time, electricity was mainly produced and traded with long term contracts by national monopolistic companies. The EU acted a directive which initiated the liberalization of electricity markets in 1996. The first power exchange markets in Europe were founded in the following years. On these markets, electricity is mainly traded in day-ahead auction in which electricity

is traded the day prior the delivery. Nowadays a significant share of the electricity consumed in Europe is traded on these markets, see Table 3.1.

Fig. 3.1 illustrates the merit order which is a simplified version of the real auction used in power markets. It consists in the ranking of the available generation capacity in increasing order of generation cost to determine which power plants generate electricity. The low price producers are favored and produce most of the year, while the expensive ones are only engaged in peak load situations. The point where the hourly load crosses the merit order curve gives the hourly electricity price and all the electricity traded for this delivery hour is remunerated at that price. Once installed the new RES produce electricity at no cost, at least at a negligible cost when compared to those of conventional sources. Consequently, when the new RES produce, they correspond to a right shift of the merit order generation capacity curve, which can alternative be represented by a left shift of the load as shown in Fig. 3.1. Therefore when new RES are present in an energy mix, they decrease the average electricity price. Furthermore, the most flexible power plants, which are usually also the most expensive ones, see their capacity factor significantly decrease. The capacity factor is defined as the ratio of the amount of electricity produced to the maximal possible output over a given period of time.
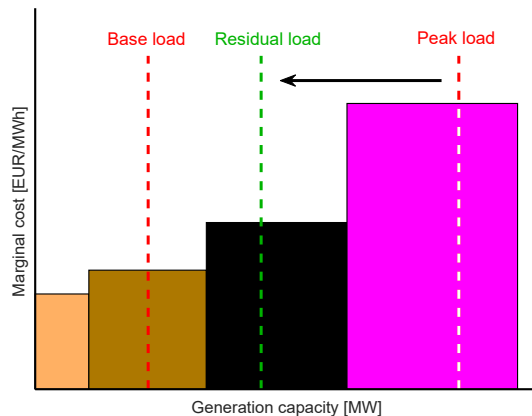

Figure 3.1 – *Illustration of the merit order based on the German energy mix: nuclear (orange), lignite (brown), hard coal (black) and gas (magenta). Each technology has a different generation cost.*

Several articles investigated historical data vs. the penetration of new RES to empirically express electricity prices as a function of green in-feed [45, 46]. The effect of merit order on historical electricity prices under increased penetration of new RES has been investigated by [47], who extrapolated their findings to evaluate future revenues of the new RES. Going further, a number of studies investigated electricity markets where prices are determined by simulated merit orders with marginal costs as inputs [48, 49, 50], which often rely on self-consistent optimizations. As interesting as these works are, they are based on heavy algorithms as well as many assumptions (for instance future fuel prices) to build the merit order.

The starting point of our investigation is the observation that the German residual load and day-ahead electricity price are strongly correlated, see Fig. 3.2. In analyzing other European

countries, we moreover observe that the correlation between residual load and day-ahead prices is generally stronger in countries with higher penetration of new RES. The penetration of new RES is expected to significantly increase in the future, it is natural to expect that this correlation will also increase. Here we define a simple effective electricity price solely based on the residual load in place of the previously mentioned rather complex algorithms.
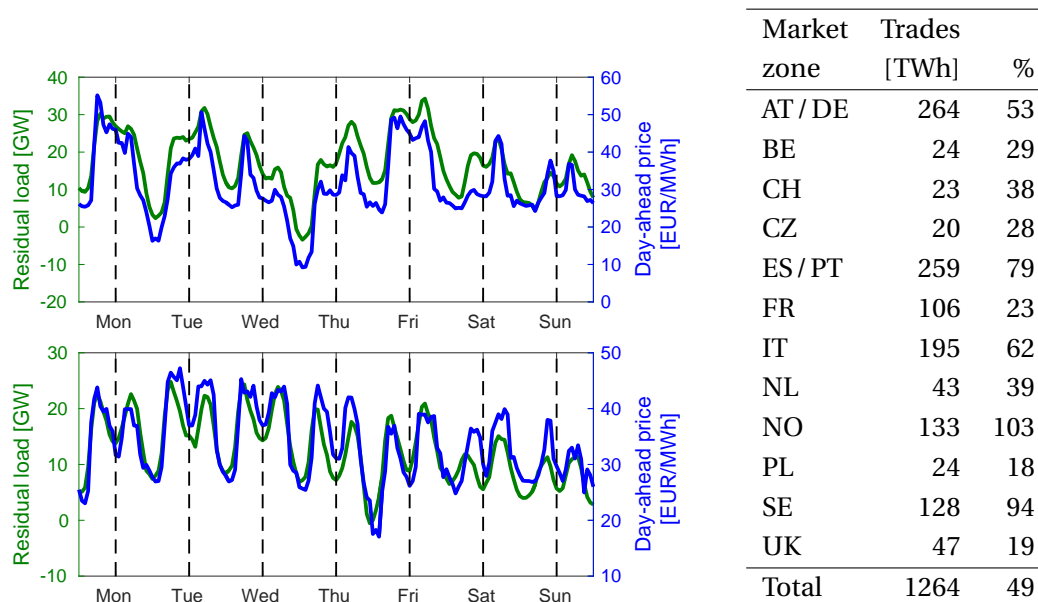

Figure 3.2 – *German residual load (green) and day-ahead electricity price (blue) for a winter (top) and summer (bottom) week in 2015 [data taken from [14]]. Vertical dashed lines indicate noon time.*

Market zone	Trades [TWh]	%
AT / DE	264	53
BE	24	29
CH	23	38
CZ	20	28
ES / PT	259	79
FR	106	23
IT	195	62
NL	43	39
NO	133	103
PL	24	18
SE	128	94
UK	47	19
Total	1264	49

Table 3.1 – *Traded electrical energy and corresponding load percentage of several European day-ahead markets in 2015. Sources: [51], [52], [53] and [54].*

3.2 The residual load and the determination of the must-run

In this section, we refine the notion of residual load that we introduced in Section 2.1.2. In particular, we explain that a share of the dispatchable energy sources acts for economic reason as if it was non-dispatchable. This share is known as the *must-run* [55, 56, 57] and our goal is to assess its current volume in Germany and to find some possible trends of its future evolution.

We remind that the residual load corresponds to the subtraction of the non-dispatchable production to the load. The non-dispatchable productions consist mainly in the new RES. Some power plants keep producing even when electricity prices are below their production costs to avoid ramping costs, this contribution to the residual load is often neglected as it comes from dispatchable energy sources [58]. Nevertheless, it is consistent with the definition and meaning of the residual load to include the must-run productions in non-dispatchable productions and treat them as demand reduction. With this addition, the residual load R_i is

then defined in each zone #i as

$$R_i(t) = L_i(t) - P_i^{\mathrm{pv}}(t) - P_i^{\mathrm{wind}}(t) - P_i^{\mathrm{mrun}}. \tag{3.1}$$

Here, $L_i(t)$ is the national load, and $P_i^{\mathrm{pv}}(t)$, $P_i^{\mathrm{wind}}(t)$ and P_i^{mrun} are PV, wind and must-run productions respectively. In the following, the run-of-the-river (RoR) is incorporated in the must-run. As in Chapter 2, we hourly discretize their profiles, $t_n = n\Delta t$, with $\Delta t = 1$ hour. We assume that, in a given year, P_i^{mrun} does not depend on time. For our initial investigations, we take $L_i(t)$ as the 2015 national load from ENTSO-E database [14] without modification, given the relatively short time span of our investigations (up to 2020). We conclude our investigations by adding a term describing effectively the action of active demand response on the residual load. As in Chapter 2, PV and wind production profiles are obtained from historical 2015 production profiles, taken from ENTSO-E database [14], which we scale up country by country to take into account planned capacity evolution as given in *ENTSO-E 2020 Expected progress* [20].

To obtain $R_i(t)$, we are left with evaluating the must-run power which is not a uniquely defined procedure [56, 55]. In the following, we use two different approaches to determine the must-run in Germany, which lead to comparable volumes of must-run power. Our first approach is to determine the must-run from the historical day-ahead electricity price and share of the different technologies producing. Fig. 3.3 shows the shares of the different technologies composing the German energy mix for each hour of 2017 and the corresponding day-ahead electricity price. From these scatter plots we assess that the must-run corresponds to 75% of the total nuclear capacity, 40% of the total lignite capacity, 45% of the RoR capacity and 5% of the total capacity of gas and hard coal capacities. By summing these contributions, we obtain a must-run in Germany of about 21 GW in 2017. When applied to the year 2015, this assessment gives a must-run of about 23 GW. From the similar scatter plots presented in Ref. [58], we obtain a must-run corresponding to 85% of the total nuclear capacity, 70% of the total capacity of lignite power plants and 10% of the total capacity of hard coal power plant for the period from October 2008 to November 2009. This estimate sums up to about 36 GW. This procedure is tedious as it requires detailed information on the different production and the price of electricity, furthermore it is hard to use it to extrapolate the future trend of the must-run.

In our second approach, we base the determination of the must-run on the evaluation of load duration curves. Fig. 3.4 explains the procedure, where for sake of readability, it is limited to a single week. Fig. 3.4 (a) shows the German load from which we subtract the new RES productions. Fig. 3.4 (b) shows the duration curve of the resulting power profile (green curve) which gives the time during which the profile is over a certain power. By definition, must-run corresponds to the power that exceeds a certain level "most of the time", otherwise it would not be economically viable. The must-run volume we obtain with this procedure depends on what we consider as "most of the time".
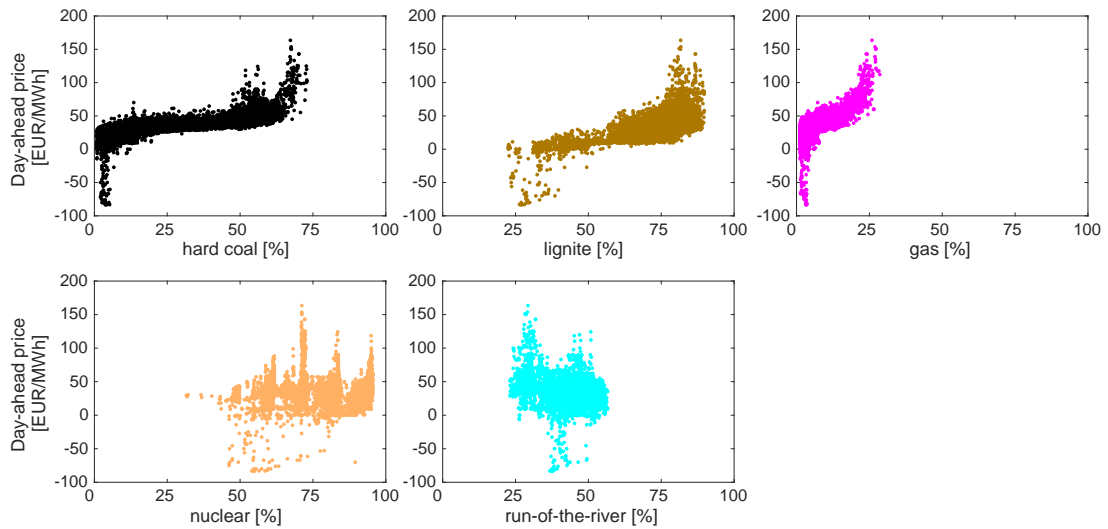
Figure 3.3 – *Engaged proportion of the different technologies in the German energy mix as electricity price evolves, each point corresponds to an hour of 2017.*
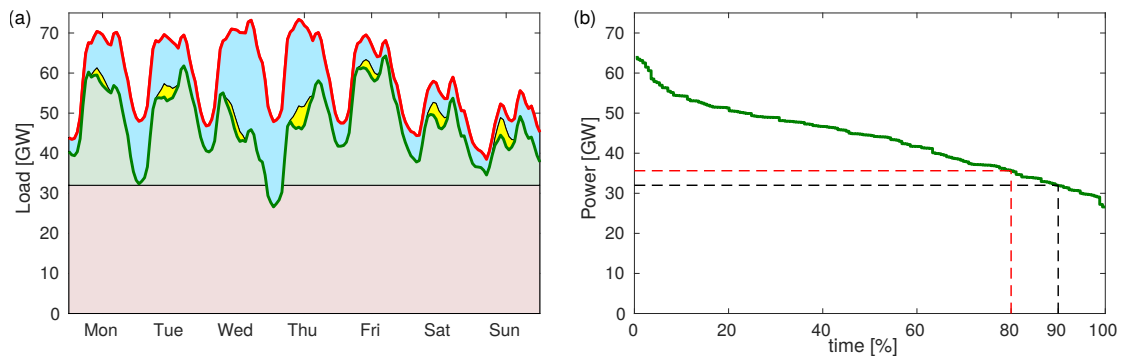

Figure 3.4 – *Assessment of the must-run power by duration curves. (a) Residual load (green area) is obtained by subtracting the new RES productions [wind (cyan) and PV (yellow)] and the must-run (light red band) to the load (red curve). (b) Determination of the must-run form duration curve of load minus new RES productions (green curve).*

By applying this procedure to the load and new RES production yearly profiles corresponding to the years 2000 to 2020, we obtain different duration curves and we can track the evolution of the must-run. Fig. 3.5 (a) shows the residual load duration curves for four different years in Germany. We extract the must-run as the corresponding power threshold exceeded during "most of the year", and chose this to mean 7000 (vertical red dashed line) or 8000 hours (black dashed line). The obtained must-run is plotted in Fig. 3.5 (b) for these two choices (dashed lines). We see that the two curves mostly differ by a vertical shift of 3-4 GW. The must-run is about 30-35 GW in 2010, and keeps decreasing thereafter, as the penetration of new RES increases. Our two approaches to the determination of the must-run are in good agreement. We therefore validate our procedure for estimating the volume of must-run production and use it to compute residual loads based on the scenario *ENTSO-E 2020 Expected progress* [20].
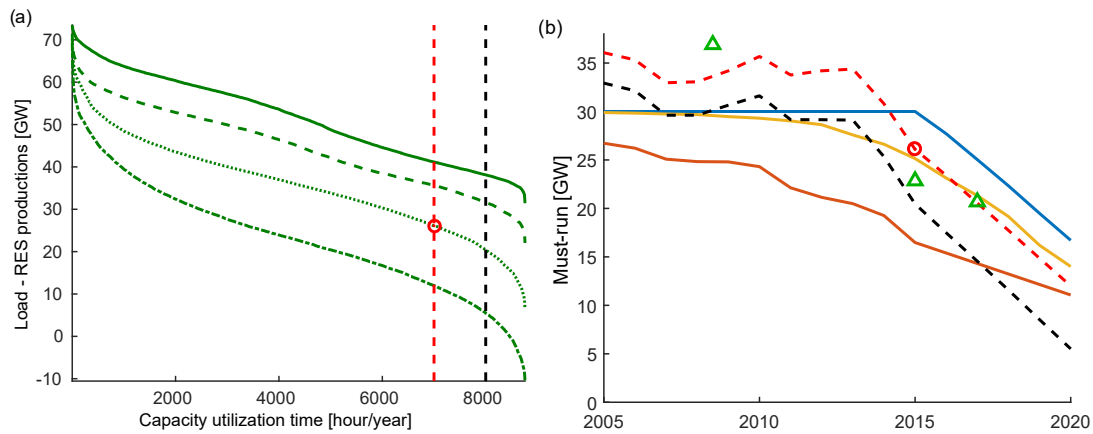
Figure 3.5 – *(a) Duration curves of German load minus RES productions for the years 2000 (solid), 2010 (dashed), 2015 (dotted) and 2020 (dash-dotted). (b) Must run power as obtained from the duration curves [red and black dashed curves, corresponding to the red/black dashed vertical lines in panel (a), the red circles illustrate the connection between panel (a) and panel (b).] and our three scenarios: keeping thermal production capacity "as long as possible" (blue), "exact substitution" (red), "interpolated path" (orange). The green triangles indicate the estimates we obtain from market prices and production profiles.*

It is important to realize that the procedure just described underestimates (overestimates) the must-run for exporting (importing) countries. As a matter of fact, Fig. 3.5 (b) suggests that the German must-run started to decrease already in 2013, instead, German thermal production capacity has been kept constant in 2013–2016 while its exports have increased significantly. This suggests that Germany will keep a large must-run as long as it can export its production when needed. To take this effect into account, we introduce three different scenarios for must-run evolution which we will use in our investigations. These three scenarios are shown in Fig. 3.5 (b). The "*as long as possible*" (blue) scenario corresponds to a must-run that is constant until 2015 after which it decreases with the same rate of 3 [GW/year] in 2016-2020 as the dashed lines. The "*exact substitution*" (red) scenario corresponds to the opposite case where thermal capacities are withdrawn exactly at the same rate as new RES are installed. Finally, the "*interpolated path*" (orange) scenario is a smooth curve interpolating somehow arbitrarily between the blue and red scenarios. None of them will exactly be realized, we use these scenarios to understand the influence of must-run on electricity prices. Finally, while we just focused on the German case to describe the procedure for evaluating must-run capacity, the described method is applied to other European countries, in particular to Spain.

3.3 An effective electricity price based on the residual load

Fig. 3.2 illustrates that a strong correlation exist between national residual loads $R_i(t)$ and day-ahead prices $p_{\mathrm{da}i}(t)$. In this section, we first validate this by quantifying the correlation between national residual loads and day-ahead electricity prices in several European countries. Having validated it, we confidently construct an effective price on the residual load. We use this simple effective price to investigate qualitatively the future electricity prices as the penetration

of new RES increases in the European energy mixes. Finally, we determine the parameters relating the electricity price to the residual load.

The residual load indicates, by definition, the periods of surplus or deficit of production of new RES. It has been the focus of many recent investigations evaluating the needed capacity of energy storage, of thermal storage and of additional dispatchable productions to help absorb large penetrations of new RES [56, 57, 59, 60]. In his analysis of negative price regimes, Nicolosi illustrated a connection between the residual load and the merit order [61]. von Roon and Hubber have been the only ones so far to report a direct correlation between residual load and spot electricity prices [62]. Their investigation of the German electricity market before 2010 further assumed that the coal and natural gas price determine the electricity price most of the time. They proposed to model electricity prices as a function of the natural gas price and of the residual load.

To the best of our knowledge, we are the first to investigate the future revenues of electricity producers obtained with effective electricity prices solely based on the residual load.

3.3.1 Correlation between national electricity prices and residual loads

While some degree of correlation between the residual load and spot market prices is expected, a strong correlation between them has been reported in Ref. [62] for Germany in 2007–2009.

We quantify this correlation for different European countries by measuring their Pearson's correlation coefficient which for two discrete sets of data $X = \{x_k\}$ and $Y = \{y_k\}$ reads

$$r(X, Y) = \frac{\sum_k (x_k - \bar{x})(y_k - \bar{y})}{\sqrt{\sum_k (x_k - \bar{x})^2 \sum_k (y_k - \bar{y})^2}}, \tag{3.2}$$

where $\bar{x}$ and $\bar{y}$ are the average values of the two sets. By definition, one has $r \in [-1, 1]$, with $r = 0$ indicating the absence of correlation between the two sets, $r = 1$ two perfectly correlated sets, $r = -1$ two totally anticorrelated sets and $r > 0.5$ indicates an already strong correlation.

We obtain correlation coefficient $r(p_{\mathrm{da}\,i}, R_i)$, for the years 2012-2015, from hourly sets of data for both residual loads R_i and day-ahead prices $p_{\mathrm{da}\,i}$, from which we removed the 2 % highest and lowest values – corresponding to those that are further away from the average than two or three standard deviations. These extreme events correspond to exceptional situations with forecast errors, unplanned production outages and so forth [63, 64]. These events are hardly predictable and lie beyond the scope of the present work. Table 3.2 shows the evolution of correlations between residual loads and day-ahead prices of the four largest countries in continental Europe. All values are large, $r > 0.58$, and seem to be constant or perhaps even increasing with time.

We further investigate the correlation coefficient for 2015 data in a number of continental European countries. Fig. 3.6 plots the correlation coefficient between national residual load

and day-ahead electricity price as a function of new RES penetration, which we took as the ratio of yearly RES production to the total electricity production. Data are taken from ENTSO-E database [14] and have been crosschecked and completed where necessary with data obtained from national grid operators and power markets.

The correlation coefficients in Table 3.2 and Fig. 3.6 satisfy $r(p_{\mathrm{da}i}, R_i) > 0.58$ in all cases, indicating a strong correlation between the residual loads and day-ahead prices. Additionally, $r(p_{\mathrm{da}i}, R_i)$ is larger in countries with larger penetration of new RES, with the exception of Switzerland, where the correlation is presumably higher due to a large penetration of hydro-electricity. Given this trend, and the planned increase in new RES penetration in all European countries, it seems natural to expect an even larger correlation between residual loads and day-ahead prices in the future.

Figure 3.6 – *Pearson's correlation coefficient r between national residual loads R_i and 2015 national day-ahead prices $p_{\mathrm{da}i}$ as a function of the penetration of new RES in several European countries.*
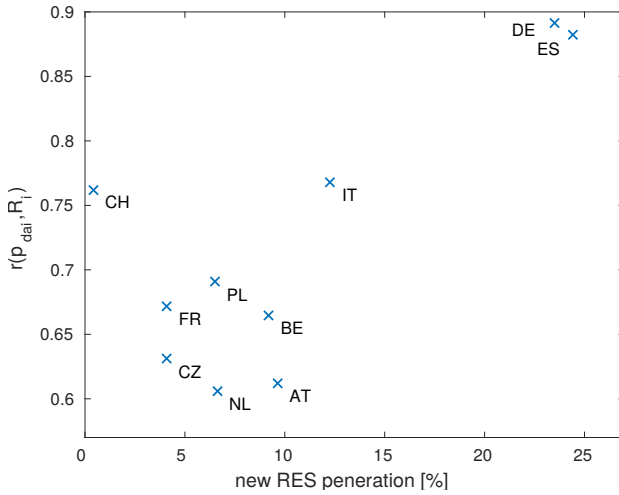
	2012	2013	2014	2015
FR	0.65	0.74	0.71	0.67
DE	0.78	0.86	0.89	0.89
IT	0.63	0.58	0.61	0.77
ES	#	#	0.77	0.88

Table 3.2 – *Evolution of the correlation $r(p_{\mathrm{da}i}, R_i)$ between national day-ahead prices and residual loads.*

3.3.2 Evolution of electricity prices during the energy transition

We validated that there is a strong correlation between residual loads and day-ahead electricity prices and therefore that our assumption $p_{\mathrm{da}i}(t) \propto R_i(t)$ holds. Here, we use this relationship to qualitatively forecast electricity prices and price fluctuations at different stages of the unfolding of the energy transition.

The new RES progressively substitutes thermal productions, doing so they reduce the must-run and change fluctuations in the residual load. The way these fluctuations change depends on the chosen RES mix. PV panels produce more around noon, therefore their production is correlated with the main load peak. Wind productions are more erratic and are therefore relatively uncorrelated with the load at least on short timescales. Consequently, fluctuations in residual loads will always increase if the substitution mix is made of wind power only, while

they will first decrease before increasing again if the mix is dominated by PV. This is illustrated in Fig. 3.7 which sketches the behavior of the residual load at three different stages of the energy transition. Panel (a) shows the situation at the very initial stage of the energy transition, with low RES penetration. The shape of the residual load is very similar to the load itself and the must-run is high. Panel (b) illustrates the transition period with increased RES penetration with a significant fraction of PV, corresponding to the German mix. PV significantly decreases the load peak during office hours, which reduces fluctuations of the residual load. The must-run is still high. In our model, this reduces fluctuations in electricity prices, therefore there are less financial opportunities for flexible productions. In the final stages of the energy transition, the large RES penetration completely changes the shape of the residual load, which looks now very different from the load, see Fig. 3.7 (c). The must-run power is lower, bringing average prices higher. Most importantly, fluctuations in the residual load are comparable to and even higher than those at the early stages of the energy transition.
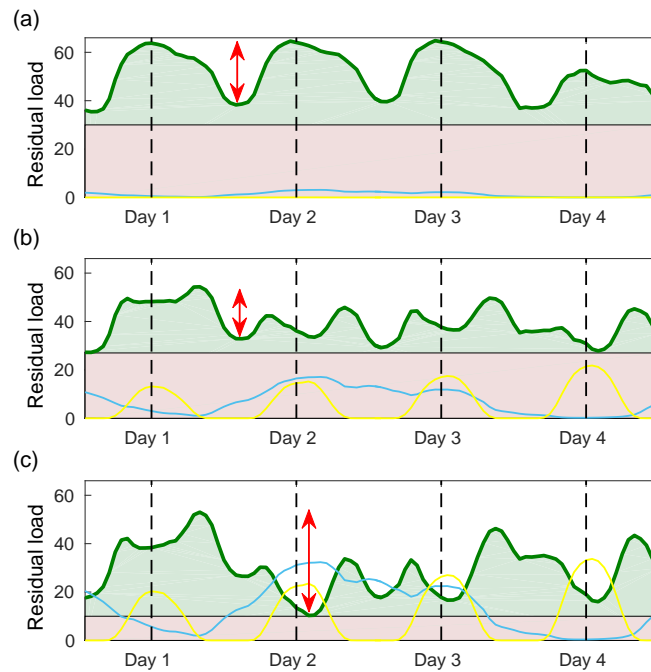
Figure 3.7 – *Sketch of the residual load (green area) and must-run (light red band) at three stages of the energy transition: (a) Initial, (b) intermediate and (c) late stages of the transition. PV (yellow) and WT (light blue) production profiles are superimposed. Red arrows indicate the magnitude of fluctuations of the residual load. Vertical dashed lines indicate noon time.*

3.3.3   Determination of the pricing parameters

We construct an effective electricity price as a linear regression of the residual load,

$$p_{\mathrm{da}}(t) = \Delta p_{\mathrm{da}} R(t) + p_{\mathrm{da}0}\,, \tag{3.3}$$

We focus on electricity prices and revenues for various productions in Spain and Germany, two large European countries that are already well engaged in their energy transition in the electric sector, with large penetration of new RES. As we restrict our investigations to only two countries, we drop the country index $\#i$. The RES mix has proportionally less PV in Spain than in Germany, which allows us to identify differences in the evolution of prices from different choices of RES mixes. Based on 2015 data, we obtain $\Delta p_{da} \approx 1$ and 2.2 [€/MWh·GW^{-1}] and $p_{da0} \approx 20$ and 30 [€/MWh] in Germany and Spain respectively for the parameters in Eq. (3.3). We found very little change in these parameters during the years 2013–2015 in Germany and therefore assume these parameters to be constant in time in each country, for a time window ranging from 2015 to 2020. That this is reasonable is illustrated in Fig. 3.8 which shows that the effective price $p_{da}(t)$ of Eq. (3.3) reproduces historical day-ahead prices quite well. The agreement is already good in 2006 and becomes even better in 2013. Exceptional price spikes are not totally captured, which correspond however to unusual situations beyond the reach of our modeling.

In the following, we investigate future expected revenues of electricity producers on the assumption that Δp_{da} and p_{da0} remain constant. Fig. 3.8 shows that this assumption hold retrospectively over a decade. In the future, if economic conditions vary, it may impact the pricing parameters Δp_{da} and p_{da0} and other scenarios with different values of Δp_{da} and p_{da0} can be investigated. Qualitatively, one anticipates that p_{da0} is determined by the marginal cost of must-run production. In Europe this is essentially the marginal price of electricity from coal-fired plants, and therefore p_{da0} increases if carbon taxes increase. The parameter Δp_{da} on the other hand is more directly related to the order of merit, and thus to the marginal cost of electriciy from gas-fired power plants. As such it will follow the evolution of both carbon taxes and natural gas prices. How much these parameters vary for given variations in gas prices and carbon taxes needs to be calibrated. Performing this calibration is beyond the scope of the present work.

3.4   Future revenues of electricity producers

We investigate the future revenues of different electricity productions in Europe with the effective electricity price defined in Eq. (3.3). We initially focus on the hydroelectric sector, which can provide production flexibility and storage capacities needed to integrate new RES into the electric grid. We next turn our attention to general power plants characterized by their annual number of operation hours and finally we investigate how active demand respond affects our findings. We show that the length of the intermediate period where the revenues for flexible productions and PS hydroelectricity are reduced depends on (i) the rate at which RES penetration increases, (ii) the chosen RES mix, and (iii) the rate at which must-run is reduced.
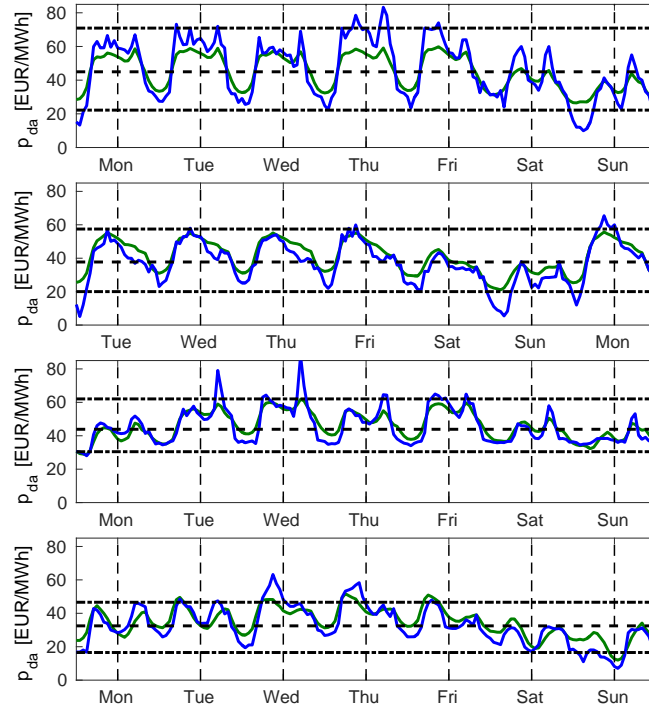
Figure 3.8 – *Effective electricity price defined in Eq.* (3.3) *built on the residual load (green line) and actual day-ahead electricity price (blue line) during a week in winter and summer 2006 (top two panels) and 2013 (bottom two panels) in Germany. Dashed lines show the monthly average price and the dotted-dashed lines prices exceeded 10 and 90 % of the time during that month. Vertical dashed lines indicate noon time.*

3.4.1 The profitability of hydroelectricity

We focus on the revenues of hydroelectric power plants. As we mentioned earlier, Swiss hydroelectricity is suffering from the low electricity prices. Due to the strong interconnection between the German and Swiss transmission grids, electricity prices in Switzerland are particularly affected by the German new RES production peaks. Consequently, it is reasonable to investigate the future revenues of the Swiss hydroelectricity with the effective electricity price based on the German residual load.

Pumped-storage facilities

To show how insightful our simple effective description of electricity prices can be, we start by an analytical investigation of the future revenues of PS hydroelectricity, then we corroborate our findings with numerical simulations.

The revenue G of a PS plant over a time interval $t \in [t_i, t_f]$ is given by

$$G = \int_{t_i}^{t_f} p_{\mathrm{da}}(t) \cdot P^{\mathrm{ps}}(t) \mathrm{d}t, \tag{3.4}$$

where $P^{\mathrm{ps}}(t)$ account for the power produced by the PS power plant as well as the power consumed to pump. Optimizing the revenues of PS plants means producing when $p_{\mathrm{da}}(t)$ is large and consuming when $p_{\mathrm{da}}(t)$ is low. It therefore makes sense to assume that P^{ps} and p_{da} are strongly correlated. This assumption is confirmed in Fig. 3.9, which shows the production of a Swiss PS plant and the day-ahead price for 10 consecutive days in 2015. Neglecting losses for the time being, we write

$$P^{\mathrm{ps}}(t) \cong \pi^{\mathrm{ps}} \cdot \left[p_{\mathrm{da}}(t) - \bar{p}_{\mathrm{da}} \right], \tag{3.5}$$

where $\bar{p}_{\mathrm{da}}$ is the average price over the considered time period and π^{ps} is a prefactor linking prices to production. Eq. (3.5) guarantees that $\int_{t_i}^{t_f} P^{\mathrm{ps}}(t)\mathrm{d}t = 0$ as should be for a PS plant without loss. Inserting Eq. (3.5) into (3.4) and using Eq. (3.3), we get

$$G \cong \pi^{\mathrm{ps}} \Delta p_{\mathrm{da}}^2 \, T \mathrm{Var}\left[R\right], \tag{3.6}$$

for the annual revenue with $T = 8760$ hours. This result shows that the revenue of a lossless PS power plant is proportional to the variance of the residual load. With the consideration we made in Section 3.3.2, and under the assumptions described above, it is easy to qualitatively predict the future revenues of a PS power plant. When the new RES mix is dominated by the PV productions, they first decrease in the initial stages of the energy transition, where increased RES penetration reduces price fluctuations. The revenues however increase later, once the RES penetration is such that it restores large fluctuations in residual loads and thus in electricity prices. When the new RES mix is dominated by the wind productions, the revenue always increases.

We next investigate numerically the revenues of PS power plants in Germany and Spain in the period 2005-2020. Residual loads are calculated from 2015 data for the load and RES profiles, the latter being scaled up from year to year to interpolate linearly between the 2015 realized annual production and the planned 2020 annual production [65]. The evolution of the annual RES productions is given in Fig. 3.10 (c) and (d). As in Chapter 2, the revenues of a PS power plant depend on its pumping and producing operations $P_{\mathrm{t}}^{\mathrm{ps}}(t_n)$ and $P_{\mathrm{p}}^{\mathrm{ps}}(t_n)$, they are given by

$$G^{\mathrm{ps}} = \sum_n p_{\mathrm{da}}(t_n) \left[P_{\mathrm{t}}^{\mathrm{ps}}(t_n) - P_{\mathrm{p}}^{\mathrm{ps}}(t_n) \right] \Delta t. \tag{3.7}$$

We generate PS power profiles by maximizing the revenue G of Eq. (3.7). Using the actual day-ahead price, this procedure generates a fictitious PS production profile given by the dotted black curve in Fig. 3.9, which is very close to the actual one (solid black curve). We attribute the few discrepancies to the fact that our maximization of G in Eq. (3.7) is made with perfect advance knowledge of the load and RES productions. This test substantiates our procedure for calculating power profiles and evaluating revenues of PS plants.

Now that we validated that we obtain realistic PS operation with our maximization, we calculate revenues of PS plants from Eqs. (3.7) with the effective price of Eq. (3.3). Revenues of
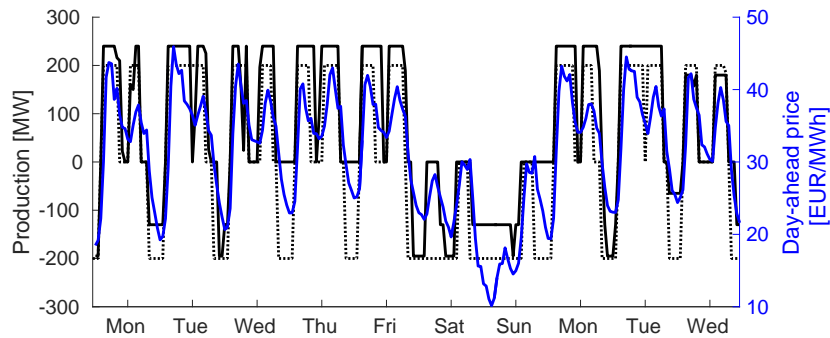
Figure 3.9 – *The actual (solid black curve) and computed (dotted black curve) production of a typical Swiss PS plant and the day-ahead price (blue curve). Negative production means pump load. Sources: Swissgrid and [14].*

German and Spanish PS plants as the energy transition unfolds are shown in Fig. 3.10. One observes that they remain approximately constant in both countries from 2005 to 2008/2009, even though the wind production increases by 40 % in Germany and almost 50 % in Spain. Revenues decrease significantly in Germany from 2009 on, reaching a minimum around 2013 with revenues reduced by as much as 20 %. The revenues decrease more when the must-run reduction is faster [see Fig. 3.10 (a)]. This is easily understandable when one realizes that a higher must-run reduces the residual load, and with it, the electricity price. Power losses due to the finite efficiency of the plant, $\eta < 1$, cost less at higher must-run, which increases revenues.
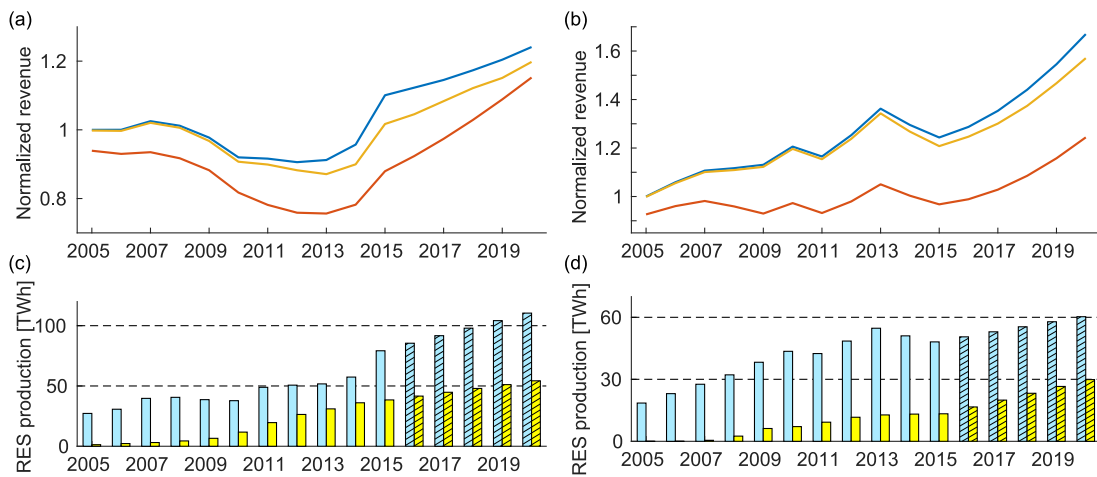
Figure 3.10 – *(a)-(b) Normalized revenue (divided by the revenue of 2005 in the scenario "as long as possible") of a PS power plant in Germany [panel (a)] and in Spain [panel (b)], with $\eta = 0.9$, for the three must-run scenarios presented in Fig. 3.5 (b). (c)-(d) Evolution of wind (light blue) and PV (yellow) annual production in Germany [panel (c)] and in Spain [panel (d)]. Dashed rectangles correspond to planned future evolution [65].*

The striking feature in Fig. 3.10 (a) is that, as expected from the discussion in Section 3.3.2 together with Eq. (3.6), the drop in revenues corresponds to the acceleration of the penetration of PV, which reduces the mid-day residual load peak. The fluctuations of the residual load go

down, leading to reduced revenues through Eq. (3.6). As the penetration of PV further increases, so do the fluctuations of the residual load – one enters the stage depicted in Fig. 3.7 (c) and the revenues increase again. The drop in revenues does not last long. The importance of PV in this phenomenon becomes clear when comparing Fig. 3.10 (a) and Fig. 3.10 (b). The revenues of the Spanish PS power plant displays no significant drop. This is so, because the mix of new RES is clearly dominated by wind power in Spain. Fluctuations in residual load are increased at all stages of the transition, regardless of the chosen scenario for must-run reduction. Thus, from Eq. (3.6), revenues also always tend to increase.

Conventional dam power plants

With the same notations we introduced in Chapter 2, the filling $S^{\text{dam}}(t)$ of a conventional dam storage evolves and is subject to the constraints we presented in Section 2.1.2. A conventional dam hydroelectric plant is characterized by its rated power $P_{\max}^{\text{dam}}$, its storage capacity $S_{\max}^{\text{dam}}$ and the annual electricity generation $\sigma_{\text{dam}} = \sum_n P^{\text{dam}}(t_n)\Delta t$. Relative revenue evolution therefore depends on only two dimensionless parameters which we take as $S_{\max}^{\text{dam}}/(P_{\max}^{\text{dam}}\Delta t) \equiv N_{\text{empty}}$ and $\sigma_{\text{dam}}/(P_{\max}^{\text{dam}}\Delta t) \equiv N_{\text{op}}$, giving the number of hours of operation at full power to empty the reservoir and to use all the annual energy inflow respectively. Their revenue is given by

$$G = \sum_n p_{\text{da}}(t_n)\, P^{\text{dam}}(t_n). \tag{3.8}$$

We find that revenues depend only very weakly on N_{empty}, and therefore focus on the evolution of revenues vs. N_{op}. In multiannual average, dams produce their annual energy inflow σ_{dam}. In continental Europe, this usually corresponds to $N_{\text{op}} \in [1000, 3000]$ hours of full power operation [66].

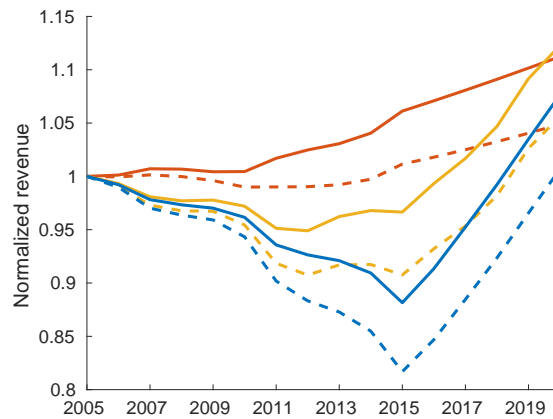Figure 3.11 – *Normalized revenue of conventional dam hydroelectric plants with high (N_{op} = 1000 hours; solid lines) and low (N_{op} = 3000 hours; dashed lines) power capacity in the Alps, with N_{empty} = 1000 hours and for the three must-run scenarios presented in Fig. 3.5 (b).*

Fig. 3.11 shows the revenues of conventional dam hydroelectric plants with N_{empty} = 1000

and $N_{op} = 1000$ and 3000. One sees a similar non-monotonous behavior as for PS plants in Germany. How much and until when the revenue drops depends strongly on the chosen scenario for must-run withdrawal. Generally, we find that revenues drop more and longer for delayed must-run withdrawal – the flexibility of conventional dam hydroelectric power plants is best rewarded for exact substitution of production capacity, where production from thermal plants is reduced at the same rate as new RES production increases. Only in that case we would see no drop in revenue for conventional hydro power plants. Regardless of the must-run scenario, revenues return to their pre-energy transition level by 2020 in all considered scenarios. We observe that plants with higher rated power P_{max}^{dam}, i.e. lower number N_{op} of annual operation hours, see their revenue decrease less than those with lower power, because the higher the rated power, the easier it is to produce almost only when the price spikes.

3.4.2 The influence of the annual operation time on revenues

To better understand the trends discussed above, we finally investigate different types of productions characterized only by the number of hours N_{op} per year they operate at maximal power P_{max} with no further constraint. Accordingly, we consider four classes of power plants which are

  (i) super-peaking power plants, functioning $N_{op} = 1000$ hours per year at peak power P_{max},
 (ii) peaking power plants $N_{op} = 2000$,
(iii) load-following power plants with $N_{op} = 5000$,
(iv) base-load power plants with $N_{op} = 8000$.

Their revenue is simply given by

$$G = \sum_n p_{da}(t_n)P(t_n), \tag{3.9}$$

where we impose no other restriction, than $\sum_n P(t_n) = P_{max} N_{op}$. Fig. 3.12 shows the evolution of these revenues as the energy transition unfolds in Germany, for our three scenarios for must-run reduction. We see first, that regardless of must-run reduction, peaking power plants always have higher revenues and second, that faster must-run withdrawal leads to smaller reductions in revenues. In particular, there is no significant decrease in revenue in the exact substitution scenario, in which thermal plants are retired in direct proportion to the penetration increase of new RES.

These results indicate that the currently very low electricity prices in Europe (and the poor revenues of the hydroelectricity sector) are due to an overcapacity of electricity production more than anything else. Thermal plants are currently retired too slowly compared to the rate at which the penetration of new RES increases. We therefore conjecture that the paradox of the energy transition can be overcome by phasing out thermal plants faster.
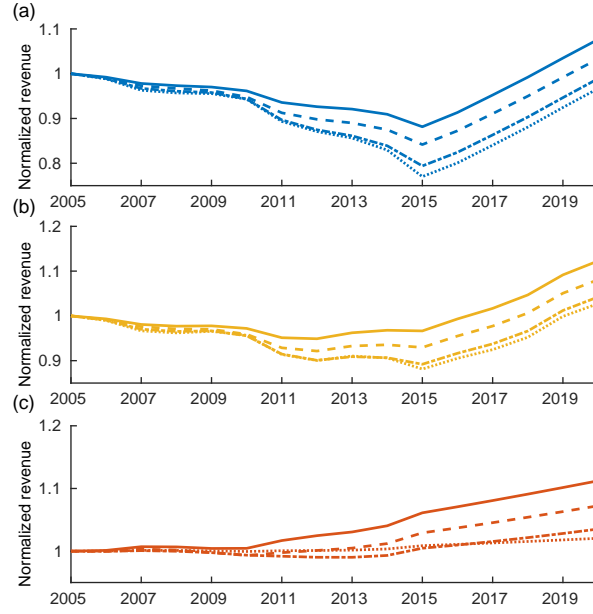
Figure 3.12 – *Normalized revenues of super-peaking plants (solid lines), peaking plants (dashed lines), load-following plants (dotted-dashed lines) and base-load plants (dotted lines) under the three must-run scenarios presented in Fig. 3.5 (b).*

3.4.3 The competition of active demand response

Another approach to mitigate undesirable effects of the new RES is to tackle them locally, at distribution grid level. This approach relies in particular on active demand response (ADR) [67]. We want to assess the maximal effect that ADR can have on the results we presented in the chapter. How ADR is concretely implemented is out of the scope of the present work, we simply add an effective contribution to the national residual load that models the sum of all active demand response contributions. With ADR, the residual load is given by

$$R(t) = L(t) + \delta L(t) - P^{\text{pv}}(t) - P^{\text{wind}}(t) - P^{\text{mrun}} = R_0(t) + \delta L(t), \tag{3.10}$$

where changes in the load profile due to ADR are included in $\delta L(t)$ and R_0 is the residual load without ADR, as in Eq. (3.1). ADR can be deployed for various reasons, for instance to reduce electricity costs of end users or to mitigate load fluctuations on the distribution network. In both instances, ADR tends to reduce variations in the residual load, and we incorporate this goal in an optimizing procedure which we briefly describe. For the sake of simplicity, we do not incorporate specific load constraints such as comfort temperature intervals for ADR with thermostatically controlled loads. The only constraint on the ADR profile is

$$\left|\delta L(t)\right| < \delta L_{\max}, \forall t, \tag{3.11}$$

where $\delta L^{\max}$ is the maximal ADR power. We further assume that the annual consumption remains unchanged,

$$\int_{t_i}^{t_f} \delta L(t) \mathrm{d}t = 0. \tag{3.12}$$

Recent estimates of the potential of ADR indicate that only a fraction of the total consumption can be shifted,

$$\int_{t_i}^{t_f} \left| \delta L(t) \right| \mathrm{d}t \le 2\sigma \int_{t_i}^{t_f} L(t) \mathrm{d}t, \tag{3.13}$$

with $\sigma \simeq 0.01$ giving the maximal fraction of the total consumption that can been shifted, while the maximal ADR power $\delta L^{\max}$ is about 10 % of the maximal load $L^{\max}$ (roughly corresponding to 7 GW in Germany) [67]. These numbers may seem rather small, however they have been obtained assuming a broad load participation in ADR [67].

Our procedure is to compute the ADR profile that minimizes the fluctuations of the residual load,

$$\min_{\delta L} \left[\mathrm{Var}(R) \right] = \min_{\delta L} \left[\mathrm{Var}(L^+ - L^- + R_0) \right], \tag{3.14}$$

where we defined $L^\pm(t) = \max \left[0, \pm \delta L(t) \right]$. We linearly increase σ and $\delta L^{\max}/L^{\max}$ from 0 in 2015 to $\sigma = 0.01$ and $\delta L^{\max}/L^{\max} = 0.1$ in 2025. Because we neglect specific load constraints on ADR, our results likely overestimate the impact of ADR on the residual load, and therefore on electricity prices.

Fig. 3.13 (a) shows the effect of ADR on the revenues of a PS plant. ADR being a form of storage, it competes with PS and reduces its revenues, however, the effect is rather moderate, with 2020 revenues still exceeding those of 2005. Fig. 3.13 (b) shows the revenues of a conventional dam hydroelectric plant, which are even less affected by ADR than those of the PS plant.

3.5 Conclusion

Our interest in this Chapter was to investigate how the increasing penetration of new RES affect electricity prices in Europe. We showed that day-ahead electricity price is strongly correlated with residual loads in most European countries. From this observation we built an effective price based solely on the residual load. With this physico-economic indicator we investigated the revenues of different electricity producers.

As a summary, we found that:

- Residual load and day-ahead electricity prices are strongly correlated in Europe.
- A simple physico-economic indicator can be used to investigate the future electricity prices.
- New RES drag electricity prices down, PV particularly decreases the volatility of electricity prices.
- The insufficient withdrawal of must-run productions plunges the revenues of flexible sources.

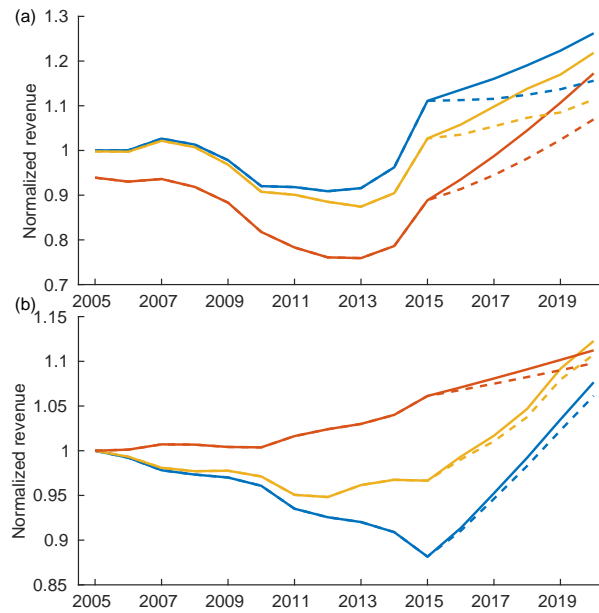Figure 3.13 – *(a) Revenues of a PS plant in Germany with (dashed) and without (plain) ADR. (b) Revenues of a conventional dam hydroelectric plant in Germany with (dashed) and without (plain) ADR. ADR linearly evolves from zero in 2015 to its maximal potential in 2025, with $\delta L^{\max} = 7$ [GW] and $\sigma = 0.01$ [67].*

The roles of inertia, primary control and grid geometry on disturbances in transmission grids

Part II

4 Disturbance propagation in large transmission grids

The rotational inertia of conventional generators helps the system to be resilient against contingencies. The substitution of thermal generators by inertialess new RES may jeopardize power system stability in particular within the first few seconds after the occurrence of a fault. In this chapter, we investigate the propagation of disturbances in large transmission grids following abrupt power losses. To that purpose, we construct a dynamical model of the Continental European transmission grid, its elaboration is detailed in Section 4.1. We investigate the system disturbance following abrupt power losses in Section 4.2. We show that for a given amount of lost power the magnitude of the following disturbance strongly depends on the fault location. Furthermore we show that the strongest disturbance magnitudes are related to the buses located in the "Fiedler areas" which consist in the buses with large squared Fiedler components. The Fiedler vector is the eigenvector corresponding to the smallest non-zero eigenvalue of the network Laplacian. In Section 4.3, we investigate the influence of the placement of inertia by removing the inertia of certain generators. We show that the resilience of the grid against contingencies strongly depends on where inertia was removed. The system is more prompt to be disturbed when inertia is reduced in the "Fiedler areas". To confirm our conclusions, we alternatively use a model of the Texas ERCOT transmission grid [68], where we obtain inertia and damping coefficients using the same procedure as for the European model. The model and most of the results presented in this chapter were published in Ref. [69].

4.1 A dynamical model of the continental European transmission grid

For our investigation on disturbances in large transmission grids, we need detailed information on them. In this section, we elaborate our dynamical model of the continental European transmission grid[1].

---

[1] We built our grid model from different publicly available databases under Creative Commons licenses.

There are only few publicly available models of part or all of the synchronous grid of continental Europe. To the best of our knowledge, the first one was released by Zhou and Bialek [70] and later upgraded to incorporate the Balkans [71]. Other models include ELMOD [72], PEGASE [35, 34] and PyPSA-Eur [37]. These models are intended for power flow computations and they have not been extended to dynamical simulations. Furthermore, except PyPSA-Eur, they lack bus geolocalization which makes the interpretation of the results tedious. None of those model can be used straightforwardly for dynamical investigations, this motivated us to develop our own model.

Similar elaboration procedures to the one presented in this work were used in Refs. [70, 72, 73]. A similar model has recently been constructed, whose parameters do not seem to be publicly available [73].

4.1.1 Construction of the initial load flow solution

The first step of our model elaboration is to obtain the steady state solution that will later be disturbed, it is obtained as follows. The geographical location and the electrical parameters of each bus including voltage level, generator type and rated power are determined from publicly available databases. Line capacities are extracted from their length. Different load situations are investigated using a demographically-based distribution of national loads, together with a dispatch based on a DC optimal power flow.

Wiegmans has extracted geolocalization data for the continental European grid from the ENTSO-E interactive map [74]. Our starting point is his database, which contains location and voltage of buses, identified as either generator or load buses, lengths and voltages for transmission lines and voltages for transformers. We determined the principal component of that grid and discarded non-connected buses. The final network we obtain has 3809 buses connected by 4944 transmission lines.

Electrical parameters of transmission lines

Fig. 4.1 shows the transmission grid in Continental Europe which consists in transmission lines operated at two different rated voltages, 220 kV and 380 kV, and the transformers. In the following, electricity production is dispatched with an optimal power flow in DC approximation, in which the lines have purely imaginary admittances. In Section 1.3, we showed that the series admittance of a transmission line is approximately inversely proportional to its length. Hence, the admittance of the line #k is given by

$$b_k = 1/\left(x^{\text{km}} L_k\right), \tag{4.1}$$

where L_k is its length, x^{km} is the kilometric reactance corresponding to this type of line, we use $x^{\text{km}} = 360\,\text{m}\Omega/\text{km}$ for 220 kV lines and $x^{\text{km}} = 265\,\text{m}\Omega/\text{km}$ for 380 kV lines. These values correspond to averages of those found in Ref. [75]. We compare the admittances obtained

with this procedure with known exact values for a number of lines and find them to be in good agreement.

Disaggregation of national loads

The procedure we use to distribute the national loads to the transmission grid buses is similar to the one we used in Chapter 2 to distribute the PV production to buses in the Swiss transmission network. The national load profiles of European countries are available on the ENTSO-E database [14]. For each country, we distribute those loads demographically over the national buses, similar procedures were used in Refs [70, 72]. Geographical population distributions are first determined from the GeoNames database [76]. Second, the population of each town is distributed over all buses that are less than $d_{max} = 50$ km away from it proportionally to their weight $w = 1$ for 220 kV buses and $w = 3$ for 380 kV buses. The goals of this weighted distribution are twofold: to effectively model the underlying distribution grid and to prevent that excessive loads are assigned to buses in the vicinity of large cities leading to infeasible power load equations. This weighted distribution determines the effective population attributed to each bus. Then, the national load is distributed to each national bus in proportion to their attributed population. The validity of the procedure is at least partly confirmed by the strong correlation between population and load distributions in Italy reported in Ref. [70].
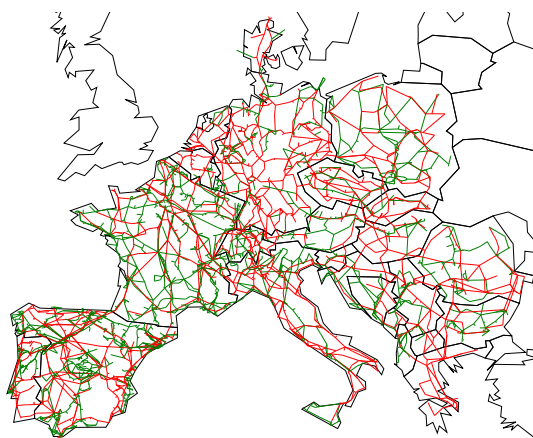
Figure 4.1 – *Continental European grid, 380kV and 220kV lines are displayed in red and green.*
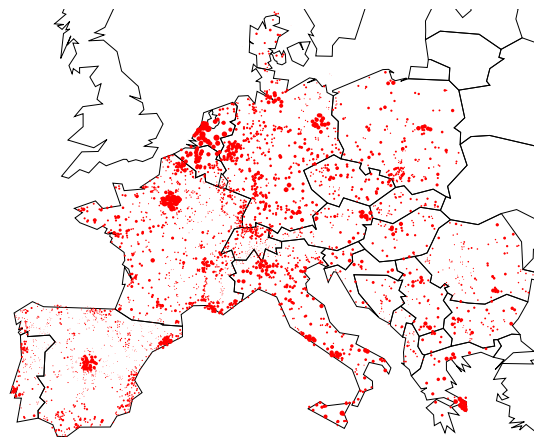
Figure 4.2 – *Load on each bus in continental Europe. The disk areas are proportional to the load. National loads are disaggregated on the national buses according to population distributions.*

Economic dispatch of conventional generators

The last step to obtain our initial state is to determine how much electric power each generator produces. Wiegmans' extract of ENTSO-E interactive map contains partial information on generator types and rated power [74]. The missing generator data are obtained from the global energy observatory website [77]. Fig. 4.3 compares the national conventional generation

capacities for several European countries listed on ENTSO-E database [14] with those we obtained by summing the rated power of the generators in our model, we observe that there is a good agreement between the actual national generation fleets and those in our model. For a given distributed load and with the thermal limit constraints on the transmission lines, the economic dispatch of power generation is obtained thanks to a DC optimal power flow. For each technology #s, we use a different marginal cost c_s, see Table 4.1. For this work, we build two opposed initial steady state cases: a winter evening hour with an high consumption and a large generating fleet and a summer evening hour with a low consumption and a small generating fleet.
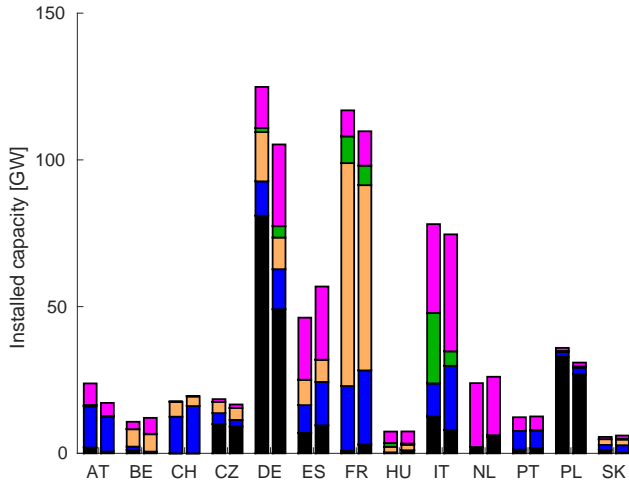
	$c_s \left[\text{MWh}^{-1}\right]$
hydro	80
nuclear	20
lignite	20
hard coal	35
gas	100
other	10

Table 4.1 – *Marginal costs for different technologies of conventional generators, they are loosely based on the values found in Ref. [27].*

Figure 4.3 – *Installed capacity according to our grid model (left column) and to Ref. [14] (right column) for several European countries.*

4.1.2 Addition of power system dynamics

In the previous paragraphs, we obtained the solution of an optimal power flow which is the initial steady state that we disturb with an abrupt power loss. Here, we briefly describe the equations that govern the power system dynamics.

Synchronous generators

In Section 1.3, we showed that the power flow equations in lossless approximation and only taking into account active power flows read

$$P_i^{\text{e}} = \sum_{j \in \mathcal{V}} b_{ij} V_i V_j \sin\left(\theta_i - \theta_j\right), \tag{4.2}$$

where we label $\mathcal{V}$ is the set buses in the system and P_i^{e} the electric power injected in the grid at the generator #i to differentiate it from the mechanical power P_i^{m} transmitted to the turbine. Here, b_{ij} gives the imaginary part of the admittance of the power line connecting bus #i at

voltage V_i to bus #j at voltage V_j and $\mathcal{V}$ is the set of the N buses in the system. Voltages are assumed constant, $V_i = V_i^{(0)}$ and are equal to either 220 or 380 kV.

The kinetic energy of a generator depends on its moment of inertia J_i and its angular speed ω_i, it is given by

$$E_{\text{kin}} = \frac{1}{2} J_i \omega_i^2. \tag{4.3}$$

Conventional generators are designed to operate in a narrow range of frequencies around the nominal system frequency $f_0 = 50$ Hz, typically between 47.5 and 51.5 Hz in Europe. On the assumption that ω_i remains close to its nominal value $\omega_0 = 2\pi f_0$, then its kinetic energy varies as

$$\frac{dE_{\text{kin}\,i}}{dt} \approx \omega_0 J_i \dot{\omega} = P^{\text{m}} - P^{\text{e}}, \tag{4.4}$$

By defining H as the time during which the rated power S of the generator provides a work equivalent to its kinetic energy, we get

$$H_i = \frac{E_{\text{kin}\,i}}{P_{\max\,i}} \approx \frac{J_i \omega_0^2}{2P_{\max\,i}}. \tag{4.5}$$

For a given technology #s, H_s is more or less independent of the size of the generator and is known as the inertia constant. Table 4.2 summarizes the values of inertia constants we use in our grid model. From Eqs. (4.3) and (5.38), The inertia coefficient m_i of the generator depends on its nominal power $P_{\max\,i}$ and its inertia constant $H_{s(i)}$ and is given by

$$m_i = 2H_{s(i)} P_{\max\,i} / \omega_0. \tag{4.6}$$

Fig. 4.4 shows the inertia distribution over the continental European grid. We observe that the vast majority of the system inertia comes from thermal generators which are substituted by new RES as the energy transition unfolds. The distribution of inertia over the grid is not uniform, there is more inertia in the center of the grid.

When a generator is not rotating at its nominal frequency an asynchronous torque, mainly due to Eddy currents in the damper windings, appears which tend to restore its frequency. The corresponding "damping" power P_i^{d} is generally difficult to calculate, nevertheless it can be obtained under some assumptions, in particular that the damping power is solely produced by the damper windings [78]. Conventional generators have damper windings which have different tasks as: providing starting torque, suppressing hunting phenomenon, preventing distortion of the voltage wave shape and damping the oscillations [79]. Damping coefficients d_i of conventational generators are obtained for each generator type from Eq. (5.24) and Table 4.3 in Ref. [78] and the damping power reads

$$P_i^{\text{d}} = -d_i \omega_i. \tag{4.7}$$
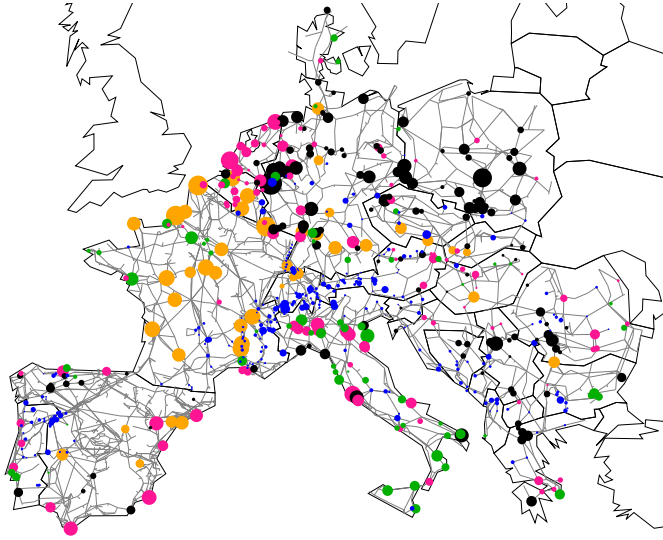
Figure 4.4 – *Inertia parameters of generators in our model of the synchronous grid of continental Europe. The disk size is proportional to m_i and the colors label hydro (blue), nuclear (orange), gas (magenta), coal (black) and other (green) power plants.*

	H_s [s]
hydro	4
nuclear	6
lignite	6
hard coal	6
gas	6
other	3

Table 4.2 – *Inertia constants for different technologies of conventional generators, they correspond to the maximal values found in Ref. [80].*

Frequency dependent loads

In dynamical analyses, the assumption that the consumer buses consist of frequency dependent loads is frequently made [81, 82]. This means that the load L_i at consumer bus #i differs from its nominal value $L_i^{(0)}$ when this bus is subject to a frequency deviation ω_i given by

$$L_i = L_i^{(0)} + d_i \omega_i \equiv L_i^{(0)} + \Delta L_i, \tag{4.8}$$

where $d_i > 0$ is the load frequency coefficient. The frequency dependence of loads was experimentally investigated [83, 84]. The results are given in the form

$$\frac{\Delta L_i}{L_i^{(0)}} = \alpha \frac{\omega_i}{\omega_0}, \tag{4.9}$$

with the frequency sensibility $\alpha \in 0.8 - 2$ [83, 84]. From Eqs.(4.8) and (4.9) the load frequency coefficient d_i reads

$$d_i = \frac{\alpha L_i^{(0)}}{\omega_0}. \tag{4.10}$$

In this work, we use $\alpha = 1.5$.

Structure preserving model

A dynamical power system model with frequency dependent loads is often called a *structure preserving model* [81]. We briefly resume the characteristics of our structure preserving model. We denote $\mathcal{V}_{\text{gen}} \subset \mathcal{V}$ the subset of buses corresponding to generator buses. Their dynamics is described by the swing equations [78, 81]

$$m_i \dot{\omega}_i + d_i \omega_i = P_i^{(0)} - P_i^{\text{e}}, \text{ if } i \in \mathcal{V}_{\text{gen}}, \tag{4.11}$$

where $P_i^{(0)} \equiv P_i^{\text{m}}$ is the power input, m_i is the inertia and d_i the damping coefficients of the generator at the bus #i. The complement subset $\mathcal{V}_{\text{load}} = \mathcal{V} \setminus \mathcal{V}_{\text{gen}}$ contains inertialess generator or consumer buses with frequency dependent loads [81] and their dynamics determined by

$$d_i \omega_i = P_i^{(0)} - P_i^{\text{e}}, \text{ if } i \in \mathcal{V}_{\text{load}}, \tag{4.12}$$

where $P_i^{(0)} \equiv -L_i^{(0)}$ is the load prior to the disturbance. We consider that Eqs. (4.11) and (4.12) are written in a rotating frame with the rated frequency of $\omega_0 = 2\pi f_0$ with $f_0 = 50$ or 60 Hz, in which case $\sum_{i \in \mathcal{V}} P_i^{(0)} = 0$.

In this work, the primary control of frequency is modeled by a damping term in the swing equations describing the dynamics of generators. This is a relatively strong approximation, it corresponds to assuming an instantaneous response of the control. In reality, generators have deadbands in which the no frequency regulation is performed and governors regulate the response of the generators as a negative feedback loop [85]. This leads to a time delay and a ramping of the response. This means that our model probably overestimates the effects of primary control.

4.1.3 Numerical integration

The results presented in Sections 4.2 and 4.3 are obtained by numerical integration of the system dynamics described by Eqs. (4.11) and (4.12). At first, we used the well-known *Kunge-Kutta fourth-order* method and we faced numerical stability problems. This forced us to use very small time steps and therefore long computation times were necessary to obtain the simulations. We circumvented these problems by changing the integration method to the *Radau5* method which was specially developed for the resolution of stiff differential equations [86].

4.2 Disturbance following an abrupt power loss

In this section, we study the system disturbance following an abrupt power loss. We motivate our choice to focus our investigations on the rates of change of frequency (RoCoFs). We observe that the disturbance magnitude strongly depends on the location of the fault. From spectral decomposition of the network Laplacian, we show that the main contributions to the

RoCoFs come from the slowest eigenmodes of the grid. In order to corroborate this observation, we perform a systematic investigation. For this purpose, we introduce a disturbance magnitude measure based on local RoCoFs.

In order to investigate transient dynamics following a plant outage, we consider abrupt power losses $P_i^{(0)} \to P_i^{(0)} - \Delta P$ with $\Delta P = 900$ MW on the European grid and 500 MW on the ERCOT grid. In both cases, faults are localized on single power plants and are only performed on power plants with $P_i^{(0)} \geq \Delta P$. The values of ΔP are chosen so that many contingencies with different locations homogeneously distributed over the whole grid can be investigated. Frequency changes are then calculated from Eqs. (4.11) and (4.12), with initial conditions given by their stationary solution and the faulted bus #b treated as a load bus with power injection $P_b = P_b^{(0)} - \Delta P$, vanishing inertia, $m_b = 0$.

4.2.1 Disturbance monitoring and measuring

The question we address in the following is how to monitor the propagation and to quantify the magnitude of disturbances in transmission systems. The answer naturally depends on the characteristics of the system in particular of its size. Different measures were introduced to quantity a disturbance of the system, the most often used ingredients are frequency deviations in frequency nadirs and RoCoFs. Here we compare the evolution of frequency deviations and RoCoFs for a large transmission system as conventional generators are substituted by new inertialess generators. There is no close-form solution for the local frequency nadirs. However, from Eqs. (4.11) and (4.12), we can obtain the post-fault f_{pf} which reads

$$f_{\text{pf}} = \omega_{\text{pf}} / (2\pi) = \Delta P \Big/ \Big(2\pi \sum_{i \in \mathcal{V}} d_i \Big). \tag{4.13}$$

For our winter evening case, we get $\sum_{i \in \text{load}} d_i \approx 1800$ MWs and $\sum_{i \in \text{gen}} d_i \approx 3100$ MWs. For a power loss $\Delta P = 900$ MW the post-fault frequency deviation $f_{\text{pf}} \approx 30$ mHz. In the hypothetical case where no conventional generator is connected to the grid the frequency dependence of the loads is sufficient to maintain the post-fault frequency deviation to $f_{\text{pf}} \approx 80$ mHz. For comparison, the first wave of load-shedding occurs for a frequency deviation 1 Hz [78]. We conclude that the frequency deviations remain generally small in large transmission grids.

To investigate the evolution of RoCoFs, we introduce the system frequency $f_{\text{sys}} = \omega_{\text{pf}} / (2\pi)$ where

$$\omega_{\text{sys}} \equiv \frac{\sum_{i \in \mathcal{V}_{\text{gen}}} m_i \omega_i}{\sum_{i \in \mathcal{V}_{\text{gen}}} m_i} . \tag{4.14}$$

f_{sys} is also known as the frequency of the center of inertia [87]. After a fault, the initial system RoCoF depends on the power imbalance ΔP in the system and system inertia M_{sys} and reads

$$\text{RoCoF}_{\text{sys}} \equiv \frac{\mathrm{d} f_{\text{sys}}}{\mathrm{d} t} \Big|_{t=0^+} = \frac{\Delta P}{2\pi M_{\text{sys}}} , \tag{4.15}$$

where $M_{sys} = \sum_{i \in \mathcal{V}_{gen}} m_i$. From Eq. (4.15), we obverse that, for a given loss of power ΔP, $RoCoF_{sys}$ varies depends on the inertia that is connected to the system. We observe that the initial system RoCoF diverges when the system inertia vanishes. The system inertia M_{sys} depends on the generation fleet and it varies from hour to hour. Furthermore, as the penetration of inertialess new RES increases, conventional generators contribute less predominantly to electricity production leading to a lower system inertia. We can qualitatively investigate the evolution of $RoCoF_{sys}$ with our pan-European power dispatch algorithm, described in Chapter 2. For each hour of the year, the system inertia $M_{sys}(t)$ is approximately given by

$$M_{sys}(t) \simeq \sum_{i,s} 2 H_s P_i^s(t)/\omega_0 \,, \tag{4.16}$$

where H_s is the inertia constant of the technology #s and $P_i^s(t)$ the corresponding production in the zone #i.

Fig. 4.5 shows the distribution of $RoCoF_{sys}$ after a 900 MW power loss in the continental European grid based on the hourly historical production profiles of the year 2017 from ENTSO-E database [14] and the production profiles we obtained for the year 2030. In 2017, $RoCoF_{sys}$ is on average equal to 28 mHz/s and hardly ever exceeds 40 mHz/s. The narrowness of the current RoCoF distribution results from the fact that currently there is always a fleet of baseload power plants. The distribution of $RoCoF_{sys}$ for the year 2030 is broader. Its average only slightly increase to 35 mHz/s, but it reaches 100 mHz/s for a few hours in the year.
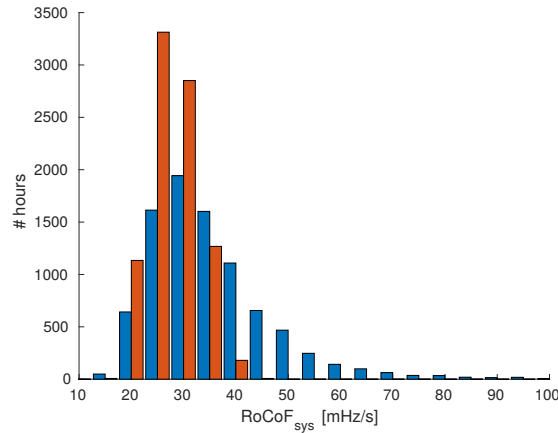

Figure 4.5 – *Initial RoCoF in Continental Europe in the years 2017 (red) and 2030 (blue) for a 900 MW power loss.*

In large power systems, RoCoFs seem to be better indicators of the severity of a disturbance following a localized contingency than frequency deviation which will remain small due to sufficient primary control and load response.

4.2.2 Disturbance propagation following abrupt power losses

In the following we first illustrate that location of a fault strongly affects the magnitude of the resulting system disturbance. We show that this cannot be explained by the inhomogeneity of inertia in the system. Then we perform a spectral decomposition of the local RoCoFs under the assumption of homogeneous inertia and damping in the system. We observe that the slowest eigenmodes have larger contributions to the RoCoF than fastest eigenmodes, at least when the RoCoFs are measured over a time period higher than a few 100 ms.

The starting point of the following investigation is the observation that, for a given amount of lost power ΔP, the propagation of the disturbance in the system strongly differs from a fault location to another. Indeed, Fig. 4.6 shows series of snapshots illustrating the propagation of the disturbance over the continental European grid for two different fault locations which only differ by the location of the power loss. In the top row the faulted power plant is in Greece, while in the bottom row it is in Switzerland. In both instances, the lost power is $\Delta P = 900$ MW and the grid, including loads and feed-ins, inertia distribution, damping parameters and electrical parameters of all power lines, is the same. The two disturbance propagations shown are dramatically different. For a fault in Greece, RoCoFs reach 0.5 Hz/s for times up to 2s. The disturbance seems to propagate through the continental European grid while only disturbing slightly the geometrical center of the grid. For a fault in Switzerland, on the other hand, RoCoFs never exceed 0.1 Hz/s and the disturbance does not propagate beyond few hundred kilometers. Finally we observe that local RoCoFs can be significantly higher than $\text{RoCoF}_{\text{sys}}$.
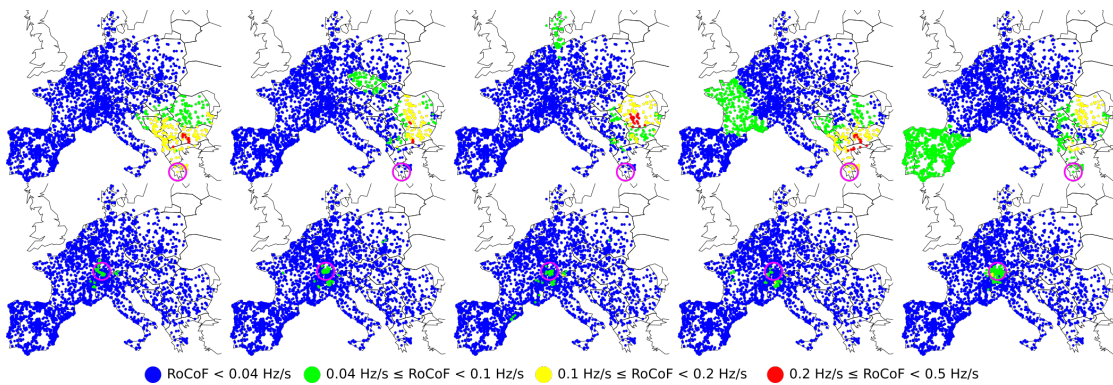
Figure 4.6 – *Spatio-temporal evolution of local RoCoFs for two different power losses of $\Delta P = 900$ MW in a moderate load (typical of a standard summer evening) configuration of the synchronous grid of continental Europe of 2018. The top five panels correspond to a fault in Greece and the bottom five to a fault in Switzerland. In both cases, the fault location is indicated by a purple circle. Panels correspond to snapshots over time intervals 0-0.5[s], 0.5-1[s], 1-1.5[s], 1.5-2[s] and 2-2.5[s] from left to right.*

One might argue that these different behaviors are due to the distribution of inertia in the European grid. Indeed, there is more inertia close to the geometric center of Europe than in the periphery of the grid as shows Fig. 4.4. To investigate the influence of inertia distribution on frequency disturbance propagation, we artificially reduce the inertia in France by a factor

two or alternatively double the inertia present in the Balkans. By investigating the same fault locations as in Fig. 4.6, we find that when inertia is reduced in France, the disturbance following the fault in Switzerland propagates more in France. On the other hand, it has almost no effect on the propagation of the Greek fault. Fig. 4.7 (a) shows how the fault in Greece disturbs the local frequency of three buses in the Balkan, France and Spain with the actual inertia distribution, while Fig. 4.7 (b) shows local frequency deviations for the same fault at the same buses but with the inertia in France reduced by a factor two. By comparing Fig. 4.7 (a) and (b), we observe that this inertia reduction had a negligible effect on the Greek fault. Increasing the inertia in the Balkan mitigates the maximal RoCoFs in this region, however for the Greek fault, the relatively strong RoCoFs are still present for time $t > 2$ s. We therefore conclude that the inhomogeneous distribution of inertia in the system cannot alone explain the difference in the disturbance propagation we observed in Fig. 4.6. We perform the same investigation for our winter evening case. As the total load is higher, more generators are producing to the grid and more inertia is present in the system. Consequently the RoCoFs are reduced, nevertheless we also find distinct disturbance propagations depending on where faults occur.
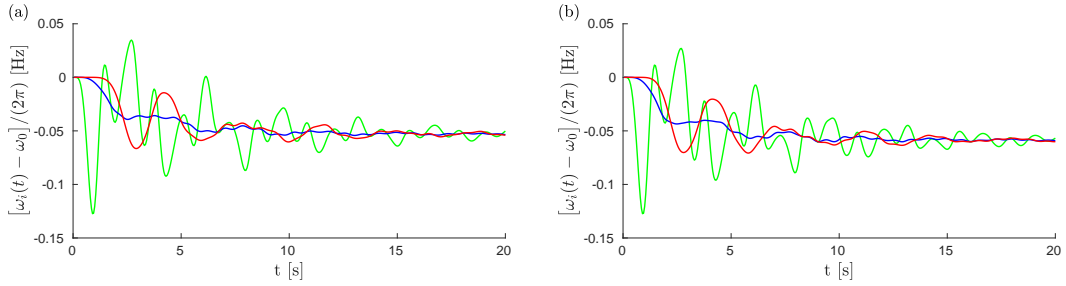
Figure 4.7 – *Frequency deviations for the fault in Greece (same location as in Fig. 4.6) and (b) in the top row of Fig. 4.6 [with inertia in France reduced by a factor of two compared to panel (a)], for three buses in the Balkans (green), France (blue) and Spain (red).*

We can gain some qualitative understanding into disturbance propagations through spectral graph theory under simplifying assumptions on model parameters. The spectral decomposition applied to transmission grid is presented in Section 5.2. In real power grids frequencies are monitored at discrete time intervals $t \rightarrow k\Delta t$, with Δt ranging between 40 ms and 2 s [88]. RoCoFs are then evaluated as the frequency slope between two such measurements. Energy Networks Association recommends a time delay of 0.5 s in the RoCoF determination for distributed generators in the UK [89]. We follow its recommendation and set $\Delta t = 0.5$ s. The RoCoF at the bus #i reads

$$r_i(t) = \frac{\omega_i(t + \Delta t) - \omega_i(t)}{2\pi\Delta t}.$$

(4.17)

Spectral decomposition

In the following, we use some elements of spectral analysis to interpret our simulations of disturbance propagations. Spectral analysis to applied power systems has a long history [80, 78, 90]. The Lyapunov spectrum is used to determine the linear stability of power systems, see for instance Refs. [91, 92, 93]. Spectral decomposition of the network Laplacian is often used for graph partition [94, 95]. The relation between the smallest non-zeros eigenvalue, the corresponding eigenvector and the disturbance propagation is investigated in Ref. [96]. Tamrakar et al. [97] studied the disturbance propagations for different grid structures. They show that the localization, the damping and the propagation speed of the disturbances strongly depend on the meshness of the grid. Spectral analysis is used to understand inter-area oscillations, buses are clustered by using the slowest eigenmodes of the system dynamics. This approach is called *slow coherency* [90].

Spectral decomposition is not the only approach to investigate the disturbance propagation in large transmission grids. Alternatively, transmission grids can be treated as continuums and disturbance propagations are described in terms of electromechanical waves in this medium [98, 99, 100].

Anticipating the results we obtain in Section 5.3, for an uniform distribution of inertia and primary control in the system, we get

$$r_i(t) = \frac{\Delta P e^{-\gamma t/2}}{\pi m} \sum_\alpha \frac{u_{\alpha i} u_{\alpha b}}{f_\alpha \Delta t} \left[\sin\left(\frac{f_\alpha (t + \Delta t)}{2} \right) - \sin\left(\frac{f_\alpha t}{2} \right) \right], \tag{4.18}$$

where $f_\alpha = \sqrt{4\lambda_\alpha^{(0)}/m - \gamma^2}$ and $\lambda_\alpha^{(0)}$ is the αth eigenvalue of the network Laplacian. For more information on spectral decomposition, see Section 5.2. The term $\alpha = 1$ gives a position-independent contribution to $r_i(t)$. All other terms $\alpha > 1$ have oscillations with both amplitude and period depending on $f_\alpha/2$. Eigenmodes with large α and large eigenvalues λ_α therefore contribute much less than eigenmodes with small α, both because their oscillation amplitude is reduced and because they oscillate faster, which leads to faster cancellation of terms. With our choice of $\Delta t = 0.5$ s we find $f_2 \Delta t \in [1.08, 823]$ for $\alpha > 1$ in our model. The second lowest value is $f_3 \Delta t = 1.78$, almost twice larger than the first one. One expects that only few eigenmodes of the network Laplacian, corresponding to its smallest non-zero eigenvalues, effectively matter in the spectral sum in Eq. (4.18).
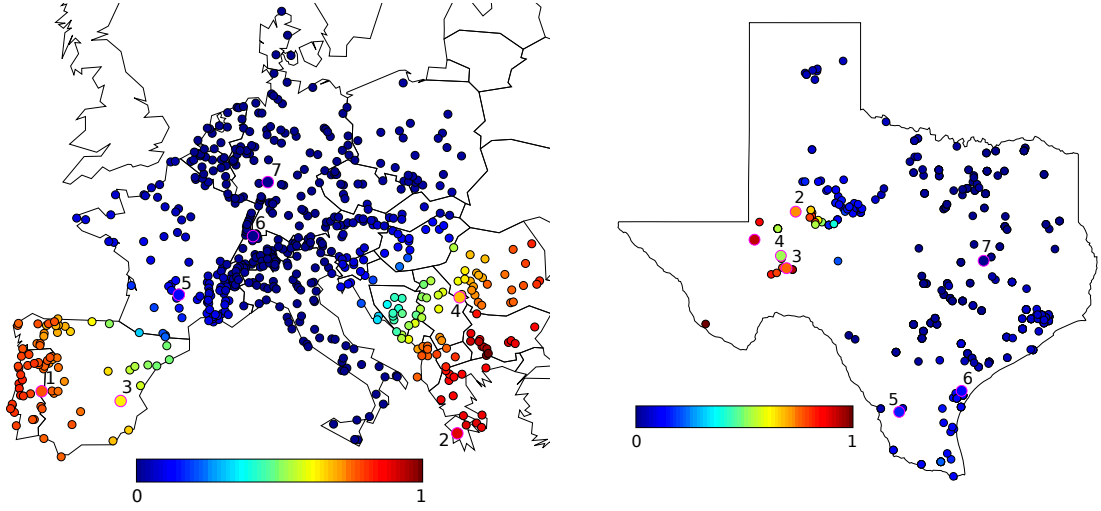
Figure 4.8 – *Color plot of the normalized squared components u_{2k}^2 of the Fiedler vector on generator buses in the European and ERCOT grids. Labeled buses correspond to labeled symbols in Figs. 4.9 and 4.10. The Texas ERCOT transmission grid is taken from Ref. [68] and we obtained inertia and damping coefficients using the same procedure as for the European model.*

Eq. (4.18) shows that, for homogeneous inertia and damping, the short-time RoCoF response $r_i(t)$ is inversely proportional to the inertia. The behavior at longer times is determined by the magnitude of the few slowest eigenmodes of the network Laplacian both on the fault location and the bus where the RoCoF is measured. This simple spectral analysis seems to demonstrate that the distinct disturbance propagations shown in Fig. 4.6 is related to different excitations of the slowest eigenmodes of the network Laplacian. Indeed, in focusing on the Fiedler vector we observe that the Greek fault excites this mode while the Swiss fault does not, see Fig. 4.8. The Fiedler ($\alpha = 2$) vector is located in the peripheral areas of the grid and avoid its center, the same observation was made for the German grid in Ref. [96]. We find that the third ($\alpha = 3$) eigenmode has essentially the symmetric counterpart to the asymmetric Fiedler vector, see Fig. 5.1 in Section 5.2. This means that $\{u_{3i}^2\}$ is similar to squared Fiedler components $\{u_{2i}^2\}$. Furthermore, the next eigenmodes $\alpha = 4, \ldots 6$ largely avoid the geometric center of continental Europe. Higher modes have $f_{\alpha>6}\Delta t > 4f_2\Delta t$, accordingly, their contribution to r_i in Eq. (4.17) are at least four times smaller and oscillate four times faster than the Fiedler mode.

In the following, we perform a systematic investigation of the relationship between disturbance magnitudes and the Fiedler vector. To assess the disturbance magnitude of a power loss at the bus #b over the whole grid, one needs to gather information on RoCoFs at different times and locations. We therefore introduce the performance measure

$$\mathcal{M}_b = \sum_{k=1}^{N_{\text{sim}}} \sum_{i\in\mathcal{V}} \left| r_i(k\Delta t) \right|, \tag{4.19}$$

where $N_{\text{sim}} = 10$ is the number of time intervals $\Delta t = 0.5$ s considered in our numerics. Fig. 4.7 shows that the total time $N_{\text{sim}}\Delta t = t_{\text{sim}} = 5$ s considered in our numerical calculation of $\mathcal{M}_b$ is

set to include major initial oscillations while neglecting oscillations at longer times which are of little concern.

Our spectral analysis suggests that RoCoFs are larger following power losses on buses with large components of the eigenvectors with smallest eigenvalues of the Laplacian matrix. To check whether this result also holds in realistic power grids with inhomogeneous distribution of inertia, we numerically calculate $\mathcal{M}_b$ for 20 abrupt power losses homogeneously distributed on the European and ERCOT grids. Fig. 4.9 shows that the disturbance magnitude $\mathcal{M}_b$ grows with the squared Fiedler component u_{2b}^2 of the location #b of the power loss. The disturbance magnitude is more than twice larger in the European grid and almost three times larger in the ERCOT grid for power losses on buses with largest u_{2b}^2, than for losses on buses with low u_{2b}^2. We have found that the same trend persists when plotting $\mathcal{M}_b$ against the squared component u_{3b}^2 of the second slowest mode of the Laplacian. The magnitude of the disturbance following an abrupt power loss is therefore determined by its location, in particular on the amplitude $u_{\alpha b}^2$ on the faulted bus #b of the Fiedler mode ($\alpha = 2$) and of the next slowest mode ($\alpha = 3$) of the network Laplacian. In the following, we call "Fiedler areas" ("non-Fiedler areas") the set of buses $\{i\}$ where u_{2i}^2 and u_{3i}^2 are large (small).
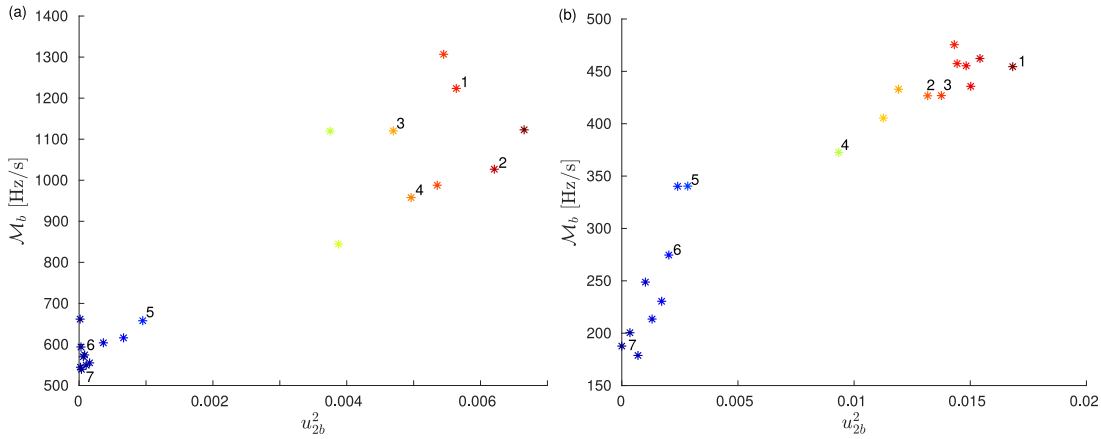
Figure 4.9 – *Global RoCoF disturbance magnitude $\mathcal{M}_b$ as a function of squared Fiedler components u_{2b}^2 for power losses on 20 different bus #b for (a) the European and (b) the ERCOT grid. Labeled symbols correspond to locations indicated in Fig. 4.8. The plots look similar when $\mathcal{M}_b$ is plotted against the squared component u_{3b}^2 of the second slowest mode of the Laplacian.*

4.3 Disturbance magnitude and the placement of inertia

We showed that disturbance magnitudes are dependent on the fault locations. Stronger disturbances follow the faults exciting the slowest eigenmodes of the network Laplacian.

As new RES are inertialess producers, their increasing penetration leads to low inertia situations [101]. The lack of rotational inertia rises important issues of power grid stability, which is of much higher concern to transmission system operators than the volatility of the RES productions [102, 103, 104]. For a fixed amount of inertia, meshed grids are more resilient to

disturbances [105]. We finish our investigations by varying the amount and the distribution of inertia connected to the grid.

We modify inertia on the network following three different procedures where the inertia of a generator on bus #i is increased/decreased according to one of the following probability distributions

$$p_i^{\mathrm{U}} \propto 1, \qquad \text{(uniformly)} \qquad\qquad (4.20)$$

$$p_i^{\mathrm{F}} \propto u_{2i}^2, \qquad \text{(mainly in Fiedler areas)} \qquad (4.21)$$

$$p_i^{\mathrm{nF}} \propto 1/u_{2i}^2. \qquad \text{(mainly in non-Fiedler areas)} \qquad (4.22)$$

The three distributions reduce/add inertia uniformly, preferentially on buses with large squared Fiedler components and preferentially on buses with small squared Fiedler components.
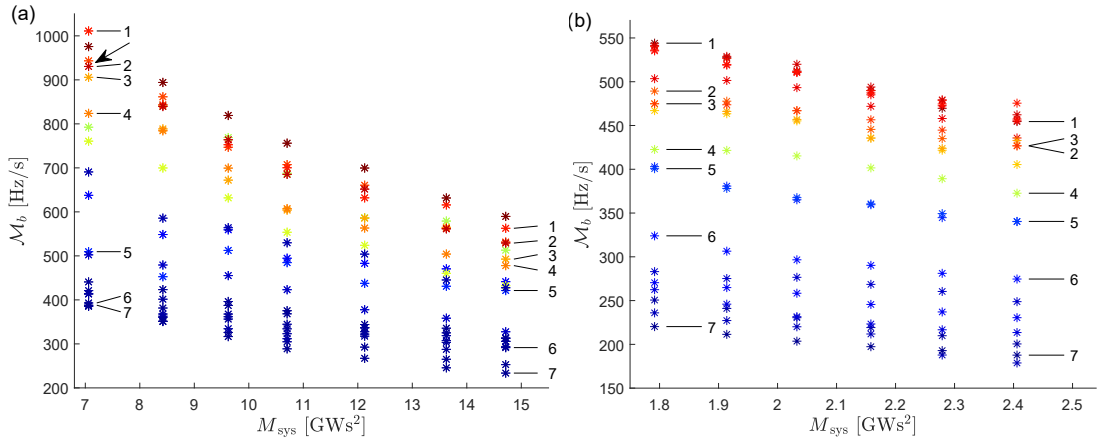
Figure 4.10 – *Global RoCoF disturbance magnitude $\mathcal{M}_b$ as the system inertia M_{sys} is artificially uniformly reduced in the European grid (a) and in the ERCOT grid (b). Each point corresponds to the loss of a single power station, with colors related to the squared component u_{2b}^2 of the Fiedler vector on the power loss bus. Color code and label symbols are the same as in Fig. 4.8. The arrow indicates the data point corresponding to the top left data point, also indicated by an arrow in Fig. 4.11.*

Fig. 4.10 shows the evolution of $\mathcal{M}_b$ as a function of total inertia, $M_{\mathrm{sys}} = \sum_i m_i$, for power losses of $\Delta P = 900$ MW on the same 20 power plants as in Fig. 4.9. The data corresponding to today's synchronous grid of continental Europe are the rightmost, with the largest amount of inertia. The inertia is then reduced following the first procedure where generator buses become randomly inertialess according to the homogeneous probability distribution (4.20). One sees that $\mathcal{M}_b$ follows the ranking defined by the squared Fiedler components, almost regardless of the amount of inertia in the system, and faults in the Fiedler areas are generically more critical than those in the non-Fiedler areas.

The situation can be dramatically different when inertia is added/removed in certain areas following the other two distributions $\{p_i^{\mathrm{F}}\}$ and $\{p_i^{\mathrm{nF}}\}$. In Fig. 4.11, the top left data point

(indicated by an arrow) corresponds to the data labeled 2 in the top left of Fig. 4.10 (also indicated by an arrow). Paths (1) and (3) correspond to adding inertia according to procedure described by Eq. (4.22), i.e. mostly outside the Fiedler area. This procedure reduces $\mathscr{M}_b$ by less than 10 % while increasing the total inertia M_{sys} by 30 %. Path (2) follows procedure described by Eq. (4.21) by adding inertia almost exclusively on the Fiedler area. This is much more efficient and leads to a reduction of $\mathscr{M}_b$ by more than 30 % with the same total increase of M_{sys} by 30 %. Finally, path (4) illustrates a procedure where inertia is removed from Fiedler areas and added to non-Fiedler areas. In that case, the RoCoF disturbance magnitude increases, even with a global increase of inertia. Path (4), when taken in reverse direction, shows that grid resilience against faults such as power losses can be enhanced while simultaneously reducing the total amount of inertia.
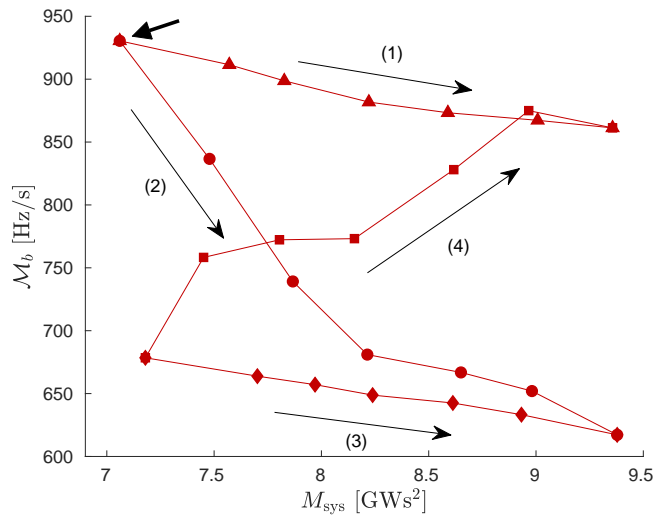
Figure 4.11 – *Global RoCoF disturbance magnitude $\mathscr{M}_b$ vs. artificially modified total system inertia. Along paths (1) and (3), inertia is added according to procedure* (4.22), *i.e. mostly on the non-Fiedler area. Path (2) follows procedure* (4.21) *by adding inertia almost exclusively on the Fiedler area. Path (4) follows a selected procedure where inertia is removed from the Fiedler area and added on the non-Fiedler area. The top left data point corresponds to the data point indicated by an arrow in Fig. 4.10.*

We finally show in Fig. 4.12 how global RoCoF disturbance magnitudes depend on the location of each of the 20 power losses considered in Fig. 4.10. The three data sets correspond to unchanged inertia $M_{\mathrm{sys}}^0 = 14.7$ GWs^2 (crosses), inertia $M_{\mathrm{sys}} = 0.6 M_{\mathrm{sys}}^0$ reduced mostly in the Fiedler area, following the probability distribution (4.21) (empty circles) or outside the Fiedler area, according to (4.22) (full circles). Fig. 4.12 clearly shows that (i) regardless of the position of the fault, inertia reduction on the Fiedler area systematically leads to an enhanced sensitivity to power loss, compared to inertia reduction outside the Fiedler area and (ii) the sensitivity increase is larger for faults on the Fiedler area.
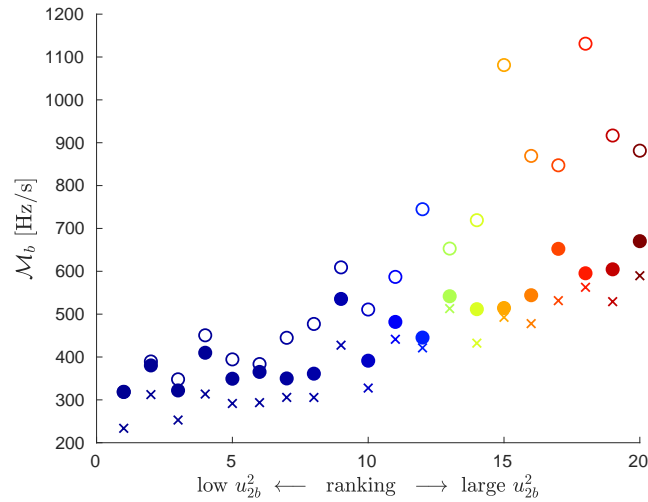
Figure 4.12 – *Global RoCoF disturbance magnitude $\mathcal{M}_b$ horizontally ranked in increasing order of the squared Fiedler mode amplitude u_{2b}^2 on the faulted bus #b. Crosses are for a system with inertia $M_{\text{sys}}^0 = 14.7$ GWs^2 (corresponding to today's European grid, Fig. 4.6) and circles for reduced inertia $M_{\text{sys}} = 0.6 M_{\text{sys}}^0$, with system inertia mainly reduced outside Fiedler areas (solid circles) or mainly reduced inside Fiedler areas (empty circles).*

4.4 Conclusion

In this chapter we investigated the propagation of disturbances in large transmission grids. To that purpose, we developed a dynamical model of continental European transmission grid from publicly available databases. We showed that in large transmission grids the frequency deviations remain small even if a large share of the conventional generators are substituted by inertialess new RES and we conclude that for large transmission grids RoCoFs are better disturbance indicators.

We found that the magnitude of the disturbance following an abrupt power loss depends on the fault location. To perform a systematic investigation, we introduced a performance measure based on local RoCoFs. We were able to relate the magnitude of the disturbances to the excitation of the slowest eigenmodes of the network Laplacian. In particular we showed that the disturbance magnitudes are higher for faults occurring on buses with exciting Fiedler mode, the eigenmode associated with the smallest non-zero eigenvalue of the network Laplacian. We call the portion of the grid containing those buses with large squared Fiedler components the Fiedler areas. We found that inertia reduction on the Fiedler area leads to an amplified RoCoF response, while reducing the inertia on non-Fiedler area has a much weaker effect, with only a moderate increase of local RoCoFs.

Our findings emphasize an important aspect of optimal inertia location. Our results show that the substitution of a large share of the German coal-fired or the French nuclear power plants by new RES seems feasible without jeopardizing the reliability of the continental European grid. This is a consequence of the fact that these generators are located in the non-Fiedler

area of the continental European grid. On the other hand, our results dissuade from reducing the inertia in the Fiedler areas (the Balkan and Spain). These areas might benefit from local additions of virtual inertia or synchronous condensers for a harmonious incorporation of new RES in their energy mixes.

In short, in this chapter we found that:

- For large transmission grids, RoCoFs are better indicators of the disturbance magnitude than the frequency deviations.
- The disturbance magnitude following a localized fault depends on how much it excites the slowest eigenmodes of the system in particular the Fielder vector.
- A power system is more resilient when more inertia is present in its "Fiedler areas".

The results presented in Section 4.3 highlight the importance of optimal placement of inertia. In low inertia power systems, inverters of the new RES can emulate inertia with proper control [106, 107, 108]. In Chapter 5, we continue to investigate the relationship between the spectral decomposition of the network Laplacian and the magnitude of disturbances following abrupt power losses. We use this spectral decomposition to perform a perturbation theory analysis and we are able to develop algorithms to distribute inertia and primary control optimally.

5 Optimal placement of inertia and primary control

The problem addressed in this chapter is closely related to the one addressed in the previous chapter, where we investigated the propagation of disturbances in large transmission grids following abrupt localized power losses. We showed that, when the system inertia is reduced in certain portions of the grid, the Fiedler areas, it becomes less resilient against contingencies, in particular those occurring in these areas. In this chapter we seek the optimal placement of inertia and primary control in transmission grids to maximize their resilience against localized contingencies. For that purpose, we introduce a mathematical $\mathscr{L}_2-$norm performance measure based on local frequency deviations. The system dynamics and consequently our performance measure have closed-form expressions under strong assumptions as uniform damping ratios. To circumvent this limitation, we apply perturbation theory to obtain closed-form approximate expression of the system dynamics and of our measure when some mild inhomogeneities are present in the distributions of inertia and primary control. Section 5.1 gives an introduction to perturbation theory. Spectral decomposition is applied to power systems in Section 5.2. Section 5.3 deals with the case where inertia and primary control are uniformly distributed in the system. The performance measure that quantifies system disturbances is introduced and we calculate its value for abrupt power losses. In Section 5.4 we apply matrix perturbation theory to calculate the sensitivities of our measure in local variations of inertia and primary control. Section 5.5 presents the optional placement of inertia and primary control in the case of weak inhomogeneity. In Section 5.6 we apply our optimal placements to the continental European grid. Most of the results presented in this chapter will be published in an upcoming article [109].

There are different approaches to tackle the problem of the optimal placement of inertia and primary control which lead either to more analytical or more numerical results. Analytical results often require strong assumptions and/or simplifications of the dynamical model. They rely on the minimization of performance measures based on $\mathscr{H}_p$ or $\mathscr{L}_p$ norms [110, 111, 112], which are rather far from what the transmission grid operators are able to measure. Poolla et al. proposed a different placement optimization based on the minimization of $\mathscr{H}_2$ norms [111], while Pirani et al. adopted an approach based on $\mathscr{H}_\infty$ norms [112]. On the other hand, the

minimization of quantities, as local RoCoFs or frequency deviations that can be measured in transmission grids, has usually no close-form solution and is obtained with numerical methods. Borsche et al. evaluated damping ratios and transient overshoots to optimize the placement of virtual inertia [113]. Borsche and Dörfler extended the latter work to minimize the maximal RoCoF or frequency deviation by an optimal placement of inertia [114]. There are attempts to bridge the gap by finding analytical expressions for quantities measurable in real transmission grids [115].

5.1 An introduction to perturbation theory

Perturbation theory is widely used in Theoretical Physics and consequently this topic is treated in introductory textbooks on quantum mechanics, see for instance Refs. [116, 117]. Outside the Physics community, this method is little known. The following is a brief explanation of perturbation theory, it is mainly intended as an assistance for non-physicists to better understand Section 5.4 where we apply perturbation theory to power system dynamics. Perturbation theory relies on the idea that, when one adds a small term to a system that was already diagonalized, the eigenvalues and eigenvectors of the full system (the initial system and the small term) must only slightly differ from those of the initial system and that one can compute the corrections.

In the following, we apply perturbation theory to a simple two-state system and we compare the approximate expressions of its eigenvalues and eigenvectors we obtain with their exact expressions. Our simple system H consists in an already diagonalized H_0 and a small perturbation λV, with $\lambda \ll 1$ a dimensionless small parameter.

$$
H = \left[\begin{array}{cc} \varepsilon_1^{(0)} & 0 \\ 0 & \varepsilon_2^{(0)} \end{array} \right] + \lambda \left[\begin{array}{cc} 0 & \Delta \\ \Delta & 0 \end{array} \right] \equiv H_0 + \lambda V,
\tag{5.1}
$$

where $0 < \varepsilon_1^{(0)}, \varepsilon_2^{(0)}, \Delta$. Without loss of generality, we assume that $\varepsilon_1 < \varepsilon_2$. H is easily diagonalisable, its eigenvalues read

$$
\varepsilon_1 = \left[\varepsilon_1^{(0)} + \varepsilon_2^{(0)} - \sqrt{\xi} \right] / 2,
\tag{5.2}
$$

$$
\varepsilon_2 = \left[\varepsilon_1^{(0)} + \varepsilon_2^{(0)} + \sqrt{\xi} \right] / 2,
\tag{5.3}
$$

where $\xi = \left(\varepsilon_2^{(0)} - \varepsilon_1^{(0)} \right)^2 + 4\lambda^2 \Delta^2$. The corresponding eigenbasis reads

$$
\frac{1}{n_+ n_-} \left[\begin{array}{cc} \lambda \Delta n_+ & \lambda \Delta n_- \\ \left(\varepsilon_1 - \varepsilon_1^{(0)} \right) n_+ & \left(\varepsilon_2 - \varepsilon_1^{(0)} \right) n_- \end{array} \right],
\tag{5.4}
$$

where $n_\pm = \sqrt{ \left(\varepsilon_2^{(0)} - \varepsilon_1^{(0)} \pm \sqrt{\xi} \right) \left(\varepsilon_2^{(0)} - \varepsilon_1^{(0)} \right) / 2 + 2\lambda^2 \Delta^2 }$. The first (second) column is the eigenvector associated with $\varepsilon_1 (\varepsilon_2)$. In the following we use Dirac notation, the eigenvectors of H_0

are denoted

$$|1^{(0)}\rangle \equiv \begin{pmatrix} 1 \\ 0 \end{pmatrix}, \; |2^{(0)}\rangle \equiv \begin{pmatrix} 0 \\ 1 \end{pmatrix} \text{ and their transposes } \langle 1^{(0)}| \equiv \begin{pmatrix} 1 & 0 \end{pmatrix}, \langle 2^{(0)}| \equiv \begin{pmatrix} 0 & 1 \end{pmatrix}. \quad (5.5)$$

The relationship between $\boldsymbol{H}$ and its eigenvalues and eigenvectors, in Dirac notation, reads

$$\boldsymbol{H}|n\rangle = \varepsilon_n |n\rangle, \quad (5.6)$$

In the following derivation, we depart from our simple system and treat the general case of a N-state system. We assume that eigenvalues and eigenvectors can be expended in power series

$$\varepsilon_n = \sum_{i=0}^{\infty} \lambda^i \varepsilon_n^{(i)}, \quad (5.7)$$

$$|n\rangle = \sum_{i=0}^{\infty} \lambda^i |n^{(i)}\rangle, \quad (5.8)$$

in particular we know that if $\lambda = 0$, then $\varepsilon_n = \varepsilon_n^{(0)}$ and $|n\rangle = |n^{(0)}\rangle$. We want the eigenvectors of $\boldsymbol{H}$ to be unitary which imposes

$$\langle n \mid n \rangle = \sum_{i=0}^{\infty} \sum_{j=0}^{\infty} \lambda^{i+j} \langle n^{(i)} | n^{(j)} \rangle = 1, \quad (5.9)$$

which in order of λ reads

- zeroth order: $\langle n^{(0)} | n^{(0)} \rangle \equiv 1$,
- first order: $\langle n^{(1)} | n^{(0)} \rangle + \langle n^{(0)} | n^{(1)} \rangle$,
- second order: $\langle n^{(2)} | n^{(0)} \rangle + \langle n^{(1)} | n^{(1)} \rangle + \langle n^{(0)} | n^{(2)} \rangle$,
- …

The zeroth order contribution to Eq. (5.9) imposes that the other contributions vanish, in particular $\langle n^{(1)} | n^{(0)} \rangle \equiv \langle n^{(0)} | n^{(1)} \rangle = 0$. Inserting Eqs. (5.7) and (5.8) into Eq. (5.6), it becomes

$$\left(\boldsymbol{H_0} - \lambda \boldsymbol{V} \right) \sum_{i=0}^{\infty} \lambda^i |n^{(i)}\rangle = \sum_{i=0}^{\infty} \sum_{j=0}^{\infty} \lambda^{i+j} \varepsilon_n^{(i)} |n^{(i)}\rangle, \quad (5.10)$$

which in order of λ reads

- zeroth order: $\boldsymbol{H_0}|n^{(0)}\rangle = \varepsilon_n^{(0)}|n^{(0)}\rangle$,
- first order: $\boldsymbol{H_0}|n^{(1)}\rangle + \boldsymbol{V}|n^{(0)}\rangle = \varepsilon_n^{(0)}|n^{(1)}\rangle + \varepsilon_n^{(1)}|n^{(0)}\rangle$,
- second order: $\boldsymbol{H_0}|n^{(2)}\rangle + \boldsymbol{V}|n^{(1)}\rangle = \varepsilon_n^{(0)}|n^{(2)}\rangle + \varepsilon_n^{(1)}|n^{(1)}\rangle + \varepsilon_n^{(2)}|n^{(0)}\rangle$,
- …

Multiplying by $\langle n^{(0)}|$ the first order contribution to Eq. (5.6), we obtain

$$\varepsilon_n^{(1)} = \langle n^{(0)} | \boldsymbol{V} | n^{(0)} \rangle. \quad (5.11)$$

The eigenvectors of H_0 form a orthonormal basis which leads to the completeness relation

$$\sum_{n=1}^{N} |n^{(0)}\rangle\langle n^{(0)}| = \mathbb{1}_N, \tag{5.12}$$

where $\mathbb{1}_N$ is the $N \times N$ identity matrix. Using this relationship in the first order contribution to Eq. (5.6), we obtain

$$|n^{(1)}\rangle = \sum_{k \neq n} \frac{\langle k^{(0)}|V|n^{(0)}\rangle}{\varepsilon_n^{(0)} - \varepsilon_k^{(0)}} |k^{(0)}\rangle, \tag{5.13}$$

The second order corrections are obtained similarly, they read

$$\varepsilon_n^{(2)} = \sum_{k \neq n} \frac{\langle k^{(0)}|V|n^{(0)}\rangle}{\varepsilon_n^{(0)} - \varepsilon_k^{(0)}}, \tag{5.14}$$

$$|n^{(2)}\rangle = \sum_{k \neq n} \sum_{l \neq n} \frac{\langle k^{(0)}|V|l^{(0)}\rangle\langle l^{(0)}|V|n^{(0)}\rangle}{\left(\varepsilon_n^{(0)} - \varepsilon_l^{(0)}\right)\left(\varepsilon_n^{(0)} - \varepsilon_k^{(0)}\right)} |k^{(0)}\rangle - \sum_{k \neq n} \frac{\langle n^{(0)}|V|n^{(0)}\rangle\langle k^{(0)}|V|n^{(0)}\rangle}{\left(\varepsilon_n^{(0)} - \varepsilon_k^{(0)}\right)^2} |k^{(0)}\rangle$$
$$- \frac{1}{2} \sum_{k \neq n} \frac{\langle k^{(0)}|V|n^{(0)}\rangle^2}{\left(\varepsilon_n^{(0)} - \varepsilon_k^{(0)}\right)^2} |k^{(0)}\rangle, \tag{5.15}$$

As the computation of corrections becomes more and more tedious as the orders increase, third or higher order corrections are rarely computed. From Eqs. (5.11), (5.13) – (5.15), we compute the first non-vanishing corrections to the first eigenvalue and to the corresponding eigenvector of H. For the first order corrections, we get

$$\varepsilon_1^{(1)} = \langle 1^{(0)}|V|1^{(0)}\rangle = 0, \tag{5.16}$$

$$|1^{(1)}\rangle = \frac{\langle 2^{(0)}|V|1^{(0)}\rangle}{\varepsilon_1^{(0)} - \varepsilon_2^{(0)}} |2^{(0)}\rangle = \frac{\Delta}{\varepsilon_1^{(0)} - \varepsilon_2^{(0)}} \begin{pmatrix} 0 \\ 1 \end{pmatrix} \tag{5.17}$$

As the first order correction $\varepsilon_1^{(1)}$ vanishes, we compute the second order correction

$$\varepsilon_1^{(2)} = \langle 1^{(0)}|V|2^{(0)}\rangle^2 / \left(\varepsilon_1^{(0)} - \varepsilon_2^{(0)}\right) = \Delta^2 / \left(\varepsilon_1^{(0)} - \varepsilon_2^{(0)}\right). \tag{5.18}$$

To compare theses results with those in Eqs. (5.2) and (5.4), we first note that, if $\lambda \ll 1$, $\sqrt{\xi} \approx \varepsilon_2^{(0)} - \varepsilon_1^{(0)} - 2\lambda^2\Delta^2/(\varepsilon_2^{(0)} - \varepsilon_1^{(0)})$, from which we find that

$$\varepsilon_1 - \varepsilon_1^{(0)} \approx \lambda^2\Delta^2 / \left(\varepsilon_1^{(0)} - \varepsilon_2^{(0)}\right), \tag{5.19}$$

$$n_- \approx \lambda\Delta. \tag{5.20}$$

From Eq. (5.19), we find that $\varepsilon_1 \approx \varepsilon_1^{(0)} + \lambda^2\varepsilon_1^{(2)}$. Inserting Eqs. (5.19) and (5.20) into the first row of Eq. (5.4), we get that $|1\rangle$ is approximately equal to

$$\begin{pmatrix} 1 \\ \lambda\Delta/(\varepsilon_1^{(0)} - \varepsilon_2^{(0)}) \end{pmatrix}, \tag{5.21}$$

which is equivalent to $|1^{(0)}\rangle + \lambda |1^{(1)}\rangle$. Perturbation theory therefore allowed us to correctly approximate the first eigenvector and eigenvalue of $\boldsymbol{H}$.

In this section, we applied the perturbation theory to a simple system that can be exactly diagonalized for educational purposes. Hovever, the true strength of perturbation theory lies in the fact that it gives approximate expressions of eigenvalues and eigenvectors for system which cannot be analytically diagonalized as we show in Section 5.4.

5.2   Spectral decomposition applied to transmission grids

In this section, we introduce the network Laplacian $\boldsymbol{L}$ and perform its spectral decomposition. The spectral decomposition approach used here has recently drawn the attention of a number of groups and has been used to calculate performance measures in power grids and consensus algorithms e.g. in Refs. [115, 112, 118, 119].

In Section 1.3, we showed that, within the lossless approximation, the power flow equations are given by

$$P_i = \sum_j V_i V_j b_{ij} \sin\left(\theta_i - \theta_j\right). \tag{5.22}$$

Here, we assume constant voltage magnitudes $\left(V_i \equiv V_i^{(0)}, \ \forall i\right)$ and we label $\{\theta_i^{(0)}\}$ the solutions of Eq. (5.22). In the vicinity of these solutions, with $\theta_i(t) = \theta_i^{(0)} + \delta\theta_i(t)$, the deviations $\{\delta\theta_i\}$ in voltage phases under a change in active power $P_i \to P_i + \delta P_i$, can be obtained by linearizing Eq. (5.22),

$$\delta P_i = \sum_j V_i^{(0)} V_i^{(0)} b_{ij} \cos\left(\theta_i^{(0)} - \theta_j^{(0)}\right)\left(\delta\theta_i - \delta\theta_j\right). \tag{5.23}$$

In matrix form, it reads

$$\boldsymbol{\delta P} = \boldsymbol{A} \operatorname{diag}\left(\{b_k \cos(\delta_k)\}\right) \boldsymbol{A}^\top \boldsymbol{\delta\theta} \equiv \boldsymbol{L}\boldsymbol{\delta\theta}, \tag{5.24}$$

where $\boldsymbol{A}$ is the incidence matrix of the network [see Eq. (1.33) for its definition], $b_k \equiv V_i^{(0)} V_j^{(0)} b_{ij}$ the weighted admittance of the line #k which connects the buses #i and #j and $\delta_k \equiv \theta_i^{(0)} - \theta_j^{(0)}$ the phase difference on this line. As we showed in Section 1.3, $\boldsymbol{A}^\top \mathbb{1}_{N\times 1} = \mathbb{O}_{N\times 1}$, therefore $\mathbb{1}_{N\times 1}$ is an eigenvector of $\boldsymbol{L}$ associated with the eigenvalue zero. The Laplacian matrix is real and symmetric, it can be diagonalized by unitary transformation $\boldsymbol{U}^{(0)}$,

$$\boldsymbol{L} = \boldsymbol{U}^{(0)\top} \boldsymbol{\Lambda}^{(0)} \boldsymbol{U}^{(0)}, \tag{5.25}$$

where $\Lambda^{(0)} = \operatorname{diag}\left(\{\lambda_1^{(0)} = 0, \ldots, \lambda_2^{(0)}, \lambda_N^{(0)}\}\right)$, $\boldsymbol{U}^{(0)} = \left[\boldsymbol{u}_1^{(0)}, \ldots, \boldsymbol{u}_N^{(0)}\right]$ is the eigenbasis of $\boldsymbol{L}$. The superscript $^{(0)}$ denotes that the terms are related to the network Laplacian $\boldsymbol{L}$. With the proper normalization to be unitary, we obtain $\boldsymbol{u}_1^{(0)} = (1, \ldots, 1)/\sqrt{N}$ associated with $\lambda_1 = 0$. If the grid is

connected, as in our case, all other eigenvalues of L are strictly positive, $\lambda_\alpha > 0$, $\forall \alpha > 1$. Due to their orthogonality to $\boldsymbol{u}_1^{(0)}$ the other eigenvectors $\{\boldsymbol{u}_\alpha\}$ satisfy $\sum_i u_{\alpha i}^{(0)} = 0$, $\forall \alpha > 1$.

Fig. 5.1 shows the eigenvalues $\lambda_\alpha^{(0)}$ and the eigenvectors corresponding to the six smallest non-zero eigenvalues of the continental European transmission grid. In particular, we note that the $\lambda_\alpha \gg \lambda_2$ for $\alpha \gtrsim 6$. Fig. 5.1 (2) – (7) show that the slowest eigenmodes of the network Laplacian are mainly located in the peripheral areas of the grid.
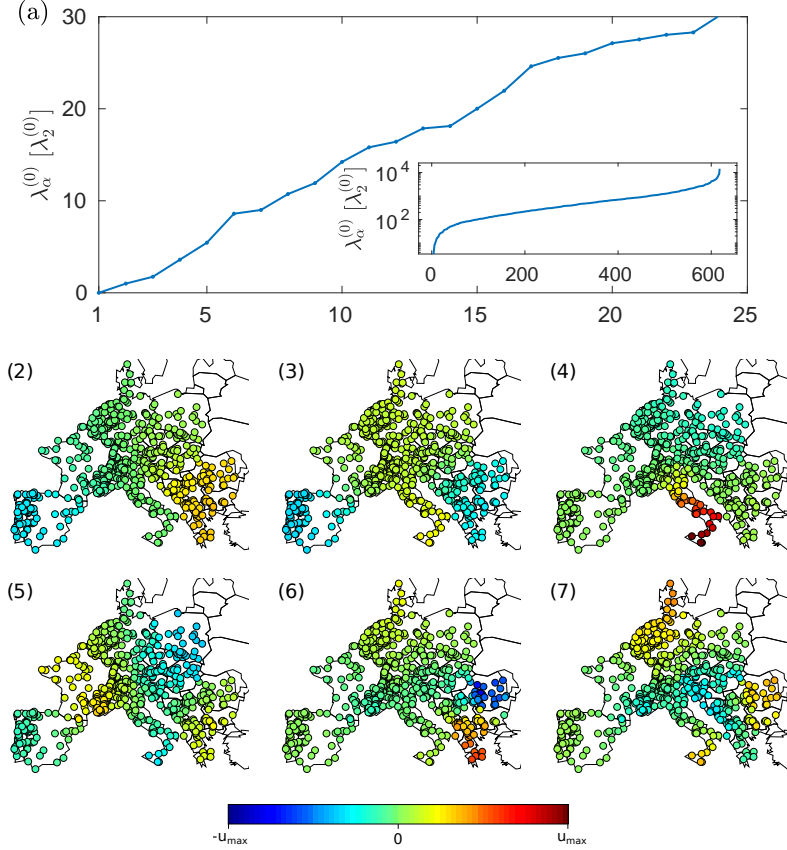
Figure 5.1 – *(a) Eigenvalues $\{\lambda_\alpha^{(0)}\}$ of the network Laplacian L. Panels (2)-(7) display the eigenvectors corresponding to $\{\lambda_2^{(0)}, \ldots, \lambda_7^{(0)}\}$, colors span the interval $[-u_{\max}, u_{\max}]$ where $u_{\max} = \max_{\alpha \in \{2, \cdots, 7\}} |u_{\alpha i}^{(0)}|$.*

First eigenvector of the inertia weighted Laplacian

Later in this chapter, we need the expression of the first eigenvector of $\boldsymbol{L_M} = \boldsymbol{M}^{-1/2} \boldsymbol{L} \boldsymbol{M}^{-1/2}$. From Eq. (5.24) and the discussion below it, we find that the vector $\left(m_1^{1/2}, \ldots, m_N^{1/2}\right)$ is an eigenvector of L_M associated with the eigenvalue zero. Once normalized, the first eigenvector $\boldsymbol{u}_1$ of $\boldsymbol{L_M}$ associated with the eigenvalue zero is a unit vector and we find that

$$u_{1i} = \sqrt{\frac{m_i}{\sum_j m_j}}, \quad \forall i, \tag{5.26}$$

5.2.1 Resistance distances and centrality

In the following, we introduce the resistance distances and show that a centrality measure can be derived from them. Finally, we use resistance distances to cluster the buses of the continental European grid into areas. This clustering increases the readability of our time domain simulations presented in Section 5.6.

Resistance distances were first introduced in Ref. [120]. The resistance distance between buses #i and #j is given by

$$\Omega_{ij} = L_{ii}^{\ddagger} + L_{jj}^{\ddagger} - L_{ij}^{\ddagger} - L_{ji}^{\ddagger}, \tag{5.27}$$

where $L^{\ddagger}$ is the Moore–Penrose pseudo inverse of L which is a particular case of the pseudo-inverses we presented the the end of Section 1.3. It can be expressed as

$$L^{\ddagger} = U^{(0)\top} \mathrm{diag}\big(\{0, \lambda_2^{(0)-1}, \cdots, \lambda_N^{(0)-1}\}\big) U^{(0)}. \tag{5.28}$$

With Eq. (5.28), we can reformulate Eq. (5.27) as

$$\Omega_{ij} = \sum_{\alpha > 1} \big(u_{\alpha i}^{(0)} - u_{\alpha j}^{(0)}\big)^2 / \lambda_{\alpha}^{(0)}. \tag{5.29}$$

A centrality measure, called *resistance centrality*, can be obtained from resistance distances [121], it is expressed by

$$C_i = N \Big(\sum_j \Omega_{ij}\Big)^{-1}. \tag{5.30}$$

The larger C_i is, the more central the bus #i is.

Areal clustering

For the sake of readability of our results in Section 5.6, we average bus frequencies into areal frequencies. We obtain these areas with k-mean clustering [122] based on their resistance distances defined in Eq. (5.27).

k-means algorithm:
1. k randomly chosen buses become the centroids $\{c_\alpha\}$
2. asign each bus #i to the nearest centroid #c_α to get $S_\alpha = \big\{i \mid c_\alpha = \mathrm{argmin}_{\beta = \{1,...,k\}} \Omega_{ic_\beta}\big\}$, $\forall \alpha$
3. redefine the centroids as $c_\alpha = \mathrm{argmin}_{i \in S_\alpha} \sum_{j \in S_\alpha} \Omega_{ij}$, $\forall \alpha$
4. repeat steps 2 and 3 until convergence

We choose $k = 8$ which is a good compromise between readability and spatial resolution. The results of the k-means partitioning depends on the initial set of centroids. We quantify the

goodness of a partition by computing

$$\mathcal{R} = \sum_{\alpha=1}^{k} \sum_{i \in S_\alpha} \Omega_{ic_\alpha}, \tag{5.31}$$

We applied k-means algorithm with 10^4 different initial conditions, the optimal partition minimizing $\mathcal{R}$ is displayed in Fig. 5.2.
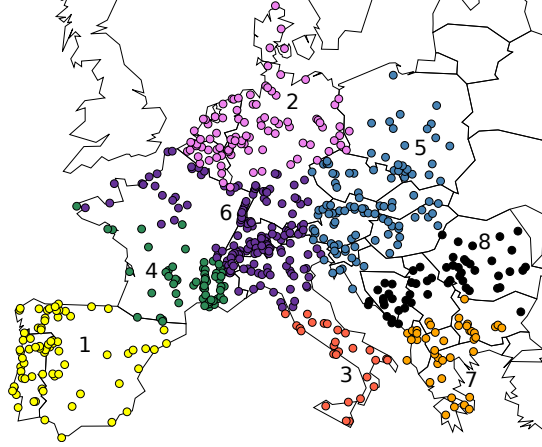
Figure 5.2 – *Areas obtained by k-means clustering based on resistance distances.*

5.3 Unperturbed system dynamics

For a better comprehension of the Sections 5.3 to 5.5, we sketch the general approach as follows.

When the damping ratios are homogeneous over the grid, the system dynamics decouples when it is expressed with the eigenmodes $\{\xi_\alpha\}$ of the inertia-weigthed network Lapacian L_M. As $\{\xi_\alpha\}$ are independent from each other, their closed-form solutions for an abrupt power loss is straightforward to obtain. We want to quantify the disturbance following a localized abrupt power loss and therefore we introduce a disturbance measure $\mathcal{M}_b$ and obtain its closed-form expression. When, furthermore, we assume that inertia is uniformly distributed in the grid, we observe that the faults exciting the slowest eigenmodes of the network Laplacian L have higher values of the disturbance measure.

When some inhomogeneity is present in the inertia distribution, disturbance measure depends on the eigenvectors and eigenvalues of L_M which only slightly differ from those of $m^{-1}L$ where m is the average inertia. We apply perturbation theory to obtain the corrections. With them, we compute the sensitivities of the disturbance measure in local changes in inertia distribution. When some inhomogeneity is present in the damping ratios, the system dynamics is no more directly related to the eigenmodes of L_M. Once again we apply perturbation theory, we get approximate expressions describing the system dynamics when some mild homogeneities

are present in the damping ratios. From these expressions, we deduce the sensitivities of our measure to local changes in damping ratios. We derive algorithms to optimally place inertia and primary control from those sensitivities.

5.3.1 Transmission grid model

To obtain closed-form expressions describing the system dynamics, we must simplify the structure preserving model we introduced in Chapter 4. Here we assume that every bus has inertia. In Section 4.1.2, we showed that the dynamics of buses with inertia is governed by the swing equations,

$$m_i \dot{\omega}_i + d_i \omega_i = P_i - \sum_j B_{ij} \sin\left(\theta_i - \theta_j\right), \tag{5.32}$$

where m_i is the local inertia and d_i the local damping coefficients (primary control). We introduce the damping ratio $\gamma_i \equiv d_i/m_i$. In the vicinity of a stable point $\{\theta_i^{(0)}\}$, we can linearize Eq. (5.32) to obtain

$$\boldsymbol{M}\dot{\boldsymbol{\omega}} + \boldsymbol{D}\boldsymbol{\omega} = \boldsymbol{\delta P} - \boldsymbol{L}\boldsymbol{\delta\theta}, \tag{5.33}$$

where $\boldsymbol{M} = \text{diag}(\{m_i\})$, $\boldsymbol{D} = \text{diag}(\{d_i\})$.

5.3.2 Exact solution for homogeneous damping ratio

When the damping ratio is constant, $d_i/m_i = \gamma_i = \gamma$, $\forall i$, Eq. (5.33) can be integrated exactly [123, 114, 115, 124]. To see this we first transform angle coordinates as $\boldsymbol{\delta\theta} = \boldsymbol{M}^{-1/2}\boldsymbol{\delta\theta_M}$ to obtain

$$\dot{\boldsymbol{\omega}}_M + \underbrace{\boldsymbol{M}^{-1}\boldsymbol{D}}_{\boldsymbol{\Gamma}}\boldsymbol{\omega}_M + \underbrace{\boldsymbol{M}^{-1/2}\boldsymbol{L}\boldsymbol{M}^{-1/2}}_{\boldsymbol{L_M}}\boldsymbol{\delta\theta_M} = \boldsymbol{M}^{-1/2}\boldsymbol{\delta P}, \tag{5.34}$$

where we introduced the diagonal matrix $\boldsymbol{\Gamma} = \text{diag}(\{d_i/m_i\}) \equiv \text{diag}(\{\gamma_i\})$. The inertia-weighted Laplacian matrix $\boldsymbol{L_M}$ is real and symmetric, therefore it can be diagonalized

$$\boldsymbol{L_M} = \boldsymbol{U}^\top \boldsymbol{\Lambda} \boldsymbol{U} \tag{5.35}$$

with an orthogonal matrix $\boldsymbol{U}$, the αth row of which gives the components $u_{\alpha,i}$, $i = 1,\dots N$ of the αth eigenvector $\boldsymbol{u}_\alpha$ of $\boldsymbol{L_M}$. The diagonal matrix $\boldsymbol{\Lambda} = \text{diag}(\{\lambda_1 = 0, \lambda_2, \cdots, \lambda_N\})$ contains the eigenvalues of $\boldsymbol{L_M}$ with $\lambda_\alpha < \lambda_{\alpha+1}$. For connected networks only the smallest eigenvalue λ_1 vanishes, which follows from the zero row and column sum property of the Laplacian matrix $\boldsymbol{L_M}$. Rewriting Eq. (5.34) in the basis diagonalizing $\boldsymbol{L_M}$ gives

$$\ddot{\boldsymbol{\xi}} + \boldsymbol{U}\boldsymbol{\Gamma}\boldsymbol{U}^\top\dot{\boldsymbol{\xi}} + \boldsymbol{\Lambda}\boldsymbol{\xi} = \boldsymbol{U}\boldsymbol{M}^{-1/2}\boldsymbol{\delta P}, \tag{5.36}$$

where $\delta\boldsymbol{\theta}_M = \boldsymbol{U}^\top\boldsymbol{\xi}$. This change of coordinates is nothing but a spectral decomposition of angle deviations $\delta\boldsymbol{\theta}_M$ into their components in the basis of eigenvectors of $\boldsymbol{L}_M$. These components are cast in the vector $\boldsymbol{\xi}$. The formulation of the problem in Eq. (5.36) makes it clearer that, if $\boldsymbol{\Gamma}$ is a multiple of identity, the problem can be reformulated as a set of ordinary differential equations that can be exactly integrated. This is done below in Eq. (5.42), and provides an exact solution on which we construct a matrix perturbation theory in the next section.

Proposition 1 (Unperturbed evolution) *For an abrupt power loss, $\delta P(t) = \delta P\,\Theta(t)$ with the Heaviside step function $\Theta(t)$, and with homogeneous damping ratio, $\boldsymbol{\Gamma} = \gamma\,\mathbb{1}_N$ with the $N \times N$ identity matrix $\mathbb{1}_N$, the frequency coordinates $\dot{\xi}_\alpha$ evolve independently as*

$$\dot{\xi}_\alpha(t) = \frac{2\mathscr{P}_\alpha}{f_\alpha} e^{-\gamma t/2} \sin\left(\frac{f_\alpha t}{2}\right), \forall \alpha > 1, \tag{5.37}$$

where $f_\alpha = \sqrt{4\lambda_\alpha - \gamma^2}$ and $\mathscr{P}_\alpha = \sum_i u_{\alpha i}\,\delta P_i/m_i^{1/2}$.

This result generalizes Theorem III.3 of Ref. [118].

Proof: The proof goes along the lines of the diagonalization procedure proposed in [115, 124, 125]. Eq. (5.36) can be rewritten as

$$\frac{\mathrm{d}}{\mathrm{d}t}\begin{bmatrix} \boldsymbol{\xi} \\ \dot{\boldsymbol{\xi}} \end{bmatrix} = \underbrace{\begin{bmatrix} \mathbb{0}_N & \mathbb{1}_N \\ -\boldsymbol{\Lambda} & -\gamma\,\mathbb{1}_N \end{bmatrix}}_{\boldsymbol{H}_0}\begin{bmatrix} \boldsymbol{\xi} \\ \dot{\boldsymbol{\xi}} \end{bmatrix} + \begin{bmatrix} \mathbb{0}_{N\times 1} \\ \mathscr{P} \end{bmatrix}, \tag{5.38}$$

where $\mathscr{P} = \boldsymbol{U}\boldsymbol{M}^{-1/2}\delta\boldsymbol{P}$, $\mathbb{0}_{N\times M}$ is the $N \times M$ matrix of zeroes and $\mathbb{1}_N$ is the $N \times N$ identity matrix. The matrix $\boldsymbol{H}_0$ is block-diagonal up to a permutation of rows and columns [124], and can easily be diagonalized block by block, where each 2×2 block corresponds to one of the eigenvalues λ_α of $\boldsymbol{L}_M$. The αth block is diagonalized by the transformation

$$\begin{bmatrix} \chi_{\alpha+}^{(0)} \\ \chi_{\alpha-}^{(0)} \end{bmatrix} = \boldsymbol{T}_\alpha^L\begin{bmatrix} \xi_\alpha \\ \dot{\xi}_\alpha \end{bmatrix}, \quad \boldsymbol{T}_\alpha^L \equiv \frac{i}{f_\alpha}\begin{bmatrix} \mu_{\alpha-}^{(0)} & -1 \\ -\mu_{\alpha+}^{(0)} & 1 \end{bmatrix}, \tag{5.39}$$

$$\begin{bmatrix} \xi_\alpha \\ \dot{\xi}_\alpha \end{bmatrix} = \boldsymbol{T}_\alpha^R\begin{bmatrix} \chi_{\alpha+}^{(0)} \\ \chi_{\alpha-}^{(0)} \end{bmatrix}, \quad \boldsymbol{T}_\alpha^R \equiv \begin{bmatrix} 1 & 1 \\ \mu_{\alpha+}^{(0)} & \mu_{\alpha-}^{(0)} \end{bmatrix}, \tag{5.40}$$

with the eigenvalues $\mu_{\alpha\pm}^{(0)}$ of the αth block,

$$\mu_{\alpha\pm}^{(0)} = -\frac{1}{2}\left(\gamma \mp i f_\alpha\right). \tag{5.41}$$

The two rows (columns) of $\boldsymbol{T}_\alpha^L\,(\boldsymbol{T}_\alpha^R)$ give the nonzero components of the two left (right)

eigenvectors $\boldsymbol{t}_{\alpha\pm}^{(0)L}$ ($\boldsymbol{t}_{\alpha\pm}^{(0)R}$) of $\boldsymbol{H}_0$. Following this transformation, Eq. (5.38) reads

$$\frac{\mathrm{d}}{\mathrm{d}t}\begin{bmatrix} \chi_{\alpha+}^{(0)} \\ \chi_{\alpha-}^{(0)} \end{bmatrix} = \begin{bmatrix} \mu_{\alpha+}^{(0)} & 0 \\ 0 & \mu_{\alpha-}^{(0)} \end{bmatrix}\begin{bmatrix} \chi_{\alpha+}^{(0)} \\ \chi_{\alpha-}^{(0)} \end{bmatrix} + \frac{i}{f_\alpha}\begin{bmatrix} -\mathscr{P}_\alpha \\ \mathscr{P}_\alpha \end{bmatrix}. \tag{5.42}$$

The solutions of Eq. (5.42) are

$$\chi_{\alpha\pm}^{(0)} = \pm\frac{i\mathscr{P}_\alpha}{f_\alpha\mu_{\alpha\pm}^{(0)}}\left(1 - e^{\mu_{\alpha\pm}^{(0)}t}\right), \ \forall\alpha > 1. \tag{5.43}$$

Inserting Eq. (5.43) back into Eq. (5.39), one finally finds Eq. (5.37) which proves the proposition. ∎

5.3.3 Performance measure

We want to mitigate disturbances following an abrupt power loss. To that end, we use performance measures which evaluate the overall disturbance magnitude over time and the whole power grid. Performance measures have been proposed, which can be formulated as $\mathscr{L}_2$ and squared $\mathscr{H}_2$ norms of linear systems [111, 115, 124, 125, 126, 127, 128, 129, 130] and are time-integrated quadratic forms in the angle, $\boldsymbol{\delta\theta}$, or frequency, $\boldsymbol{\omega}$, deviations. Here we focus on frequency deviations and use the following performance measure

$$\mathscr{M} = \int\limits_0^\infty \left(\boldsymbol{\omega}^\top - \bar{\boldsymbol{\omega}}^\top\right)\boldsymbol{M}\left(\boldsymbol{\omega} - \bar{\boldsymbol{\omega}}\right)\mathrm{d}t, \tag{5.44}$$

where $\bar{\boldsymbol{\omega}} = \left(\omega_{\text{sys}}, \omega_{\text{sys}}, \dots \omega_{\text{sys}}\right)^\top$ is the instantaneous average frequency vector with components

$$\omega_{\text{sys}}(t) = \sum_i m_i\omega_i(t) \Big/ \sum_i m_i. \tag{5.45}$$

It is straightforward to check that $\mathscr{M}$ reads

$$\mathscr{M} = \int\limits_0^\infty \sum_\alpha \dot{\xi}_\alpha^2(t)\mathrm{d}t - \frac{1}{\sum_k m_k}\int\limits_0^\infty \sum_{\alpha,\beta,i,j} m_i^{1/2}m_j^{1/2}u_{\alpha i}u_{\beta j}\dot{\xi}_\alpha(t)\dot{\xi}_\beta(t)\mathrm{d}t, \tag{5.46}$$

when rewritten in the eigenbasis of $\boldsymbol{L_M}$. From Eq. (5.59), the second term in Eq. (5.46) is equal to $\int_0^\infty \dot{\xi}_1^2(t)\mathrm{d}t$ and we finally get

$$\mathscr{M} = \int\limits_0^\infty \sum_{\alpha>1} \dot{\xi}_\alpha^2(t)\mathrm{d}t. \tag{5.47}$$

Proposition 2 *For an abrupt power loss,* $\boldsymbol{\delta P}(t) = \boldsymbol{\delta P}\Theta(t)$ *on a single bus labeled b,* $\delta P_i =$

$\delta_{ib}\delta P$, and with an homogeneous damping ratio, $\mathbf{\Gamma} = \gamma \mathbb{1}_N$,

$$\mathcal{M}_b = \frac{\delta P^2}{2\gamma m_b} \sum_{\alpha>1} \frac{u_{\alpha b}^2}{\lambda_\alpha}, \tag{5.48}$$

in terms of the eigenvalues λ_α and the components $u_{\alpha b}$ of the eigenvectors $\boldsymbol{u}_\alpha$ of $\boldsymbol{L_M}$.

Note that we introduced the subscript b to indicate that the fault is localized on that bus only. The power loss is modeled as $P_i = P_i^{(0)} - \delta P_i \Theta(t)$ with $\delta P_i = \delta_{ib}\delta P$ with the Kronecker symbol $\delta_{ib} = 1$ if $i = b$ and 0 otherwise.

Proof: Equation (5.37) straightforwardly gives

$$\int_0^\infty \dot{\xi}_\alpha^2(t)\mathrm{d}t = \frac{u_{\alpha b}^2 \delta P^2}{2\gamma m_b \lambda_\alpha}, \alpha > 1, \tag{5.49}$$

which, when summed over $\alpha > 1$ gives Eq. (5.48). $\blacksquare$

Remark 1 *For homogeneous inertia coefficients, $\boldsymbol{M} = m\mathbb{1}_N$, the eigenvector and eigenvalues of the inertia-weighted Laplacian $\boldsymbol{L_M}$ defined in Eq. (5.34) are given by $\boldsymbol{u}_\alpha = \boldsymbol{u}_\alpha^{(0)}$, and $\lambda_\alpha = m^{-1}\lambda_\alpha^{(0)}$, in terms of the eigenvectors $\boldsymbol{u}_\alpha^{(0)}$ and eigenvalues $\lambda_\alpha^{(0)}$ of the Laplacian $\boldsymbol{L}$. In that case, the performance measure reads*

$$\mathcal{M}_b^{(0)} = \frac{\delta P^2}{2\gamma} \sum_{\alpha>1} \frac{u_{\alpha b}^{(0)2}}{\lambda_\alpha^{(0)}}, \tag{5.50}$$

With the resistance centrality defined in Eq. (5.30) and with Eq. (5.27), one can show that [119, 130, 131]

$$\sum_{\alpha>1} \frac{u_{\alpha b}^{(0)2}}{\lambda_\alpha^{(0)}} = C_b^{-1} - N^{-2}Kf_1, \tag{5.51}$$

where Kf_p are the generalized Kirchhoff indices [132, 130], they read

$$Kf_p = N \sum_{\alpha>1} \lambda_\alpha^{-p}, \tag{5.52}$$

Because Kf_1 is a global quantity characterizing the network, it follows from Eqs. (5.50) with Eq. (5.51) that, when inertia and primary control are homogeneously distributed in the system, the disturbance magnitude as measured by $\mathcal{M}_b^{(0)}$ is larger for disturbances on peripheral (less central) buses [69, 133].

5.4 Matrix perturbation

In the previous section, we treated the case where inertia and primary control are uniformly distributed in the system. Our goal is to lift this restriction to obtain $\mathcal{M}_b$ when some mild inhomogeneities are present. We parametrize these inhomogeneities by writing

$$m_i = m + \delta m\, r_i, \tag{5.53}$$

$$d_i = m_i \gamma_i = (m + \delta m\, r_i)(\gamma + \delta\gamma\, a_i), \tag{5.54}$$

with the average m and γ and the maximum deviation amplitudes δm and $\delta\gamma$ of inertia and damping ratio. Inhomogeneities are determined by the coefficients $-1 \le a_i, r_i \le 1$ with $\sum_i r_i = \sum_i a_i = 0$ which are determined following a minimization of the performance measure $\mathcal{M}_b$ (5.44). In the following two paragraphs we construct a matrix perturbation theory to linear order in the inhomogeneity parameters δm, and $\delta\gamma$ to calculate the performance measure $\mathcal{M}_b = \mathcal{M}_b^{(0)} + r_i \rho_i + a_i \alpha_i + \mathcal{O}(\delta m^2, \delta\gamma^2)$. This requires to calculate the susceptibilities $\rho_i \equiv \partial \mathcal{M}_b / \partial r_i$ and $\alpha_i \equiv \partial \mathcal{M}_b / \partial a_i$.

Perturbation theory was applied in the context of electric power grids in Ref. [124, 111] and for consensus networks in Ref. [127]. Coletta et al. used this method to calculate quadratic performance measures following a line fault from the eigenvalues and eigenvectors of the network Laplacian before the fault [124]. Poolla et al. used it to obtain the gradient in their iterative optimization [111]. More generally eigenvalues and eigenvectors sensibilities on the variation of a parameter are used in Refs. [134, 135], they emphasized an interesting correlation between the location of inertia reduction and specific electromechanical modes in the case of increased wind turbine and photovoltaic penetration respectively.

5.4.1 Inhomogeneity in inertia

When inertia is inhomogeneous, but the damping ratios remain homogeneous, the system dynamics and $\mathcal{M}_b$ are still given by Eqs. (5.38) and (5.48). However, the eigenvectors of the inertia-weighted Laplacian matrix $\boldsymbol{L_M}$ differ from those of $\boldsymbol{L}$ and consequently $\mathcal{M}_b$ is no longer equal to $\mathcal{M}_b^{(0)}$. In general there is no simple way to diagonalize $\boldsymbol{L_M}$, but one expects that if the inhomogeneity is weak, then the eigenvalues and eigenvectors of $\boldsymbol{L_M}$ only slightly differ from those of $m^{-1}\boldsymbol{L}$, which allows to construct a perturbation theory.

Assumption 1 (Weak inhomogeneity in inertia) *The deviations $\delta m\, r_i$ of the local inertias m_i are all small compared to their average m. We write $\boldsymbol{M} = m\big[\mathbb{1}_N + \mu\,\mathrm{diag}(\{r_i\})\big]$, where $\mu \equiv \delta m / m \ll 1$ is a small, dimensionless parameter.*

To linear order in μ, the series expansion of $\boldsymbol{L_M}$ reads

$$\boldsymbol{L_M} = \boldsymbol{M}^{-1/2}\,\boldsymbol{L}\,\boldsymbol{M}^{-1/2} = m^{-1}\Big[\boldsymbol{L} + \mu \boldsymbol{V}_1 + \mathcal{O}(\mu^2)\Big], \tag{5.55}$$

with $\boldsymbol{V}_1 = -\left(\boldsymbol{R}\boldsymbol{L}+\boldsymbol{L}\boldsymbol{R}\right)/2$ and $\boldsymbol{R} = \mathrm{diag}(\{r_i\})$. In this form, the inertia-weighted Laplacian matrix $\boldsymbol{L}_M$ is given by the sum of an easily diagonalizable matrix, $m^{-1}\boldsymbol{L}$, and a small perturbation matrix, $(\mu/m)\,\boldsymbol{V}_1$. Truncating the expansion of $\boldsymbol{L}_M$ at this linear order gives an error of order $\sim \mu^2$, which is small under Assumption 1.

Matrix perturbation theory gives approximate expressions for the eigenvectors $\boldsymbol{u}_\alpha$ and eigenvalues λ_α of $\boldsymbol{L}_M$ in terms of those ($\boldsymbol{u}_\alpha^{(0)}$ and $\lambda_\alpha^{(0)}$) of $\boldsymbol{L}$. To leading order in μ one has

$$\lambda_\alpha = m^{-1}\left[\lambda_\alpha^{(0)} + \mu\lambda_\alpha^{(1)} + \mathcal{O}\!\left(\mu^2\right)\right],\tag{5.56}$$

$$\boldsymbol{u}_\alpha = \boldsymbol{u}_\alpha^{(0)} + \mu\boldsymbol{u}_\alpha^{(1)} + \mathcal{O}\!\left(\mu^2\right),\tag{5.57}$$

with

$$\lambda_\alpha^{(1)} = \boldsymbol{u}_\alpha^{(0)\top}\boldsymbol{V}_1\boldsymbol{u}_\alpha^{(0)},\tag{5.58}$$

$$\boldsymbol{u}_\alpha^{(1)} = \sum_{\beta\neq\alpha}\frac{\boldsymbol{u}_\beta^{(0)\top}\boldsymbol{V}_1\boldsymbol{u}_\alpha^{(0)}}{\lambda_\alpha^{(0)}-\lambda_\beta^{(0)}}\boldsymbol{u}_\beta^{(0)}.\tag{5.59}$$

From Eqs. (5.48), (5.56) and (5.57), the first-order approximation of $\mathcal{M}_b$ in μ reads

$$\mathcal{M}_b = \mathcal{M}_b^{(0)} + \frac{\mu\delta P^2}{2\gamma}\sum_{\alpha>1}\lambda_\alpha^{(0)-1}\left(2u_{\alpha b}^{(0)}u_{\alpha b}^{(1)} - r_b u_{\alpha b}^{(0)2} - u_{\alpha b}^{(0)2}\lambda_\alpha^{(0)-1}\lambda_\alpha^{(1)}\right) + \mathcal{O}\!\left(\mu^2\right).\tag{5.60}$$

Proposition 3 *For an abrupt power loss, $\boldsymbol{\delta P}(t) = \boldsymbol{\delta P}\Theta(t)$ on a single bus labeled b, $\delta P_i = \delta_{ib}\delta P$, and under Assumption 1, the susceptibilites $\rho_i \equiv \partial\mathcal{M}_b/\partial r_i$ are given by*

$$\rho_i = -\frac{\mu\delta P^2}{\gamma N}\sum_{\alpha>1}\frac{u_{\alpha b}^{(0)}u_{\alpha i}^{(0)}}{\lambda_\alpha^{(0)}}.\tag{5.61}$$

Proof: Taking the derivative of Eq. (5.60) with respect to r_i, with $\lambda_\alpha^{(1)}$ and $u_{\alpha b}^{(1)}$ given in Eqs. (5.58) and (5.59), one gets

$$\frac{\partial\mathcal{M}_b}{\partial r_i} = \frac{\mu\delta P^2}{2\gamma}\left[\sum_{\substack{\alpha>1\\\beta\neq\alpha}}u_{\alpha b}^{(0)}u_{\beta b}^{(0)}u_{\alpha i}^{(0)}u_{\beta i}^{(0)}\left(\frac{1}{\lambda_\alpha^{(0)}} - \frac{2}{\lambda_\alpha^{(0)}-\lambda_\beta^{(0)}}\right) - \delta_{ib}\sum_{\alpha>1}\frac{u_{\alpha b}^{(0)2}}{\lambda_\alpha^{(0)}}\right.$$
$$\left.+ \sum_{\alpha>1}\frac{u_{\alpha b}^{(0)2}u_{\alpha i}^{(0)2}}{\lambda_\alpha^{(0)}}\right] + \mathcal{O}\!\left(\mu^2\right),\tag{5.62}$$

The first term in the square bracket in Eq. (5.62) gives

$$\sum_{\substack{\alpha>1\\\beta\neq\alpha}}\frac{u_{\alpha b}^{(0)}u_{\beta b}^{(0)}u_{\alpha i}^{(0)}u_{\beta i}^{(0)}}{\lambda_\alpha^{(0)}} = \sum_{\substack{\alpha>1,\\\beta}}\frac{u_{\alpha b}^{(0)}u_{\beta b}^{(0)}u_{\alpha i}^{(0)}u_{\beta i}^{(0)}}{\lambda_\alpha^{(0)}} - \sum_{\alpha>1}\frac{u_{\alpha b}^{(0)2}u_{\alpha i}^{(0)2}}{\lambda_\alpha^{(0)}} = \delta_{ib}\sum_{\alpha>1}\frac{u_{\alpha b}^{(0)2}}{\lambda_\alpha^{(0)}} - \sum_{\alpha>1}\frac{u_{\alpha b}^{(0)2}u_{\alpha i}^{(0)2}}{\lambda_\alpha^{(0)}},\tag{5.63}$$

where we used $\sum_\beta u_{\beta i}^{(0)} u_{\beta b}^{(0)} = \delta_{ib}$. This term therefore exactly cancels out with the last two terms in the square bracket in Eq. (5.62) and one obtains

$$\rho_i = \frac{\partial \mathcal{M}_b}{\partial r_i} = -\frac{\mu \delta P^2}{\gamma} \sum_{\substack{\alpha > 1 \\ \beta \neq \alpha}} \frac{u_{\alpha b}^{(0)} u_{\beta b}^{(0)} u_{\alpha i}^{(0)} u_{\beta i}^{(0)}}{\lambda_\alpha^{(0)} - \lambda_\beta^{(0)}} + \mathcal{O}(\mu^2). \tag{5.64}$$

The argument of the double sum in Eq. (5.64) is odd under permutation of α and β, therefore only terms with $\beta = 1$ survive. With $u_{1i}^{(0)} = 1/\sqrt{N}$, one finally obtains Eq. (5.61). ∎

5.4.2 Inhomogeneity in damping ratios

Eq. (5.37) gives exact solutions to the linearized dynamical problem defined in Eq. (5.36), under the assumption of homogeneous damping ratio, $m_i / d_i \equiv \gamma$. In this section we lift that constraint and write $\gamma_i = \gamma + \delta \gamma \, a_i$. With inhomogeneous damping ratios, Eq. (5.38) becomes

$$\frac{\mathrm{d}}{\mathrm{d}t} \begin{bmatrix} \boldsymbol{\xi} \\ \dot{\boldsymbol{\xi}} \end{bmatrix} = \underbrace{\begin{bmatrix} \mathbb{0}_{N \times N} & \mathbb{1}_N \\ -\boldsymbol{\Lambda} & -\gamma \mathbb{1}_N - \delta \gamma \boldsymbol{V}_2 \end{bmatrix}}_{\boldsymbol{H}} \begin{bmatrix} \boldsymbol{\xi} \\ \dot{\boldsymbol{\xi}} \end{bmatrix} + \begin{bmatrix} \mathbb{0}_{N \times 1} \\ \mathscr{P} \end{bmatrix}, \tag{5.65}$$

which differs from Eq. (5.38) only through the additional term $-\delta \gamma \boldsymbol{V}_2$ with $\boldsymbol{V}_2 = \boldsymbol{U} \boldsymbol{A} \boldsymbol{U}^\top$, $\boldsymbol{A} = \mathrm{diag}(\{a_i\})$. Under the assumption that the dimensionless parameter $g \equiv \delta \gamma / \gamma \ll 1$, this additional term gives only small corrections to the unperturbed problem of Eq. (5.38), and we use matrix perturbation theory to calculate these corrections in a polynomial expansion in g.

Assumption 2 (Weak inhomogeneity in damping ratios) *The deviations $\delta \gamma \, a_i$ of the damping ratio γ_i from their average γ are all small compared to their average. We write $\boldsymbol{\Gamma} = \gamma [\mathbb{1}_N + g \, \mathrm{diag}(\{a_i\})]$, where $g \equiv \delta \gamma / \gamma \ll 1$ is a small, dimensionless parameter.*

We want to integrate Eq. (5.65) using the spectral approach that provided the solutions Eq. (5.43). In principle this requires to know the eigenvalues and eigenvectors of $\boldsymbol{H}$ in Eq. (5.65), which is not possible in general, because $\boldsymbol{V}_2$ does not commute with $\boldsymbol{\Lambda}$. As for $\boldsymbol{L}_M$, we use first order perturbation theory to compute the corrections to eigenvectors and eigenvalues. In this case, as $\boldsymbol{H}$ is not a symmetrical matrix, left and right eigenvectors differ, see Eqs. (5.39) and (5.40) and we must compute their corrections separately. They are given by formulas similar

to Eqs. (5.58) and (5.59),

$$g\,\mu_{\alpha s}^{(1)} = \boldsymbol{t}_{\alpha s}^{(0)L} \begin{bmatrix} \mathbb{O}_{N\times N} & \mathbb{O}_{N\times N} \\ \mathbb{O}_{N\times N} & -\delta\gamma\,\boldsymbol{V}_2 \end{bmatrix} \boldsymbol{t}_{\alpha s}^{(0)R}, \tag{5.66}$$

$$g\,\boldsymbol{t}_{\alpha s}^{(1)R} = \overline{\sum_{\beta,s'}} \frac{\boldsymbol{t}_{\beta s'}^{(0)L} \begin{bmatrix} \mathbb{O}_{N\times N} & \mathbb{O}_{N\times N} \\ \mathbb{O}_{N\times N} & -\delta\gamma\,\boldsymbol{V}_2 \end{bmatrix} \boldsymbol{t}_{\alpha s}^{(0)R}}{\mu_{\alpha s}^{(0)} - \mu_{\beta s'}^{(0)}}\,\boldsymbol{t}_{\beta s'}^{(0)R}, \tag{5.67}$$

$$g\,\boldsymbol{t}_{\alpha s}^{(1)L} = \overline{\sum_{\beta,s'}} \frac{\boldsymbol{t}_{\alpha s}^{(0)L} \begin{bmatrix} \mathbb{O}_{N\times N} & \mathbb{O}_{N\times N} \\ \mathbb{O}_{N\times N} & -\delta\gamma\,\boldsymbol{V}_2 \end{bmatrix} \boldsymbol{t}_{\beta s'}^{(0)R}}{\mu_{\alpha s}^{(0)} - \mu_{\beta s'}^{(0)}}\,\boldsymbol{t}_{\beta s'}^{(0)L}, \tag{5.68}$$

where $\overline{\sum}$ indicates that the sum runs over $(\beta, s') \neq (\alpha, s)$. One obtains

$$g\,\mu_{\alpha s}^{(1)} = -\delta\gamma\Big(\frac{1}{2} + is\frac{\gamma}{2f_\alpha}\Big)V_{2;\alpha\alpha}, \tag{5.69}$$

$$g\,\boldsymbol{t}_{\alpha s}^{(1)R} = 2\,\delta\gamma\,\overline{\sum_{\beta,s'}} \frac{\boldsymbol{V}_{2;\alpha\beta}\,\mu_{\alpha s}^{(0)}}{f_\beta(ss'\,f_\alpha - f_\beta)}\,\boldsymbol{t}_{\beta s'}^{(0)R}, \tag{5.70}$$

$$g\,\boldsymbol{t}_{\alpha s}^{(1)L} = 2\,\delta\gamma\,\overline{\sum_{\beta,s'}} \frac{\boldsymbol{V}_{2;\alpha\beta}\,\mu_{\beta s'}^{(0)}}{f_\alpha(f_\alpha - ss'\,f_\beta)}\,\boldsymbol{t}_{\beta s'}^{(0)L}, \tag{5.71}$$

with $\boldsymbol{V}_{2;\alpha\beta} = \sum_i a_i\,u_{\alpha i}\,u_{\beta i}$.

Remark 2 *By definition, $-1 \leq V_{2;\alpha\alpha} \leq 1$. Therefore, Eq. (5.69) indicates, among others, that when the parameters $\{a_i\}$ are correlated (anticorrelated) with the square components $\{u_{\alpha i}^2\}$ for some α then that mode is more strongly (more weakly) damped. Accordingly, Theorem 2 will distribute the set $\{a_i\}$ to increase the damping of the slow modes of H.*

Proposition 4 *For an abrupt power loss, $\boldsymbol{\delta P}(t) = \boldsymbol{\delta P}\Theta(t)$ on a single bus labeled b, $\delta P_i = \delta_{ib}\delta P$, and under Assumption 2, $\dot{\xi}_\alpha(t)$ reads, to leading order in g,*

$$\dot{\xi}_\alpha(t) = \frac{\mathscr{P}_\alpha}{f_\alpha} e^{-\gamma t/2} \Big[2\Big(s_\alpha + g\frac{\gamma^2}{f_\alpha^2}V_{2;\alpha\alpha}\Big) - g\gamma t V_{2;\alpha\alpha}\Big(s_\alpha + \frac{\gamma}{f_\alpha}c_\alpha\Big)\Big]$$
$$+ g\gamma \sum_{\beta\neq\alpha} \frac{V_{2;\alpha\beta}\mathscr{P}_\beta}{\lambda_\alpha - \lambda_\beta} e^{-\gamma t/2}\Big[\frac{\gamma}{f_\beta}s_\beta - \frac{\gamma}{f_\alpha}s_\alpha + c_\alpha - c_\beta\Big] + \mathcal{O}(g^2), \tag{5.72}$$

where $s_\alpha = \sin(f_\alpha t/2)$ and $c_\alpha = \cos(f_\alpha t/2)$, and $\mathscr{P}_\alpha$ and f_α are defined below Eq. (5.37).

Proof: The proof follows the same steps as for Proposition 1. One first performs a unitary transformation to rewrite Eq. (5.65) in the left and right eigenbasis of H. The unitary matrices $\boldsymbol{T}^{L,R}$ that do this transformation, $\boldsymbol{T}^L \boldsymbol{H} \boldsymbol{T}^R = \text{diag}(\{\mu_{\alpha s}\}) \equiv \boldsymbol{\mu}$, have elements given by components of the left and right eigenvectors of H, which we calculate to first order in g

with Eqs. (5.70)–(5.71). In this basis, one has an equation similar to Eq. (5.42), with perturbed eigenvalues $\{\mu_{\alpha s}\}$ which one also calculates perturbatively to first order in g with Eq. (5.69). The expansion has to be transformed back to the original ξ-basis and this is again done in linear order in g. It is rather tedious, though algebraically straightforward to obtain Eq. (5.72). We sketch the calculational steps.

Following the transformation with $\boldsymbol{T}^{L,R}$, Eq. (5.65) reads

$$\dot{\boldsymbol{\chi}} = \boldsymbol{\mu}\boldsymbol{\chi} + \boldsymbol{T}^L \begin{bmatrix} \mathbb{0}_{N\times 1} \\ \mathscr{P} \end{bmatrix} \equiv \boldsymbol{\mu}\boldsymbol{\chi} + \tilde{\mathscr{P}}. \tag{5.73}$$

The solutions of Eq. (5.73) read

$$\chi_{\alpha\pm} = -\frac{\tilde{\mathscr{P}}_{\alpha\pm}}{\mu_{\alpha\pm}}\Big(1 - e^{\mu_{\alpha\pm}t}\Big), \ \forall \alpha > 1, \tag{5.74}$$

Using Eqs. (5.69)–(5.71) one calculates the eigenvalues and eigenvector components of $\boldsymbol{H}$ from those of $\boldsymbol{H}_0$ and the first-order corrections in g and next we compute the first order approximate expressions of Eqs. (5.73) and (5.74). Including the first-order correction in g, $\boldsymbol{T}_\alpha^L$ reads

$$T_\alpha^L = \begin{pmatrix} \boldsymbol{t}_{\alpha+}^{(0)L} + g\,\boldsymbol{t}_{\alpha+}^{(1)L} \\ \boldsymbol{t}_{\alpha-}^{(0)L} + g\,\boldsymbol{t}_{\alpha-}^{(1)L} \end{pmatrix}, \tag{5.75}$$

and a similar equation holds for $\boldsymbol{T}_\alpha^R$. To leading order in g, the element of $\tilde{\mathscr{P}}$ read

$$\begin{bmatrix} \tilde{\mathscr{P}}_{\alpha+} \\ \tilde{\mathscr{P}}_{\alpha-} \end{bmatrix} = \frac{i}{f_\alpha}\left(\begin{bmatrix} \mu_{\alpha-}^{(0)} & -1 \\ -\mu_{\alpha+}^{(0)} & 1 \end{bmatrix} - \frac{g\gamma V_{2;\alpha\alpha}}{f_\alpha^2}\begin{bmatrix} \lambda_\alpha & -\mu_{\alpha-}^{(0)} \\ -\lambda_\alpha & \mu_{\alpha+}^{(0)} \end{bmatrix}\right)\begin{bmatrix} 0 \\ \mathscr{P}_\alpha \end{bmatrix}$$
$$+ \frac{ig\gamma}{f_\alpha}\sum_{\beta\neq\alpha}\frac{V_{2;\alpha\beta}}{(\lambda_\alpha - \lambda_\beta)}\begin{bmatrix} \lambda_\beta & -\mu_{\alpha+}^{(0)} \\ -\lambda_\beta & \mu_{\alpha-}^{(0)} \end{bmatrix}\begin{bmatrix} 0 \\ \mathscr{P}_\beta \end{bmatrix} + \mathcal{O}(g^2), \tag{5.76}$$

Expanding Eq. (5.74) to leading order in g, we get

$$\chi_{\alpha\pm} = -\frac{1}{\mu_{\alpha\pm}^{(0)}}\left[\tilde{\mathscr{P}}_{\alpha\pm}^{(0)} + g\tilde{\mathscr{P}}_{\alpha\pm}^{(1)} - g\frac{\mu_{\alpha\pm}^{(1)}\tilde{\mathscr{P}}_{\alpha\pm}^{(0)}}{\mu_{\alpha\pm}^{(0)}}\right]\Big(1 - e^{\mu_{\alpha\pm}^{(0)}t}\Big) + g\,t\frac{\mu_{\alpha\pm}^{(1)}\tilde{\mathscr{P}}_{\alpha\pm}^{(0)}}{\mu_{\alpha\pm}^{(0)}}e^{\mu_{\alpha\pm}^{(0)}t} + \mathcal{O}(g^2), \tag{5.77}$$

Finally, we find $\boldsymbol{\xi}$ and $\dot{\boldsymbol{\xi}}$ by calculating $\boldsymbol{T}^R\boldsymbol{\chi}$ to the leading order in g, we get

$$\begin{bmatrix} \xi_\alpha \\ \dot{\xi}_\alpha \end{bmatrix} = \begin{bmatrix} 1 & 1 \\ \mu_{\alpha+}^{(0)} & \mu_{\alpha-}^{(0)} \end{bmatrix}\begin{bmatrix} \chi_{\alpha+} \\ \chi_{\alpha-} \end{bmatrix} - \frac{g\gamma V_{2;\alpha\alpha}}{f_\alpha^2}\begin{bmatrix} \mu_{\alpha+}^{(0)} & \mu_{\alpha-}^{(0)} \\ \lambda_\alpha & \lambda_\alpha \end{bmatrix}\begin{bmatrix} \chi_{\alpha+}^{(0)} \\ \chi_{\alpha-}^{(0)} \end{bmatrix}$$
$$- g\gamma\sum_{\beta\neq\alpha}\frac{V_{2;\alpha\beta}}{\lambda_\alpha - \lambda_\beta}\begin{bmatrix} \mu_{\beta+}^{(0)} & \mu_{\beta-}^{(0)} \\ \mu_{\beta+}^{(0)2} & \mu_{\beta-}^{(0)2} \end{bmatrix}\begin{bmatrix} \chi_{\beta+}^{(0)} \\ \chi_{\beta-}^{(0)} \end{bmatrix} + \mathcal{O}(g^2). \tag{5.78}$$

Eq. (5.72) is obtained from Eqs. (5.77) and (5.78) and applying trigonometric identities. $\blacksquare$

Proposition 5 *For an abrupt power loss, $\boldsymbol{\delta P}(t) = \boldsymbol{\delta P}\,\Theta(t)$ on a single bus labeled b, $\delta P_i = \delta_{ib}\delta P$, and under Assumption 2, the susceptibilities $\alpha_i \equiv \partial\mathcal{M}_b / \partial a_i$ are given by*

$$\alpha_i = -\frac{g\delta P^2}{2\gamma m_b}\left[\sum_{\alpha>1}\frac{u_{\alpha i}^2 u_{\alpha b}^2}{\lambda_\alpha} + \gamma^2 \sum_{\substack{\alpha>1 \\ \beta\neq\alpha}}\frac{u_{\alpha i}\,u_{\alpha b}u_{\beta i}\,u_{\beta b}}{(\lambda_\alpha - \lambda_\beta)^2 - 2\gamma^2(\lambda_\alpha + \lambda_\beta)}\right]. \tag{5.79}$$

Remark 3 *We have found numerically that the second term is generally much smaller than the first one and gives only marginal corrections to our optimized solution.*

Proof: From Eq. (5.72), to first order in g, one has

$$\int_0^\infty \dot{\xi}_\alpha^2(t)\mathrm{d}t = \frac{\mathscr{P}_\alpha^2}{2\gamma\lambda_\alpha}\left(1 - gV_{2;\alpha\alpha}\right) - g\gamma\sum_{\beta\neq\alpha}\frac{V_{2;\alpha\beta}\mathscr{P}_\alpha\mathscr{P}_\beta}{(\lambda_\alpha - \lambda_\beta)^2 - 2\gamma^2(\lambda_\alpha + \lambda_\beta)} + \mathcal{O}(g^2). \tag{5.80}$$

Taking the derivative of Eq. (5.80) with respect to a_i with the definition of $V_{2;\alpha\beta}$ given below Eq. (5.71), and summing over $\alpha > 1$ one obtains Eq. (5.79). ∎

Finally, we briefly comment our mild inhomogeneity assumptions. Inertia and primary control usually roughly scale up with the rated powers of generators [78]. Hence, for generator buses, the assumption that mild inhomogeneities in the damping ratios $\{\gamma_i\}$ should hold and it is commonly used [126, 124, 111]. The assumption that inertia is roughly uniformly distributed in the grid seems to be a stronger assumption as the generator rated powers scale from a few megawatts to more than one gigawatt. Nevertheless, we have obtained preliminary numerical results, not presented in this work, which seem to show that even large inhomogeneities in local inertia $\{m_i\}$ do not significantly differentiate the slow eigenvectors of $\boldsymbol{L_M}$ from those of $\boldsymbol{L}$ as long as they have no spatial correlations. This observation leads us to think that our perturbation theory approach must be valid in real power systems as long as coarse-grained inhomogeneities are mild.

5.5 Optimal placement of inertia and primary control

In general it is not possible to obtain closed-form analytical expressions for the parameters a_i and r_i determining the optimal placement of inertia and primary control. Simple optimization algorithms can however be constructed that determine how to distribute these parameters to minimize $\mathcal{M}_b$. Theorems 1 and 2 give two such algorithms for optimization under the assumption that some mild inhomogeneity is present in the inertia coefficients or in the damping ratios. Additionally, Conjecture 1 proposes an algorithm for optimization under the assumption that both inertia and the damping ratios are mildly inhomogeneous.

Theorem 1 *For an abrupt power loss, under Assumption 1 and with $\boldsymbol{\Gamma} = \gamma\mathbb{1}_N$, the optimal distribution of parameters $\{r_i\}$ that minimizes $\mathcal{M}_b$ is obtained as follows.*

1. *Compute the sensitivities $\rho_i = \partial \mathcal{M}_b / \partial r_i$ from Eq. (5.61)*
2. *Sort the set $\{\rho_i\}_{i=1,\dots N}$ in ascending order*
3. *Set $r_i = 1$ for $i = \{1,\dots,\text{Int}[N/2]\}$ and $r_i = -1$ for $i = \{N - \text{Int}[N/2] + 1,\dots,N\}$*

The optimal placement of inertia and primary control is given by

$$m_i = m + \delta m\, r_i, \quad d_i = \gamma\left(m + \delta m\, r_i\right). \tag{5.81}$$

Proof: With Proposition 3, we get $\partial \mathcal{M}_b / \partial r_i = \rho_i + \mathcal{O}(\mu^2)$. Consequently, to leading order in μ, the problem described in Theorem 1 is equivalent to the following linear programming problem [136]

$$\min_{\{r_i\}} \sum_i \rho_i r_i, \tag{5.82}$$

$$\text{s.t. } |r_i| \leq 1, \tag{5.83}$$

$$\sum_i r_i = 0. \tag{5.84}$$

To solve this problem, we introduce the following Lagrangian function

$$\mathcal{L} = \sum_i \rho_i r_i + \sum_i \varepsilon_i\left(r_i^2 - 1\right) + \varepsilon \sum_i r_i, \tag{5.85}$$

where ε_i and ε are Lagrange multipliers. We get

$$\frac{\partial \mathcal{L}}{\partial r_i} = \rho_i + 2\varepsilon_i r_i + \varepsilon = 0, \; \forall i. \tag{5.86}$$

The solution must satisfy the Karush-Kuhn-Tucker (KKT) conditions [136]. In particular, complementary slackness (CS) condition imposes that either $\varepsilon_i = 0$ or $r_i = \pm 1$, $\forall i$. The choice $\varepsilon_i = 0$ leads generally to a contradiction, so we choose $r_i = \pm 1$. From Eq. (5.86) and dual feasibility condition, one gets

$$\varepsilon_i = -\frac{\varepsilon + \rho_i}{2 r_i} \geq 0. \tag{5.87}$$

Eq. (5.87) imposes that $r_i = -\text{sgn}(\varepsilon + \rho_i)$. To ensures that $\sum_i r_i = 0$ is satisfied, we set ε to minus the median value of $\{\rho_i\}$. When the number of bus N is odd, the r_i corresponding to the median value of $\{\rho_i\}$ is set to zero. ∎

Theorem 2 *For an abrupt power loss, under Assumption 2 and with $\boldsymbol{M} = m\mathbb{1}_N$, the optimal distribution of parameters $\{a_i\}$ that minimizes $\mathcal{M}_b$ is obtained as follows.*

1. *Compute the sensitivities $\alpha_i = \partial \mathcal{M}_b / \partial a_i$ from Eq. (5.79).*
2. *Sort the set $\{\alpha_i\}$ in ascending order,*
3. *Set $a_i = 1$ for $i = \{1,\dots,\text{Int}[N/2]\}$ and $a_i = -1$ for $i = \{N - \text{Int}[N/2] + 1,\dots,N\}$*

The optimal placement of primary control is given by

$$d_i = m(\gamma + \delta\gamma\, a_i). \tag{5.88}$$

Proof: With Proposition 5 and $\boldsymbol{M} = m\mathbb{1}_N$, we get Eq. (5.79). The proof is the same as the one for Theorem 1, but with $\{\alpha_i\}$ instead of $\{\rho_i\}$. ∎

We next conjecture an algorithmic combined linear optimization treating simultaneously Assumptions 1 and 2. The difficulty is that for fixed total inertia and damping, one must have $\sum_i m_i = N\,m$, $\sum_i d_i = N\,d$. From Eq. (5.54), the second condition requires $\sum_i a_i r_i = 0$. This is a quadratic, nonconvex constraint, which makes the problem nontrivial to solve. The following conjecture presents an algorithm that starts from the distribution $\{a_i\}$ and $\{r_i\}$ from Theorems 1 and 2 and orthogonalizes them while trying to minimize the related increase in $\mathcal{M}_b$.

Conjecture 1 (Combined linear optimization) *For an abrupt power loss, under Assumptions 1 and 2, the optimal placement of a fixed total amount of inertia $\sum_i m_i = mN$ and primary control $\sum_i d_i = dN$ that minimize $\mathcal{M}_b$ is obtained as follows.*

1. *Compute the parameters r_i and a_i from Theorems 1 and 2.*
   (a) *If N is odd, align the zeros of $\{r_i\}$ and $\{a_i\}$. Let i_{r0} and i_{a0} be the indexes of these zeros. Their new common index is $i_{\text{align}} = \underset{i}{\operatorname{argmin}}\big(r_i \rho_{i_{r0}} + a_i \alpha_{i_{a0}} - r_i \rho_i - a_i \alpha_i\big)$. Interchange the parameter values $r_{i_{r0}} \leftrightarrow r_{i_{\text{align}}}$ and $a_{i_{r0}} \leftrightarrow a_{i_{\text{align}}}$.*
   (b) *If N is even, do nothing*
2. *If $n \equiv \sum_i r_i a_i = 0$, the optimization is done.*
3. *Find the set $\mathscr{I} = \{i\,|\,\text{sgn}(r_i a_i) = \text{sgn}(n)\}$. To reach $\sum_i r_i a_i \to 0$, our strategy is to set to zero some elements of $\mathscr{I}$. Since however $\sum_i a_i = \sum_i r_i = 0$ must be conserved, this must be accompanied by a simultaneous change of some other parameter.*
4. *Find the pair $(a_{i1}, a_{i2} = -a_{i1})$ or $(r_{i1}, r_{i2} = -r_{i1}) \in \mathscr{I} \times \mathscr{I}$ which, when sent to $(0,0)$, induce the smallest increase of the objective function $\mathcal{M}_b$. Send it to $(0,0)$. Because the pair has opposite sign, this does not affect the condition $\sum_i a_i = \sum_i r_i = 0$.*
5. *go to step #2.*

It is not at all guaranteed that the algorithm presented in Conjecture 1 is optimal, however, numerical results to be presented below indicate that it works well.

The optimization considered so far focused on a single fault on bus labeled *#b*. We are interested, however, in finding the optimal distribution of inertia and/or primary control for all possible faults. To that end we introduce the following global vulnerability measure

$$\mathcal{V} = \sum_b \eta_b\, \mathcal{M}_b(\delta P_b), \tag{5.89}$$

where the sum runs over all generator buses. The vulnerability measure $\mathcal{V}$ gives a weighted

average over all possible fault positions, with the weight η_b accounting for the probability that a fault occurs at b and δP_b accounting for its potential intensity as given, e.g. by the rated power of the generator at the bus #b.

For equiprobable fault locations and for the same power loss everywhere, $\eta_b \equiv 1$. From Eqs. (5.89) and (5.61), it is straightforward to see that $\partial \mathcal{V}/\partial r_i = 0 + \mathcal{O}(\mu^2)$. Therefore, to leading order, there is no benefit in scaling up the inertia anywhere. On the other hand, from Eq. (5.79) and with $M = m\mathbb{1}_N$, we get

$$
\frac{\partial \mathcal{V}}{\partial a_i} = -\frac{g\delta P^2}{2\gamma m} \sum_{\alpha>1} \frac{u_{\alpha i}^{(0)2}}{\lambda_\alpha^{(0)}} + \mathcal{O}(g^2).
\tag{5.90}
$$

The corresponding optimal placement of primary control can be obtained with Theorem 2, from which we observe that the damping ratios are increased for the buses which have large squared components $u_{\alpha i}^{(0)2}$ for the slow modes of L. These modes are displayed in Fig 5.1. One concludes that, with a non-weigthed vulnerability measure, $\eta_b \equiv 1$ in Eq. (5.89), a homogeneous inertia is a local optimum for $\mathcal{V}$, for which damping parameters need to be increased primarily on peripheral buses.

5.6 Numerical investigations

We illustrate our main results on a model of the synchronous power grid of continental Europe. The network has 3809 nodes, among them 618 generators, connected through 4944 lines. For details of the model and its construction we refer the reader to [131, 69]. To connect to the theory presented above, we remove inertialess buses through a Kron reduction [137] and uniformize the distribution of inertia to $m_i = 29.22\text{MWs}^2$, and primary control $d_i = 12.25\text{MWs}$. This guarantees that the total amounts of inertia and primary control are kept at their initial levels.

Fig. 5.3 (a) shows the value of $\mathcal{M}_b^{(0)}$ calculated for each possible fault locations. Buses in the periphery of the grid tend to have larger values of $\mathcal{M}_b^{(0)}$ than those in the geometric center of Europe, which more or less coincides with center of the continental grid in terms of resistance centrality. For the sake of clarity, we average local frequencies ω_i into areal frequencies $\overline{\omega}_\alpha$ as follows

$$
\overline{\omega}_\alpha = \frac{\sum_{i\in S_j} m_i \omega_i(t)}{\sum_{i\in S_j} m_i}.
\tag{5.91}
$$

A map of the areas as well as the procedure we used to obtain them are presented in Section 5.2.1. Panels (b)-(d) display the evolution of areal frequencies for three contingencies which are chosen so that they correspond to a small, an intermediate and a large value of $\mathcal{M}_b$. Despite of the fact that the lost generation is 500MW in each case, the disturbance magnitude significantly differs from a fault location to another. In Fig. 5.3 (b), the areal frequencies

smoothly decrease to the post-fault frequency $\omega_{\mathrm{pf}} = \delta P/(dN)$. In Fig. 5.3 (c), some areal frequencies drop below the post-fault frequency. The system is more disturbed than in the previous case. In Fig. 5.3 (d), the area where the fault occurs is subject to a drastic drop of frequency which dives significantly below the post-fault frequency. Other areal frequencies encounter disturbances comparable to those in Fig. 5.3 (b). We conclude that the faults exciting the slowest eigenmodes of the network Laplacian are those disturbing the grid the most.
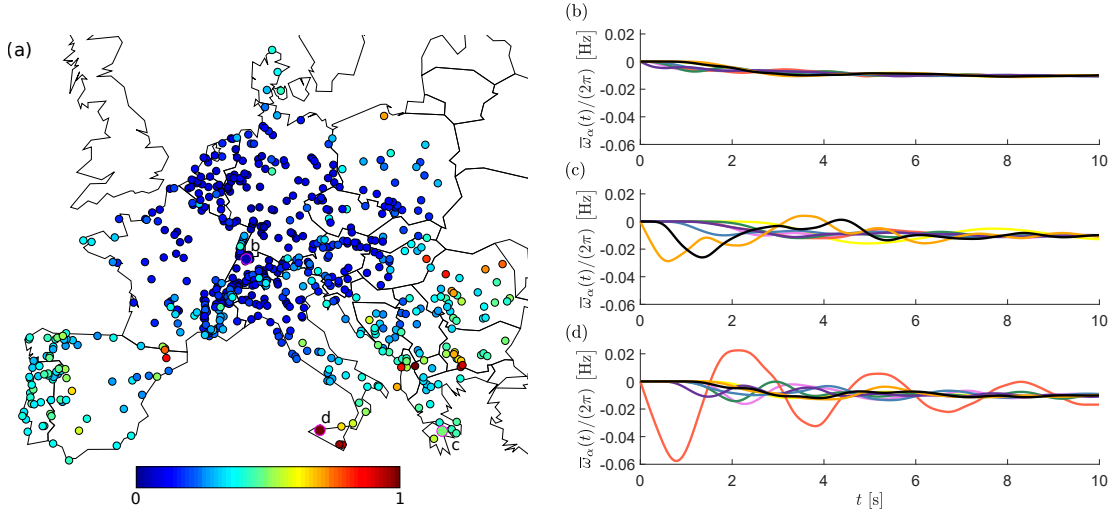

Figure 5.3 − *(a) Performance measure $\mathcal{M}_b^{(0)}$ for each possible fault location in continental Europe when inertia and primary control are uniformly distributed in the grid. (b)-(d) Areal frequencies $\overline{\omega}_\alpha$ after the loss of 500[MW] for three fault locations which are highlighted in panel (a). Areas are presented in Fig. 5.2.*

Fig. 5.4 shows the optimal placement of inertia and primary control for 4 different fault locations obtained with Theorem 1 and 2. The upper row of Fig. 5.4 shows the optimal placement of inertia for four different fault locations. The local increases of inertia ($r_i = 1$) are concentrated in the vicinity of the fault, they usually form a connected area. One better understands this result by reformulating Eq. (5.61), with Eqs. (5.51)-(5.29), in terms of resistance distances, as

$$\rho_i \propto \left(1 - N^{-1}\right)\Omega_{ib} - N^{-1} \sum_{j \neq b} \Omega_{ij}, \tag{5.92}$$

For large system, Eq. (5.92) shows that the first-order sensitivity ρ_i depends mainly on the resistance distance Ω_{ib} between the fault location and the bus $\#i$. This is particularly noticeable by comparing the blue areas in the upper row of Fig. 5.4 with the areas we obtain by minimal resistance distance clustering displayed in Fig. 5.2. The bottom row of Fig. 5.4 shows the optimal placement of primary control for the same faults. The increases in primary control ($a_i = 1$) are mostly in the periphery of the grid. Even central faults have most of their positive abatement parameters on the periphery. We observe that these two optimizations lead to significantly different distributions of these two resources.
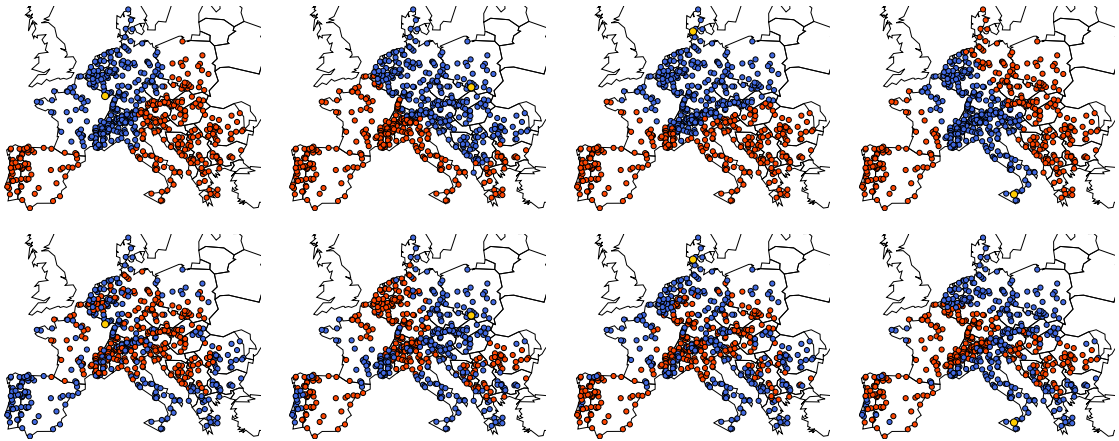
Figure 5.4 – *Optimal parameters $\{r_i\}$ (top) and parameters $\{a_i\}$ (down) for four fault locations: $a_i, r_i = -1, 1$ are displayed in red and blue respectively. The locations of the fault are displayed in yellow.*

Fig. 5.5 (a) and (b) show the $\{r_i\}$ and $\{a_i\}$ parameters obtained with Conjecture 1 for a fault located in Greece. We observe that $\{r_i\}$ and $\{a_i\}$ were already mostly orthogonal and that minor adjustments guarantee that the total primary control is conserved. Fig. 5.5 (c) shows the areal frequencies of the two most disturbed areas after this fault. The disturbance is the highest for homogeneous inertia and primary control. With solely optimized $\{r_i\}$ parameters, we observe that the disturbance is lowered and delayed. With solely optimized $\{a_i\}$, the disturbance is more strongly damped. Finally, for optimal inertia and primary control based on the jointly optimized $\{r_i\}$ and $\{a_i\}$ parameters, the disturbance is delayed and strongly damped, leading to the strongest mitigation of the disturbance. We conclude that Conjecture 1 seems to offer the best distributions of inertia and primary control in the vicinity of the homogeneous case.

Fig. 5.6 (a) and (b) show the optimal inertia and primary control distribution that minimize $\mathcal{V}$ of Eq. (5.89) with constant weights, $\eta_b = 1$. With that choice of global vulnerability measure, a homogeneous distribution of inertia is a local optimum. This directly follows from Eq. (5.61), with $\sum_b u_{\alpha b}^{(0)} = 0$, $\forall \alpha > 1$. Primary control on the other hand needs to be distributed primarily on peripheral buses. Fig. 5.6 (c) furthermore shows that the minimization of $\mathcal{V}$ significantly reduces the performance measure $\mathcal{M}_b$ for fault location b where it is largest, i.e. for faults leading to the largest transient response, while not affecting much $\mathcal{M}_b$ where it is small. The optimal placement of primary control displayed in Fig. 5.6 (b) decreases $\mathcal{V}$ by more than 12% with respect to the homogeneous case.
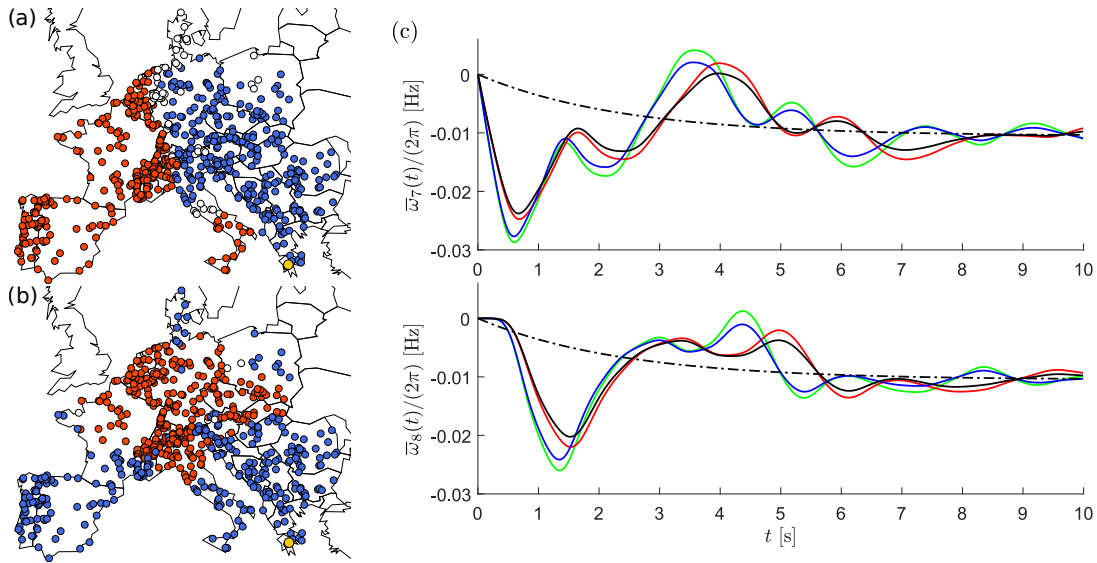
Figure 5.5 – *Combined optimization: (a) optimal $\{r_i\}$ parameters (b) Optimal $\{a_i\}$ parameters. $r_i, a_i = -1, 0, 1$ are displayed in red, white and blue respectively. The location of the fault is displayed in yellow. (c) Evolution of areal frequencies $\overline{\omega}_7$ and $\overline{\omega}_8$ for a 500[MW] fault in Greece: with inertia and primary control uniformly distributed (green), with solely optimized $\{r_i\}$ parameters (red), with solely optimized $\{a_i\}$ parameters (blue) and with jointly optimized $\{r_i\}$ and $\{a_i\}$ parameters (black). We use $\mu = g = 0.3$. Areas are displayed in Fig. 5.2.*
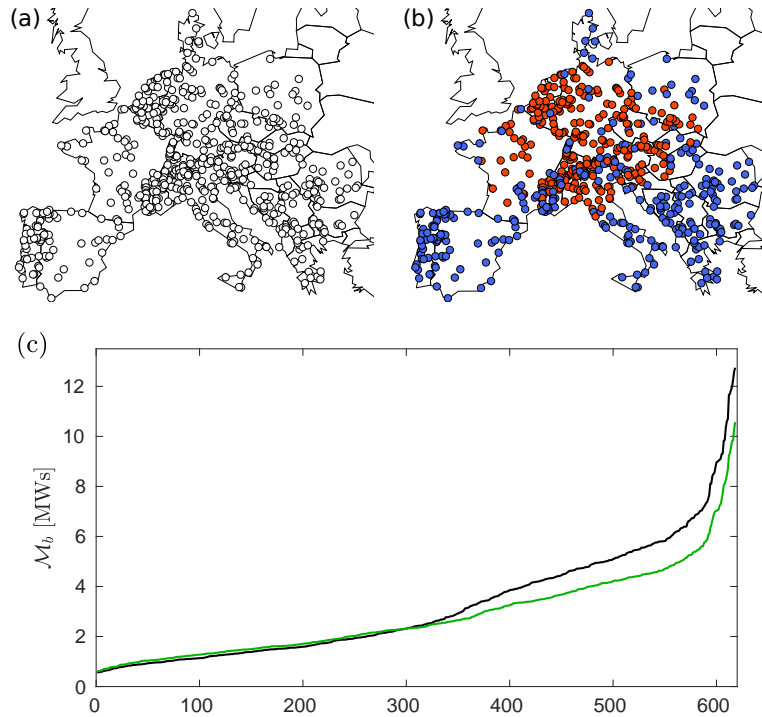
Figure 5.6 – *Deviation from homogeneous inertia (a) and primary control (b) following the minimization of $\mathcal{V}$ in (5.89) with homogeneous weight $\eta_b \equiv 1$. $r_i = -1, 0, 1$ (left) and $a_i = -1, 0, 1$ (right) are displayed in red, white and blue respectively. (c) Vulnerability $\mathcal{M}_b$ vs. fault location (in increasing order of $\mathcal{M}_b$) for the homogeneous model (black) and the optimized model corresponding to panels (a) and (b) (green).*

5.7 Conclusion

In this chapter we investigated the optimal placement of inertia and primary control in transmission grids to maximize their resilience against localized contingencies. We introduced a mathematical $\mathcal{L}_2-$norm performance measure based on local frequency deviations to quantify the magnitudes of disturbances. We showed that the power system dynamics is described by closed-form expressions only under the assumption of uniform damping ratios. This assumption strongly limits the possible analytical investigations of optimal placement of inertia and primary control. We circumvent this limitation by applying perturbation theory to find approximate expressions of our measure in the cases where some mild inhomogeneities are present in inertia and primary control distributions. We used these expressions to calculate the sensitivities of our measure in changes in inertia and primary control and we built optimal placement algorithms on them.

In this chapter, we found that:

- When inertia and primary control are uniformly distributed, the faults exciting the slowest eigenmodes of the network Laplacian have the largest values of our disturbance measure.
- For a given fault location, it is optimal to have inertia in its vicinity and primary control on the slowest eigenmodes which are excited by this fault.
- When the vulnerability of the whole grid is assessed with equiprobable fault locations, uniform distribution of inertia is optimal and the primary control is best placed in the periphery of the grid.

Conclusion and perspectives

In this work, we presented different aspects of the energy transition which consists in the substitution of the conventional CO_2 emitting energy sources by new renewable ones. The latter differ from the former by the following aspects: they are distributed, non-dispatchable, fluctuating and inertialess and they have negligible marginal costs. We investigated the impact of the energy transition on the electricity sector in Europe.

In Chapter 2, we developed a dispatch algorithm on an aggregated model of the pan-European power grid with which we studied the future European productions. Our results shows that more flexibility is asked to conventional generators as the penetration of new RES increases. Our investigations suggest that no technical constraint should hinder the energy transition in Europe during the next decade. Existing infrastructures seem to be able to cope with a relatively high penetration of new RES in the European energy mix. We showed that the proposed enhancements of the Swiss transmission network seem to considerably reduce the congestion in the grid. We also paid a special attention to the hydroelectric producers and observed that they should not suffer form generation restriction due to grid congestion. Finally, our results show that increased international power exchanges and existing PS hydroelectricity are able to absorb, to a large extend, the variations of new RES productions.

In Chapter 3, we investigated the effects of new RES on electricity prices. We explained that, due to their negligible marginal cost and their lack of dispatchability, they can be seen as a reduction of the load for electricity pricing. A share of the dispatchable productions, called must-run, acts as a non-dispatchable source for economic reasons. We showed that, in most European countries, the day-ahead electricity price is strongly correlated with residual load, which is obtained by subtracting the new RES and must-run productions from the load. From this observation, we built an effective price based solely on the residual load. With this physico-economic indicator we investigated the revenues of different electricity producers. Our results shows that new RES tend to drag electricity prices down, PV particularly decreases the volatility of electricity prices. They also suggest that an insufficient withdrawal of must-run productions is one of the main reasons for the current low revenues of flexible sources in Europe.

In Chapter 4, we examined the propagation of disturbances in large transmission grids. We developed a dynamical model of the continental European transmission grid. We observed that the magnitude of the disturbance following an abrupt power loss depends on the fault

location. We were able to relate this magnitude to the excitation of the slowest eigenmodes of the network Laplacian. Our results suggests that they are stronger when the faults excites the slowest eigenmodes of the system in particular the Fielder mode. We found that inertia reduction on the Fiedler area leads to an amplified RoCoF response, while reducing the inertia on non-Fiedler area has a much weaker effect, with only a moderate increase of local RoCoFs. Our results show that power systems are more resilient when more inertia is present in their "Fiedler areas".

In Chapter 5, we sought the optimal placement of inertia and primary control in transmission grids to maximize their resilience against localized contingencies. We showed that when inertia and primary control are uniformly distributed, the faults exciting the slowest eigenmodes of the network Laplacian have the largest values of our disturbance measure, which corroborates our findings in Chapter 4. We used perturbation theory to obtain the sensitivities of a disturbance measure to the local changes in inertia and primary control distributions. We derived algorithms for optimal placement of inertia and primary control when some mild inhomogeneities are present in their distributions. For a given fault location, it is optimal to have inertia in its vicinity and primary control on the slowest eigenmodes which are excited by this fault. Our results shows that, when the vulnerability of the whole grid is taken into account, a uniform distribution of inertia is optimal and the primary control is best placed in the periphery of the grid.

As a extension to the present work, we will investigate future power dispatches in Europe when new RES become prominent in the energy mix. In particular there is a trade-off between the requirement of new storage facilities and the acceptance of new RES curtailment. The surplus power can be used to produce hydrogen or methane through power-to-gas technologies [138].

We can probably enhance our electricity price model by incorporating the CO_2 taxes which are one of the leverages that policymakers have to drive the energy transition in Europe. It would the investigations more realistic on longer time scales. Another interesting topic would be to study the evolution of the revenues of new RES. They have a levelized cost of energy (LCOE) comparable to those of conventional sources. The LCOE is obtained by dividing the total expenditures (construction, fuel, maintenance, . . .) of a generator by its total production over its lifetime. When new RES become prominent in the European mix, they might drive their average revenue below their LCOE due to their negligible marginal cost.

We will also continue our investigation on disturbances in power systems, in particular on the optimal placement of inertia and primary control. The first idea that comes to the mind is to extent our perturbation theory to the second order corrections. This would give us more refined optimal distributions of inertia and primary control.

Acknowledgements

I would like to thank Philippe Jacquod and Frédéric Mila for giving me the opportunity to pursue a PhD in an interesting and inspiring research area.

I am grateful to Michael (Misha) Chertkov, Florian Dörfler and Stefan Ketteman for their useful comments and remarks on the manuscript.

To Robin, Melvyn, Tomasso, David T., David M., Didier, Frédéric, Pablo, Lucas, Jessen, Vincent, Sébastien, Pierre-André, Gilbert Ma., Gilbert Mo., Véronique, Alain, Carmine, Darko and the other colleagues of the HES-SO Valais/Wallis: it was a pleasure to share many activities with you, like debating on some complex problems, exploring Brussels, gossiping at coffee breaks, climbing and mountaineering, drinking beers in pubs, . . .

I apologize to all my old friends for not having spent enough time with them lately.

Many thanks to my family who gave me continuous support and encouragement during the last 4 years.

Sion, February 2019   Laurent

Bibliography

[1] J. Oerlemans, "Quantifying global warming from the retreat of glaciers," *Science*, vol. 264, no. 5156, pp. 243–245, 1994.

[2] J. Cook, D. Nuccitelli, S. A. Green, M. Richardson, B. Winkler, R. Painting, R. Way, P. Jacobs, and A. Skuce, "Quantifying the consensus on anthropogenic global warming in the scientific literature," *Environmental research letters*, vol. 8, no. 2, p. 024024, 2013.

[3] A. Einstein, "On the method of theoretical physics," *Philosophy of science*, vol. 1, no. 2, pp. 163–169, 1934.

[4] Swiss Federal Office of Electricity (BFE), "Schweizerische Elektrizitätsstatistik 2017." http://www.bfe.admin.ch/php/modules/publikationen/stream.php?extlang= fr&name=fr_172350757.pdf, 2018.

[5] J. J. Grainger, W. D. Stevenson, and G. W. Chang, *Power system analysis*, vol. 621. McGraw-Hill New York, 1994.

[6] A. Bergen and V. Vittal, *Power Systems Analysis.* Pearson/Prentice Hall, second ed., 2000.

[7] RTE, "Static grid model." https://clients.rte-france.com/htm/fr/vie/telecharge/Static_ Grid_Model_RTE_CWE_project_publication.xlsx, 2015.

[8] A. Gómez-Expósito, A. J. Conejo, and C. Cañizares, *Electric energy systems: analysis and operation.* Boca Raton, FL: CRC Press, 2008.

[9] L. Pagnier and P. Jacquod, "A predictive pan-european economic and production dispatch model for the energy transition in the electricity sector," in *PowerTech, 2017 IEEE Manchester*, IEEE, 2017.

[10] L. Pagnier and P. Jacquod, "Swissgrid's strategic grid 2025 : an independent analysis." https://www.researchgate.net/publication/322790410_Swissgrid's_strategic_grid_ 2025_an_independent_analysis, 2018.

[11] N. Pinto Marinho, *Réduction d'un modèle de système électrique pour des études technico-économiques.* PhD thesis, Paris Saclay, 2018.

Bibliography

[12] C. Grudzien, D. Deka, M. Chertkov, and S. N. Backhaus, "Structure-and physics-preserving reductions of power grid models," *Multiscale Modeling & Simulation*, vol. 16, no. 4, pp. 1916–1947, 2018.

[13] C. Huo and E. Cotilla-Sanchez, "A power-balanced clustering algorithm to improve electrical infrastructure resiliency," in *2018 Power Systems Computation Conference (PSCC)*, pp. 1–8, IEEE, 2018.

[14] ENTSO-E, "ENTSO-E Transparency platform." https://transparency.entsoe.eu/, 2015.

[15] J. B. Ward, "Equivalent circuits for power-flow studies," *Electrical Engineering*, vol. 68, no. 9, pp. 794–794, 1949.

[16] W. F. Tinney and J. M. Bright, "Adaptive reductions for power flow equivalents," *IEEE transactions on power systems*, vol. 2, no. 2, pp. 351–359, 1987.

[17] A. Papaemmanouil and G. Andersson, "On the reduction of large power system models for power market simulations," in *17th Power Systems Computation Conference (PSCC)*, pp. 1308–1313, 2011.

[18] D. Shi and D. J. Tylavsky, "A novel bus-aggregation-based structure-preserving power system equivalent," *IEEE Transactions on Power Systems*, vol. 30, no. 4, pp. 1977–1986, 2015.

[19] ENTSO-E, "Scenario Outlook & Adequacy Forecast." https://www.entsoe.eu/map/Pages/default.aspx, 2015.

[20] ENTSO-E, "ENTSO-E TYNDP Dataset." http://tyndp.entsoe.eu/, 2016.

[21] Swiss Federal Office of Energy (BFE), "Weekly report on water level of reservoirs." http://www.bfe.admin.ch/themen/00526/00541/00542/00630/index.html?lang=en&dossier_id=00766, 2016.

[22] S. Rehman, L. M. Al-Hadhrami, and M. M. Alam, "Pumped hydro energy storage system: A technological review," *Renewable and Sustainable Energy Reviews*, vol. 44, pp. 586–598, 2015.

[23] M. Guittet, M. Capezzali, L. Gaudard, F. Romerio, F. Vuille, and F. Avellan, "Study of the drivers and asset management of pumped-storage power plants historical and geographical perspective," *Energy*, vol. 111, pp. 560–579, 2016.

[24] D. P. Schlachtberger, T. Brown, S. Schramm, and M. Greiner, "The benefits of cooperation in a highly renewable european electricity network," *Energy*, vol. 134, pp. 469–481, 2017.

[25] G. Czisch, *Szenarien zur zukünftigen Stromversorgung: kostenoptimierte Variationen zur Versorgung Europas und seiner Nachbarn mit Strom aus erneuerbaren Energien*. PhD thesis, Universität Kassel, 2005.

[26] K. Schaber, F. Steinke, and T. Hamacher, "Transmission grid extensions for the integration of variable renewable energies in europe: Who benefits where?," *Energy Policy*, vol. 43, pp. 123–135, 2012.

[27] F. Comaty, A. Ulbig, and G. Andersson, "Ist das geplante Stromsystem der Schweiz für die Umsetzung der Energiestrategie 2050 aus technischer Sicht geeignet?," 2014.

[28] R. A. Rodriguez, S. Becker, and M. Greiner, "Cost-optimal design of a simplified, highly renewable pan-european electricity system," *Energy*, vol. 83, pp. 658–668, 2015.

[29] J. Schwippe, A. Seack, and C. Rehtanz, "Pan-european market and network simulation model," in *PowerTech (POWERTECH), 2013 IEEE Grenoble*, pp. 1–6, IEEE, 2013.

[30] J. Nocedal and S. J. Wright, *Numerical optimization.* Springer, 2nd ed., 2006.

[31] Gurobi Optimization, LLC, "Gurobi optimizer reference manual," 2018.

[32] L. Hirth, "The market value of variable renewables: The effect of solar wind power variability on their relative price," *Energy Economics*, vol. 38, pp. 218 – 236, 2013.

[33] L. Hirth, "The european electricity market model emmamodel documentation." https://neon-energie.de/emma-documentation.pdf, 2017.

[34] R. Zimmerman, C. Murillo-Sánchez, and R. T. Thomas, "Matpower: Steady-state operations, planning and analysis tools for power systems research and education," *IEEE Trans. on Power Systems*, vol. 26, pp. 12–19, 2011.

[35] C. Josz, S. Fliscounakis, J. Maeght, and P. Panciatici, "AC power flow data in MATPOWER and QCQP format: iTesla, RTE snapshots, and PEGASE," *arXiv:1603.01533*, 2016.

[36] S. An, Q. Li, and T. W. Gedra, "Natural gas and electricity optimal power flow," in *2003 IEEE PES Transmission and Distribution Conference and Exposition (IEEE Cat. No. 03CH37495)*, vol. 1, pp. 138–143, IEEE, 2003.

[37] J. Hörsch, F. Hofmann, D. Schlachberger, and T. Brown, "Pypsa-eur: An open optimisation model of the european transmission system," *Energy Strategy Reviews*, vol. 22, pp. 207–215, 2018.

[38] M. Emery, "Le réseau stratégique 2025 de swissgrid," *Bulletin SEV/VSE*, 2016.

[39] Swiss Federal Office of Meteorology and Climatology (MeteoSwiss), "archive data of meteoswiss." https://gate.meteoswiss.ch/idaweb/.

[40] B. von Kupsch, "Bericht zum Strategischen Netz 2025." https://www.swissgrid.ch/dam/swissgrid/projects/strategic-grid/sg2025-technical-report-de.pdf, 2015.

[41] Operation Simulation Associates, "Powrsym4 model." http://www.powrsym.com/.

[42] Siemens, "Power system simulator for engineering (PSS/E)." https://new.siemens.com/global/en/products/energy/services/transmission-distribution-smart-grid/consulting-and-planning/pss-software/pss-e.html.

[43] D. P. Schlachtberger, S. Becker, S. Schramm, and M. Greiner, "Backup flexibility classes in emerging large-scale renewable electricity systems," *Energy Conversion and Management*, vol. 125, pp. 336–346, 2016.

[44] L. Pagnier and P. Jacquod, "How fast can one overcome the paradox of the energy transition? a physico-economic model for the european power grid," *Energy*, vol. 157, pp. 550–560, 2018.

[45] S. Clò, A. Cataldi, and P. Zoppoli, "The merit-order effect in the Italian power market: The impact of solar and wind generation on national wholesale electricity prices," *Energy Policy*, vol. 77, pp. 79–88, 2015.

[46] F. Paraschiv, D. Erni, and R. Pietsch, "The impact of renewable energies on EEX day-ahead electricity prices," *Energy Policy*, vol. 73, pp. 196–210, 2014.

[47] J. Cludius, H. Hermann, F. C. Matthes, and V. Graichen, "The merit order effect of wind and photovoltaic electricity generation in Germany 2008–2016: Estimation and distributional implications," *Energy Economics*, vol. 44, pp. 302–313, 2014.

[48] F. Sensfuss, M. Ragwitz, and M. Genoese, "The merit-order effect: A detailed analysis of the price effect of renewable electricity generation on spot market prices in Germany," *Energy policy*, vol. 36, pp. 3086–3094, 2008.

[49] R. Haas, G. Lettner, H. Auer, and D. Neven, "The looming revolution: how photovoltaics will change electricity markets in europe fundamentally," *Energy*, vol. 57, pp. 38–43, 2013.

[50] H. Auer and R. Haas, "On integrating large shares of variable renewables into the electricity system," *Energy*, vol. 115, pp. 1592–1601, 2016.

[51] EPEX SPOT, "Annual report." https://www.epexspot.com/en/extras/download-center/activity_reports, 2015.

[52] OMIE, "Main results of the electricity market." http://www.omie.es/files/mercado_electrico_ing.diptico_web_pdf.pdf, 2015.

[53] OTE, "Annual report." http://www.ote-cr.cz/about-ote/annual-reports, 2015.

[54] NordPool, "Annual report." http://www.nordpoolspot.com/About-us/Annual-report/, 2015.

[55] P. Denholm and M. Hand, "Grid flexibility and storage required to achieve very high penetration of variable renewable electricity," *Energy Policy*, vol. 39, pp. 1817–1830, 2011.

[56] W.-P. Schill, "Residual load, renewable surplus generation and storage requirements in germany," *Energy Policy*, vol. 73, pp. 65–79, 2014.

[57] L. Saarinen, N. Dahlbäck, and U. Lundin, "Power system flexibility need induced by wind and solar power intermittency on time scales of 1–14 days," *Renewable Energy*, vol. 83, pp. 339–344, 2015.

[58] M. Nicolosi, "Wind power integration and power system flexibility – An empirical analysis of extreme events in Germany under the new negative price regime," *Energy Policy*, vol. 38, pp. 7257–7268, 2010.

[59] F. Ueckerdt, R. Brecha, G. Luderer, P. Sullivan, E. Schmid, N. Bauer, D. Böttger, and R. Pietzcker, "Representing power sector variability and the integration of variable renewables in long-term energy-economy models using residual load duration curves," *Energy*, vol. 90, pp. 1799–1814, 2015.

[60] G. Schweiger, J. Rantzer, K. Ericsson, and P. Leuenburg, "The potential of power-to-heat in Swedish district heating systems," *Energy*, vol. xxx, pp. 1–9, 2017.

[61] M. Nicolosi, *The economics of renewable electricity market integration. An empirical and model-based analysis of regulatory frameworks and their impacts on the power market.* PhD thesis, Universität zu Köln, 2012.

[62] S. von Roon and M. Huber, "Modeling spot market pricing with the residual load," tech. rep., Forschungsstelle für Energiewirtschaft, 2010.

[63] CREG, "The price spikes observed on the Belgian day-ahead spot exchange Belpex on 22 September and 16 October 2015," tech. rep., Commission for electricity and gas regulation, 2015.

[64] T. M. Christensen, A. S. Hurn, and K. A. Lindsay, "Forecasting spikes in electricity prices," *International Journal of Forecasting*, vol. 28, pp. 400–411, 2012.

[65] ENTSO-E, "TYNDP 2016 Scenario Development Report." http://tyndp.entsoe.eu/.

[66] G. Thürler, "Statistik der Wasserkraftanlagen der Schweiz." http://www.bfe.admin.ch/themen/00490/00491/index.html?lang=de&dossier_id=01049, 2014.

[67] H. C. Gils, "Economic potential for future demand response in germany–modeling approach and case study," *Applied Energy*, vol. 162, pp. 401–415, 2016.

[68] A. B. Birchfield, T. Xu, K. M. Gegner, K. S. Shetye, and T. J. Overbye, "Grid structural characteristics as validation criteria for synthetic networks," *IEEE Transactions on power systems*, vol. 32, no. 4, pp. 3258–3265, 2017.

[69] L. Pagnier and P. Jacquod, "Disturbance propagation, inertia location and slow modes in large-scale high voltage power grids," *arXiv:1810.04982*, 2018.

[70] Q. Zhou and J. W. Bialek, "Approximate model of european interconnected system as a benchmark system to study effects of cross-border trades," *IEEE Transactions on power systems*, vol. 20, no. 2, pp. 782–788, 2005.

[71] N. Hutcheon and J. W. Bialek, "Updated and validated power flow model of the main continental european transmission network," in *PowerTech, 2013 IEEE Grenoble*, IEEE, 2013.

[72] F. U. Leuthold, H. Weigt, and C. Von Hirschhausen, "A large-scale spatial optimization model of the european electricity market," *Networks and spatial economics*, vol. 12, no. 1, pp. 75–107, 2012.

[73] D. Hewes, S. Altschaeffl, I. Boiarchuk, and R. Witzmann, "Development of a dynamic model of the european transmission system using publicly available data," in *Energy Conference (ENERGYCON), 2016 IEEE International*, pp. 1–6, IEEE, 2016.

[74] B. Wiegmans, "GridKit extract of ENTSO-E interactive map." https://doi.org/10.5281/zenodo.55853, 2016.

[75] Siemens, "Power engineering guide." http://siemens.com/energy/peg, 2014.

[76] Geonames, "Cites1000 data base." http://download.geonames.org/export/.

[77] Global energy observatory, "GEO Power plants database." http://globalenergyobservatory.org/.

[78] J. Machowski, J. Bialek, and J. R. Bumby, *Power system dynamics: stability and control.* John Wiley & Sons, 2 ed., 2008.

[79] E. Kimbark, *Synchronous machines.* Power System Stability, Wiley, 1956.

[80] P. Kundur, *Power system stability and control.* McGraw-hill New York, 1994.

[81] A. R. Bergen and D. J. Hill, "A structure preserving model for power system stability analysis," *IEEE Transactions on Power Apparatus and Systems*, vol. 10, no. 1, pp. 25–35, 1981.

[82] D. Hill and A. Bergen, "Stability analysis of multimachine power networks with linear frequency dependent loads," *IEEE Transactions on Circuits and Systems*, vol. 29, no. 12, pp. 840–848, 1982.

[83] E. Welfonder, H. Weber, and B. Hall, "Investigations of the frequency and voltage dependence of load part systems using a digital self-acting measuring and identification system," *IEEE Transactions on Power Systems*, vol. 4, no. 1, pp. 19–25, 1989.

[84] J. O'Sullivan and M. O'Malley, "Identification and validation of dynamic global load model parameters for use in power system frequency simulations," *IEEE Transactions on Power Systems*, vol. 11, no. 2, pp. 851–857, 1996.

[85] H. Bevrani, *Robust power system frequency control.* New York: Springer, 2nd ed., 2014.

[86] E. Hairer and G. Wanner, "Stiff differential equations solved by radau methods," *Journal of Computational and Applied Mathematics*, vol. 111, no. 1-2, pp. 93–111, 1999.

[87] F. Milano, F. Dörfler, G. Hug, D. J. Hill, and G. Verbič, "Foundations and challenges of low-inertia systems," in *Power Systems Computation Conference (PSCC), 2018*, IEEE, 2018.

[88] N. Jenkins, R. Allan, P. Crossley, D. Kirschen, and G. Strbac, *Embedded generation.* The Institution of Engineering and Technology, 2000.

[89] Energy Networks Association, "Engineering Recommendation G59," 2017.

[90] J. H. Chow, *Power system coherency and model reduction.* New York: Springer, 2013.

[91] E. Mallada and A. Tang, "Improving damping of power networks: Power scheduling and impedance adaptation," in *2011 50th IEEE Conference on Decision and Control and European Control Conference*, pp. 7729–7734, IEEE, 2011.

[92] A. E. Motter, S. A. Myers, M. Anghel, and T. Nishikawa, "Spontaneous synchrony in power-grid networks," *Nature Physics*, vol. 9, no. 3, p. 191, 2013.

[93] T. Coletta and P. Jacquod, "Linear stability and the braess paradox in coupled-oscillator networks and electric power grids," *Physical Review E*, vol. 93, no. 3, p. 032222, 2016.

[94] B. Slininger, "Fiedlers theory of spectral graph partitioning," 2013.

[95] L. Ding, Z. Ma, P. Wall, and V. Terzija, "Graph spectra based controlled islanding for low inertia power systems," *IEEE Transactions on Power Delivery*, vol. 32, no. 1, pp. 302–309, 2017.

[96] L. A. Torres-Sánchez, G. T. F. de Abreu, and S. Kettemann, "Analysis of the dynamics and topology dependencies of small perturbations in electric transmission grids," *arXiv preprint arXiv:1706.10130*, 2017.

[97] S. Tamrakar, M. Conrath, and S. Kettemann, "Propagation of disturbances in ac electricity grids," *Scientific Reports*, vol. 8, p. 6459, 2018.

[98] J. S. Thorp, C. E. Seyler, and A. G. Phadke, "Electromechanical wave propagation in large electric power systems," *IEEE Transactions on Circuits and Systems I: Fundamental Theory and Applications*, vol. 45, no. 6, pp. 614–622, 1998.

[99] M. Parashar, J. S. Thorp, and C. E. Seyler, "Continuum modeling of electromechanical dynamics in large-scale power systems," *IEEE Transactions on Circuits and Systems I: Regular Papers*, vol. 51, no. 9, pp. 1848–1858, 2004.

Bibliography

[100] X. Yan, W. Fushuan, G. Ledwich, and X. Yusheng, "Electromechanical wave in power systems: theory and applications," *Journal of Modern Power Systems and Clean Energy*, vol. 2, no. 2, pp. 163–172, 2014.

[101] A. Ulbig, T. S. Borsche, and G. Andersson, "Impact of low rotational inertia on power system stability and operation," *IFAC Proceedings Volumes*, vol. 47, no. 3, pp. 7290–7297, 2014.

[102] P. Tielens and D. Van Hertem, "The relevance of inertia in power systems," *Renewable and Sustainable Energy Reviews*, vol. 55, pp. 999–1009, 2016.

[103] M. Milligan, B. Frew, B. Kirby, M. Schuerger, K. Clark, D. Lew, P. Denholm, B. Zavadil, M. O'Malley, and B. Tsuchida, "Alternatives no more: Wind and so- lar power are mainstays of a clean, reliable, affordable grid," *IEEE Power and Energy Magazine*, no. 13, pp. 78–87, 2015.

[104] W. Winter, K. Elkington, G. Bareux, and J. Kostevc, "Pushing the limits: Europe's new grid: Innovative tools to combat transmission bottlenecks and reduced inertia," *IEEE Power and Energy Magazine*, no. 13, pp. 60–74, 2015.

[105] A. Ulbig, T. S. Borsche, and G. Andersson, "Analyzing rotational inertia, grid topology and their role for power system stability," *IFAC-PapersOnLine*, vol. 48, no. 30, pp. 541–547, 2015.

[106] H. Bevrani, T. Ise, and Y. Miura, "Virtual synchronous generators; a survey and new perspectives," *Intl. Journal of Electrical Power and Energy Systems*, no. 54, pp. 244–254, 2014.

[107] J. Yan, R. Pates, and E. Mallada, "Performance tradeoffs of dynamically controlled grid-connected inverters in low inertia power systems," in *IEEE 56th Annual Conference on Decision and Control*, IEEE, 2017.

[108] J. Quintero, V. Vittal, G. T. Heydt, and H. Zhang, "The impact of increased penetration of converter control-based generators on power system modes of oscillation," *IEEE Transactions on Power Systems*, vol. 29, no. 5, pp. 2248–2256, 2014.

[109] L. Pagnier and P. Jacquod, "Optimal placement of inertia and primary control : a matrix perturbation theory approach," *to be published*, 2019.

[110] A. Mešanović, U. Münz, and C. Heyde, "Comparison of H_∞, H_2, and pole optimization for power system oscillation damping with remote renewable generation," *IFAC-PapersOnLine*, vol. 49, no. 27, pp. 103–108, 2016.

[111] B. K. Poolla, S. Bolognani, and F. Dörfler, "Optimal placement of virtual inertia in power grids," *IEEE Transactions on Automatic Control*, vol. 62, no. 12, pp. 6209–6220, 2017.

[112] M. Pirani, J. Simpson-Porco, and B. Fidan, "System-theoretic performance metrics for low-inertia stability of power networks," in *Decision and Control (CDC), 2017 IEEE 56th Annual Conference on*, pp. 5106–5111, IEEE, 2017.

[113] T. S. Borsche, T. Liu, and D. J. Hill, "Effects of rotational inertia on power system damping and frequency transients," in *IEEE 54th Annual Conference on Decision and Control*, pp. 5940–5946, IEEE, 2015.

[114] T. S. Borsche and Dörfler, "On placement of synthetic inertia with explicit time-domain constraints," *arXiv:1705.03244*, 2017.

[115] F. Paganini and E. Mallada, "Global performance metrics for synchronization of heterogeneously rated power systems: The role of machine models and inertia," *arXiv preprint arXiv:1710.07195*, 2017.

[116] J. J. Sakurai and E. D. Commins, *Modern quantum mechanics, revised edition.* AAPT, 1994.

[117] D. McIntyre, *Quantum Mechanics.* Pearson Addison-Wesley, San Francisco, 2012.

[118] L. Guo, C. Zhao, and S. Low, "Graph laplacian spectrum and primary frequency regulation," *arXiv preprint arXiv:1803.03905*, 2018.

[119] M. Porfiri and M. Frasca, "Robustness of synchronization to additive noise: how vulnerability depends on dynamics," *to be published*, 2018.

[120] D. Klein and M. Randić, "Resistance distance," *J. Math. Chem.*, vol. 12, p. 81, 1993.

[121] K. Stephenson and M. Zelen, "Rethinking centrality: Methods and examples," *Social networks*, vol. 11, no. 1, pp. 1–37, 1989.

[122] J. MacQueen *et al.*, "Some methods for classification and analysis of multivariate observations," in *Proceedings of the fifth Berkeley symposium on mathematical statistics and probability*, pp. 281–297, Oakland, CA, USA, 1967.

[123] S. Kettemann, "Delocalization of disturbances and the stability of ac electricity grids," *Physical Review E*, vol. 94, no. 6, p. 062311, 2016.

[124] T. Coletta and P. Jacquod, "Transient primary control effort of ac electric power networks under line contingencies," *IFAC-PapersOnLine*, vol. 51, no. 23, pp. 337–342, 2018.

[125] T. Coletta, B. Bamieh, and P. Jacquod, "Transient performance of electric power networks under colored noise," *arXiv preprint arXiv:1807.09048*, 2018.

[126] E. Tegling, B. Bamieh, and D. F. Gayme, "The price of synchrony: Evaluating the resistive losses in synchronizing power networks.," *IEEE Trans. Control of Network Systems*, vol. 2, no. 3, pp. 254–266, 2015.

[127] M. Fardad, F. Lin, and M. R. Jovanovic, "Design of optimal sparse interconnection graphs for synchronization of oscillator networks," *IEEE Transactions on Automatic Control*, vol. 59, no. 9, pp. 2457–2462, 2014.

[128] T. W. Grunberg and D. F. Gayme, "Performance measures for linear oscillator networks over arbitrary graphs," *IEEE Transactions on Control of Network Systems*, vol. PP, no. 99, p. 1, 2016.

[129] M. Siami and N. Motee, "Fundamental limits and tradeoffs on disturbance propagation in linear dynamical networks," *IEEE Transactions on Automatic Control*, vol. 61, no. 12, pp. 4055–4062, 2016.

[130] M. Tyloo, T. Coletta, and P. Jacquod, "Robustness of synchrony in complex networks and generalized kirchhoff indices," *Phys. Rev. Lett.*, vol. 120, p. 084101, 2018.

[131] M. Tyloo, L. Pagnier, and P. Jacquod, "The key player problem in complex oscillator networks and electric power grids: Resistance centralities identify local vulnerabilities." submitted.

[132] D. J. Klein and M. Randić, "Resistance distance," *Journal of mathematical chemistry*, vol. 12, no. 1, pp. 81–95, 1993.

[133] L. Gambuzza, A. Buscarino, L. Fortuna, M. Porfiri, and M. Frasca, "Analysis of dynamical robustness to noise in power grids," *IEEE Journal on Emerging and Selected topics in Circuits and Systems*, no. 7, p. 413, 2017.

[134] D. Gautam, V. Vittal, and T. Harbour, "Impact of increased penetration of dfig-based wind turbine generators on transient and small signal stability of power systems," *IEEE Transactions on power systems*, vol. 24, no. 3, pp. 1426–1434, 2009.

[135] S. Eftekharnejad, V. Vittal, G. T. Heydt, B. Keel, and J. Loehr, "Small signal stability assessment of power systems with increased penetration of photovoltaic generation: A case study," *IEEE Transactions on Sustainable Energy*, vol. 4, no. 4, pp. 960–967, 2013.

[136] D. Bertsimas and J. N. Tsitsiklis, *Introduction to linear optimization.* Athena Scientific Belmont, MA, 1997.

[137] F. Dörfler and F. Bullo, "Kron reduction of graphs with applications to electrical networks." *IEEE Trans. on Circuits and Systems*, vol. 60, no. 1, pp. 150–163, 2013.

[138] M. Jentsch, T. Trost, and M. Sterner, "Optimal use of power-to-gas energy storage systems in an 85% renewable energy scenario," *Energy Procedia*, vol. 46, pp. 254–261, 2014.

Laurent Pagnier

Chemin des Aulnes 1A
1967, Bramois
Switzerland
📞 +41 79 510 46 24
✉ laurent.vincent.pagnier@gmail.com
Swiss, Limbach (BE)
03.02.1990

Research interests

Integration of new renewable energy sources, Grid resilience, Power system modelling, Complex systems, Electricity markets

Education

2014–present	**PhD in Physics**, *École Polytechnique Fédérale de Lausanne (EPFL)*.
2012–2014	**Master of Science in Physics**, *École Polytechnique Fédérale de Lausanne (EPFL)*.
2009–2012	**Bachelor of Science in Physics**, *École Polytechnique Fédérale de Lausanne (EPFL)*.

Non-professional experiences

2010–present	**Volunteer Firefighter**, *Sion*.
2011–2015	**Ciné-Club EPFL (agepoly)**, *Committee Member*. Organization of events (e.g. short film contests) up to 400 participants.

Languages

French	Native language
English	Good written and spoken skills
German	Basic knowledge

Computer skills

Matlab	Excellent knowledge
C++	Good knowledge
Julia	Good knowledge

Qualities

Dynamic, Enthusiastic, Curious, Perspicacious, Appreciating team work

Hobbies

Cinema, Travelling, Climbing

Publications

P. Jacquod, L. Pagnier, "A new, central role for hydroelectricity in the energy transition", *in Proc. Hydro 2016*, Montreux (Switzerland).

T. Coletta, R. Delabays, L. Pagnier, P. Jacquod, "Large electric load fluctuations in energy-efficient buildings and how to suppress them with demand side management", *in Proc. ISGT-Europe 2016*, Ljubljana (Slovenia).

L. Pagnier, P. Jacquod, "A predictive pan-European economic and production dispatch model for the energy transition in the electricity sector", *in Proc. PowerTech 2017*, Manchester (UK).

L. Pagnier, P. Jacquod, "How fast can one overcome the paradox of the energy transition? A physico-economic model for the European power grid", *Energy*, 2018.

L. Pagnier, P. Jacquod, "Swissgrid's strategic grid 2025 : an independent analysis", *Tech. report*, 2018.

M. Tyloo, L. Pagnier, P. Jacquod, "The key player problem in complex oscillator networks and electric power grids: resistance centralities identify local vulnerabilities", submitted.

L. Pagnier, P. Jacquod, "Disturbance propagation, inertia location and slow modes in large-scale high voltage power grids", submitted.

Reference

Prof. Philippe Jacquod
School of Engineering, HES-SO
✉ philippe.jacquod@hevs.ch

117